Delft University of Technology

Faculty of Civil Engineering and Geo-sciences

Building Engineering

Master thesis

Modelling the dispersion of airborne respiratory particles

December 21, 2021

Author: B. Halberstadt

MSc Thesis

The effect of ventilation on dispersion of airborne respiratory particles

This document is written to obtain the degree of Master of Science

in Civil Engineering

at Delft University of Technology

Author

B. (Bastiaan) Halberstadt

Student number: 5180171

Graduation committee

Prof dr. L.C.M. (Laure) Itard

Chairwoman graduation committee - Faculty of Architecture and Built Environment

Dr. ir. H.R. (Roel) Schipper

Supervisor TU Delft - Civil Engineering

Dr. ir. W.H. (Willem) van der Spoel

Supervisor ABT B.V. / TU Delft - Faculty of Architecture and Built Environment

Preface

This document contains my master thesis which is part of the completion of my master degree in building engineering with a specialization in building physics at the TU Delft.

I decided to apply for a position at ABT, which I found through their website as a suggestion from a friend. ABT is a multidisciplinary engineering firm with projects in e.g. construction and building physics. Due to the pandemic of the COVID-19 disease the company aims to participate in creating a safe and healthy indoor climate by coming up with innovative solutions. ABT offers opportunities to students who want to be part of their research to reach their goals. My interest in this current global issue and my specialization in building technology and physics had made me decide to apply for this position at ABT and be a part of this research. I would like to thank the company for the opportunity that was given to me and to be part of this research.

During this year a lot has happened influencing all of us. From social distancing till full lockdown and working from home. Initially it was hard to find a concrete direction for the research but with passing time it became more clear. I took a challenge by not only writing a thesis about a topic I hardly knew anything about, but also by doing modelling in Python, which I had never done before. With ups and downs, both during the research and personally I managed to complete my thesis. I have learned a lot about modelling, physics and about doing research in general.

And of course I could not have completed my thesis without the help of my supervisors. Firstly I would like to thank Robert-Jan Labeur for his guidance and advice regarding turbulence modelling. Unfortunately he had to step out of the committee because of the aftermath of corona, I wish him a speedy recovery.

Secondly I would like to thank Roel Schipper and Laure Itard for their input and guidance during the committee meetings and advice on how to approach my research.

Special thanks goes to Willem van der Spoel who has fulfilled the role of daily supervisor and without whom I could not have completed my thesis. I have learned a lot during our weekly meetings.

Lastly I want to thank my family and friends for their support during this year. You have given me the positiveness and distraction when I needed it.

Abstract

The outbreak of the COVID-19 virus has increased the interest in respiratory droplet dispersion in the built environment. The dispersion of these droplets is inseparable from transmission risk. Sneezing, coughing and breathing can be modelled in many ways. In this study several models of increasing complexity are proposed and compared.

Three different models are distinguished. The first is a simple ballistic model, where the trajectories of particles of different sizes are simulated, given an initial velocity and particle diameter. This simulation gives a first insight in the movement of particles from Newton's second law.

Model 2 works by releasing particles in a turbulent jet. Mean properties of turbulent jets have been derived from experiments and computer modelling. By means of particle tracking, the dispersion of three different sizes of particles are monitored. The turbulent behaviour of the jet is captured by applying a stochastic discontinuous random walk model (DRW) in Model 2. The smallest particles (10 μm) are airborne, while the large (100 μm) particles fall out of the turbulent jet and settle on the ground. Medium size particles (50 μm) have the widest range of dispersion. The effect of evaporation has been studied in this research as well. Both relative humidity and relative velocity (the velocity between the surrounding air and the particle) influence the evaporation speed. The medium size particles are affected the most by evaporation. Depending on the ambient conditions, the medium size particles either behave more like the large particles or as the small particles.

The third model contains the effect of an ambient crossflow, representing ventilation flows. Trajectories of bent jets have been calculated. Eulerian solutions for dilution have been found for such bent jets. No mean properties in literature have been found for bent jets and hence the Langrangian particle tracking model could not be used.

Based on the results of model 2 we conclude that ventilation flows will have a tremendous impact on the dispersion of respiratory droplets, in particular the particles with initial diameter 75 - 100 μm. These droplets become airborne and will follow the ventilation flow. In dryer air droplets evaporate faster and will become airborne more quickly.

Future research could be done to create a CFD model to generate analytical formulas for jets in ambient crossflows. More detailed room conditions like the stratification of air temperature can be taken into account.

Table of Contents

List of figures

List of tables

Nomenclature

List of symbols

Symbol	Meaning
A	Dummy variable to simplify equations
A_0	Area of the jet supply opening
Ar_0	Archimedes number
B	Buoyancy flux
b	Gaussian half width
b_t	Top-hat width
C_c	Slip correction factor
C_D	Drag coefficient
C_i	Empirical constants
C_L	Empirical constant to determine eddy lifetime
C_p	Specific heat at constant pressure
C_{ps}	Specific heat of solute at constant pressure
C_μ	Empirical constant to determine the eddy length scale
d_0	Jet opening diameter
d_p	Droplet diameter
D_T	Thermal diffusivity of air
D_v	Diffusivity of water vapor in air
e_{sat}	Saturation vapor pressure
e_v	Partial vapor pressure
F_b	Buoyancy force
F_d	Drag force
F_g	Gravity force
g	Gravitational acceleration
H	Dummy variable to simplify equations
I	Dummy variable to simplify equations
k	Turbulent kinetic energy
k_1	evaporation constant
k_a	Thermal conductivity of continuous phase (air)
l_e	Eddy length scale
L_v	The latent heat of vaporization of water
M	Momentum flux
M_w	Molecular weight
Nu	Nusselt number
Pr	Prandtl number
Q	Volume flux
Q_{surf}	Surface water vapor density
Q_∞	Ambient water vapor density
r	Radial distance
R	Radius of a droplet
R_0	Initial droplet radius
R_e	Reynolds number
R_g	The universal gas constant
RH	Relative humidity
s	Distance along the centreline of the jet curve
S	Stopping distance
Sc	Schmidt number
Sh	Sherwood number
T	Instantaneous droplet (surface) temperature
t	Time
T_0	Initial temperature of the jet
T_a	Ambient (local) air temperature
t_e	Eddy lifetime

t_{int}	Interaction time
t_L	Langrangian time scale
t_r	Transit time
u'	Fluctuating component of air velocity
u	Instantaneous air velocity
$\bar{u}$	Mean air velocity
u_0	Initial jet velocity
U_a	Ambient airflow
u_c	Mean centreline velocity
u_g	Air velocity
u_p	Particle velocity
u_r	Mean streamwise velocity
v	Relative velocity of a droplet
v_r	Mean transverse velocity
x	Streamwise direction
y	Transverse direction
z	Vertical direction
z_0	Initial height centre point jet
Z_B	Characteristic length scale buoyant flux source in ambient crossflow
Z_M	Characteristic length scale momentum flux source in ambient crossflow
Greek symbol	Meaning
α	Jet entrainment coefficient
β_e	Volumetric expansion coefficient
β_g	Empirical value to determine the Gaussian half width
$\Delta\rho_0$	Density difference between receiving and exhausted fluid
ε	Dissipation rate
ε_y	Mass fraction of a constituent y with respect to the total dry mass
ζ	Random number sampled from a Gaussian probability density function
λ	Mean free path of gas
ν	Viscosity of air
ν_y	The number of ions into which a solute molecule dissociates
ρ_f	Air density
ρ_g	Air density
ρ_p	Particle density
σ	The surface tension
$\sigma(r)$	Semi -empirical root mean square turbulent velocity fluctuation
τ'	Particle relaxation time
τ_t	Temperature relaxation time
ϕ_y	The practical osmotic coefficient
ω_{surf}	Mass fraction of vapor at droplet surface
ω_∞	Mass fraction of vapor in the free stream

1. Introduction

The outbreak of the COVID-19 disease in 2020 has and is having a large impact on human society globally. Many countries have been into a hard lockdown for several months. The reason for such radical measures was to drastically decrease the number of COVID-19 infected people. The primary reason is to prevent mass decease, mainly among the risk group, existing of chronically-ill and older people. The second reason is that hospitals, and in particular the intensive-care beds, had been occupied to a great extent by COVID-19 patients. In early 2021 hospitals had to postpone their other healthcare procedures due to a lack of capacity. At all costs the government's aim is to prevent a black scenario. A black scenario occurs when all intensive-care beds are occupied and medical personnel would have to start using triage.

During the lockdowns restaurants, theatres, sports centres, cinemas, stadiums and other buildings where normally large events are held, were closed. In The Netherlands, and in many other countries, governments have introduced social distancing measures. In The Netherlands this implies that everyone should always keep a minimum of 1.5 meter distance from one another. Next to that wearing facial masks is mandatory in public buildings, for example in supermarkets. Both outdoors and in indoor climates where people still gather this policy is carried out to reduce transmission of this particular virus.

Three various transmission routes of respiratory infections are distinguished (Tellier et al., 2019):

1. Close contact. The infected person exhales by e.g. speaking, sneezing or coughing and virus-laden particles fall directly onto the mouth, nose or eyes of the susceptible.
2. Airborne. Respiratory particles remain suspended in the air and by inhalation the susceptible is exposed to infectious particles.
3. Fomite. The infected touches an object or exhaled particles settle on a surface. The susceptible touches the same object or surface which results in self-inoculation.

Figure 1 shows an illustration of the three transmission routes.

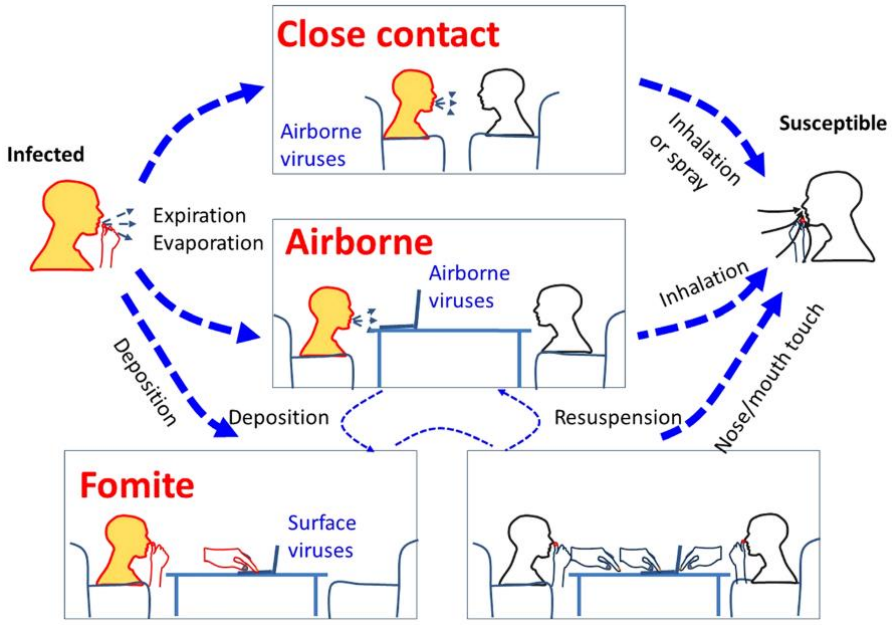

Figure 1: Possible transmission routes between an infected and a susceptible (Tellier et al., 2019)

Acute respiratory tract infections are the most common illnesses for humans worldwide (Monto, 2012). Therefore it is relevant to investigate and, if needed, improve the ventilation in public buildings to reduce transmission of viruses causing these illnesses. In the past other viruses impacting respiratory ways, like SARS in 2002, have already caused pandemics. Even though vaccinations for COVID-19 are being carried out, a new, similar, yet different virus might strike

humanity in the future. Therefore it is of great importance to understand how transmission takes place and reduce, or even avoid it at places where large groups of humans gather.

In indoor environments fresh air is supplied by ventilation systems. In large (public) indoor spaces where groups of people gather there are multiple supplies and exhausts of air. Because of this a flow pattern will arise. Larger and thus heavier respiratory particles are less influenced by these flows, however particles which are smaller in size and mass might be more likely to be influenced by such flows. Hence ventilation flows could have a significant impact on the trajectory and travel distance of respiratory particles.

1.1 Problem description

The main problem is that there are millions of buildings around the globe and that they have a number of fixed characteristics. Here one could think of function, ventilation system and typical (traditional) lay-out. Here lies a task of assessing the risk of being exposed to viruses from infected people, who might stand or sit in close proximity of you. On the other hand this task offers an opportunity to redesign, shape and rearrange our buildings to prevent future lockdowns due to similar virus outbreaks.

Exposure, as defined by Chen et al. (2020), is the total volume of respiratory droplets to which a receiver is exposed. They describe two mechanisms of transmission: through large droplets, known as direct contact and by aerosols which float in the air (W. Chen et al., 2020).

Traditionally aerosols have been defined as particles floating, or suspended in the air. The Dutch Institute for Health and Environment (RIVM) consider aerosols to be droplets in the range of 5-10 µm diameter. Smaller particles are defined as droplet nuclei. The World Health Organization states that particles of 5-10 µm are respiratory droplets and smaller ones droplet nuclei (Team, 2020).

What is neither clear nor fully understood is the effect of ventilation air flows on transmission in indoor spaces, and in particular smaller droplets and aerosols. Past experiments with aerosols used constant settings for air velocity (0 m/s), relative humidity and air temperature (Team, 2020). In different conditions, for example in higher relative humidity environments, the lifetime, evaporation time and travel distance of the aerosols increases (Chong et al., 2021).

Well ventilated indoor environments could play a crucial role in reducing or even fully prevent the airborne spread of viruses. Smart placement of supplies and exhausts potentially have a large impact on the travel distance of aerosols and therefore on the safe distance from one person to another. Other factors are the amount of ventilation air and the quality. Hence the type of ventilation and the presence of for example filters are of high significance likewise.

Brohus & Nielsen (1996) showed that personal exposure and concentration levels differ around a body when comparing sitting and standing in a displacement ventilated room (Brohus & Nielsen, 1996). This means that not only the type of ventilation should be considered when assessing an indoor space, but also its function.

Xie et al. (2007) created a model to determine how far droplets travel taking into account the droplet size, velocity and evaporation (Xie et al., 2007). They modelled the particles as spheres existing out of pure water. This, however, is an approximation. Wei & Li took this model as a starting point and added turbulence to their model jet of air for more realistic results (Wei & Li, 2015).

Chen et al. (2020) took this turbulent jet model and used it to determine the exposure of short range respiratory infection. The model includes human facial features, namely the eyes, nose and mouth as these are the place where the transmission takes place (W. Chen et al., 2020).

1.2 Objective and research questions

The main goal of this research is to understand, determine, and predict the effect of ventilation-controlled indoor airflow patterns on the dispersion of exhaled particles. Existing ventilation systems could and should be assessed and during design of new buildings the results may be used for a safe design of indoor spaces.

The main research question is:

What is the influence of ventilation air flows on the dispersion of airborne respiratory particles?

To be able to answer the research question several sub questions have been formulated. Answers to these questions lead to, and elaborate the answer.

Sub questions are:

1. What is the range of particle sizes relevant for the direct and airborne transmission?
2. What is the distribution of respiratory particles for different human breathing modes?
3. What is the influence of evaporation on the travel distance and lifetime of exhaled particles?
4. How does a turbulent jet interact with a crossflow?
5. What is the influence of ventilation air flows on the travel distance and lifetime of exhaled particles?

1.3 Methodology

The approach is to combine a desk research followed by modelling. Afterwards the model will be optimized and extended with the ultimate goal of assessing a case study.

Shortly this method consist of the following phases:

- Research phase
- Model phase
- Optimization and evaluation phase
- Finalising phase

Initially research will be conducted by researching the existing literature: The distribution of respiratory particle sizes, jets and plume models, movement of particles through air, turbulence, evaporation of sputum droplets and exposure to respiratory droplets in indoor environments.

The next step is to create the turbulent jet model to estimate the trajectories of respiratory particles. The model should take into account both the physical characteristics of a human and well as the room conditions. The model will be created (programmed) using Python. The initial goal is to reproduce a model from the literature and produce the same results to validate the created model. The next step is to expand the model so it can be used to assess a case study. The model should not be computationally heavy.

Then a third model will be created to determine the effect of an ambient crossflow on the turbulent jet.

Lastly the outcome of the research will be discussed and evaluated in the finalising phase. The question on whether ventilation air flows have influence on the dispersion of respiratory particles will be answered.

2. Literature review

2.1 introduction

The following topics will be addressed in the literature review:

- Breathing and respiratory particle size distribution
- Jets and plumes
- Movement of particles through air
- Interaction of a turbulent flow with a crossflow
- Evaporation of droplets in air
- Exposure to respiratory droplets in indoor environments

2.2 Breathing and respiratory particle size distribution

Firstly we start by analysing breathing of human beings and look at the particle size distribution. This is done for different means of breathing: regular breathing, talking, coughing and sneezing.

2.2.1 Breathing

Humans breath in a rhythmic way. Each individual has its own breathing pattern, which is reasonably stable. A way to model human breathing is to take an average of the different characteristics from different humans (Xu, 2018).

The flow rate of a breathing person follows roughly a sinusoidal shape, as is clearly visible in Figure 2.

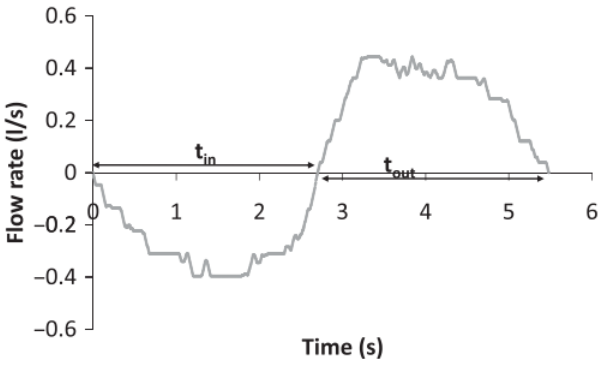

Figure 2: flow rate for normal breathing of a person (Gupta et al., 2010)

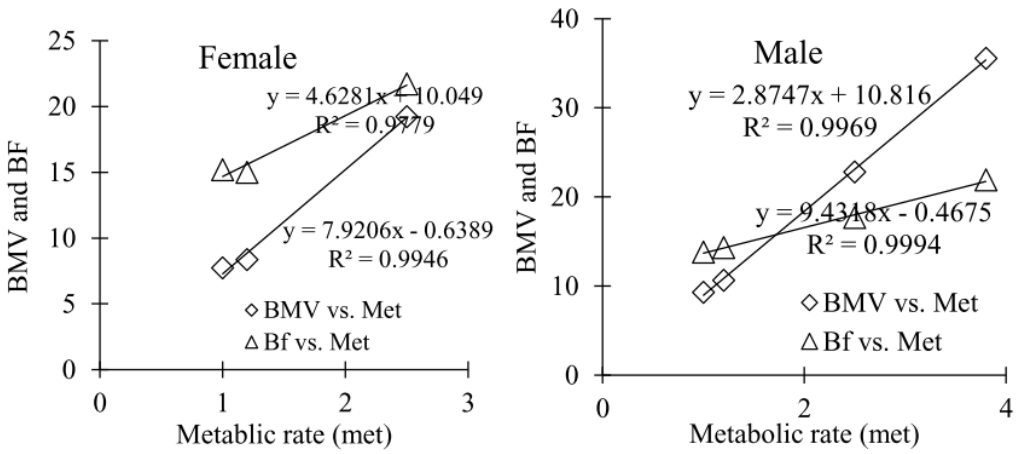

Figure 3: linear fitting of breathing minute volume in litres and breathing frequency minute^{-1} with metabolic rate (Gupta et al., 2010)

The breathing rate and volume depend greatly on activity, gender and age. In general male subjects breath more frequently and larger volumes than their female counterparts. Two factors can be distinguished, which have influence on the breathing airflow. These are human factors like the metabolic rate and room condition factors like ventilation and room temperature (Xu, 2018).

Next to frequency and volume there are also external characteristics of the human body which have an influence on the jet of air being produced while breathing. In Table 1, Table 2 and Figure 4, the most important results from external characteristics (Gupta et al., 2010) are presented.

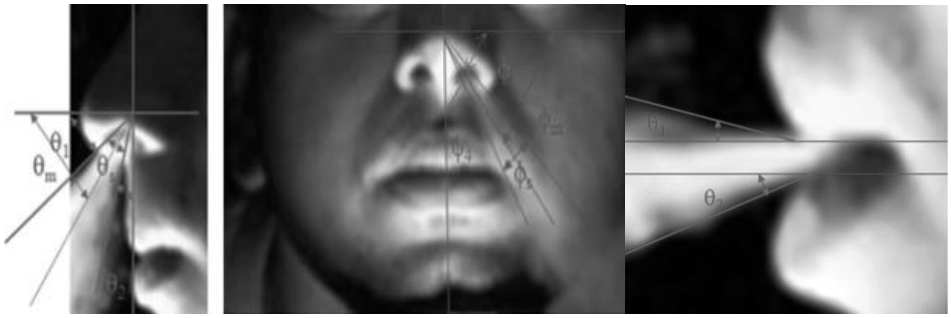

Figure 4: Angles to define nose and mouth breathing jets (Gupta et al., 2010)

Table 1: Average angle values to define nose and mouth breathing.

Angle	Mean angle and 95% confidence bound
θ_m	60° ± 6°
φ_m	69° ± 8°
θ_s	23° ± 14°
φ_s	21° ± 10°
θ_{sp} (mouth side spread)	30°

Table 2: Average nose and mouth opening for male and female.

	Mean area nose opening and 95% confidence bound	Mean area mouth opening and 95% confidence bound
Male	0.71 ± 0.23 cm^2	0.56 ± 0.10 cm^2
Female	1.20 ± 0.52 cm^2	1.16 ± 0.67 cm^2

2.2.2 Particle size distribution

In the past multiple researches about the particle distribution have already been carried out. In this paragraph a collection and comparison will be made. Finally an appropriate distribution will be determined for the continuation of this research.

Chao et al. (2009) compared their own findings to previous researches.

Table 3: Average droplet number count per person measured at the 10 and 60 mm distances (Chao et al., 2009).

Size range (µm)	Size class (µm)	Speaking (averaged number per person, counting 1-100 for 10 times)				Coughing (averaged number per person, coughing 50 times)			
		10 mm	S.D.	60 mm	S.D	10 mm	S.D.	60 mm	S.D
2-4	3	1.7	1.62	4.6	3.41	4.0	3.46	3.5	2.28
4-8	6	26.8	8.94	16.1	3.28	55.5	15.88	17.6	7.47
8-16	12	9.2	4.67	6.9	3.35	20.4	15.44	6.5	5.15
16-24	20	4.8	4.07	4.3	2.95	6.7	4.6	2.8	2.98
24-32	28	3.2	2.36	2.6	2.07	2.5	2.42	1.4	1.71
32-40	36	1.6	1.03	1.9	0.74	2.4	2.37	0.6	0.97
40-50	45	1.7	0.90	1.0	0.47	2.0	2.67	0.2	0.48
50-75	62.5	1.8	0.98	1.4	0.97	2.0	1.41	0.9	2.16
75-100	87.5	1.3	0.65	1.2	0.79	1.4	1.84	0.5	0.85
100-125	112.5	1.7	1.01	1.2	0.92	1.7	1.77	1.0	1.56
125-150	137.5	1.6	1.03	0.4	0.70	1.6	1.84	0.7	1.25
150-200	175	1.7	1.01	1.0	0.94	4.4	2.8	0.6	0.67
200-250	225	1.5	0.82	0.4	0.52	2.5	1.84	0.5	1.07
250-500	375	1.4	0.50	0.6	0.70	2.1	1.2	0.9	0.82
500-1000	750	0.5	0.82	0.1	0.32	1.4	0.97	0.4	0.71
1000-2000	1500	0.0	0.00	0.0	0.00	0.0	0.00	0.0	0.00

The measured size distributions are depicted in Figure 5, while also being compared to several other studies.

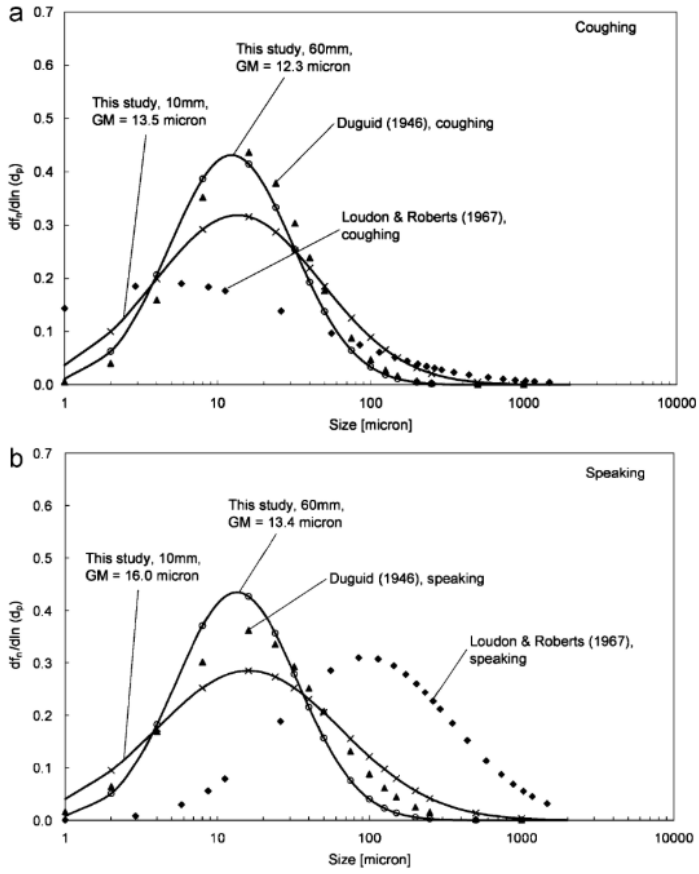

Figure 5: (a) Droplet size distribution for coughing and (b) speaking (Chao et al., 2009)

The maximum velocity through coughing of a male speaker was 13.2 m/s and 10.2 m/s for a female speaker. During speaking the average velocities were 4.6 m/s for male and 3.6 m/s for female.

Comparing the 10 and 60 mm distance distribution, the same phenomenon stands out for both coughing and speaking. The initial distribution has a wider and lower shape compared to that at a further distance. This can be explained by the fact that evaporation has taken place, reducing the size of the largest particles.

W. Chen et al. (2020) followed the distribution of Duguid and provided a discrete distribution of exhaled particles for speaking and coughing (Figure 6). Speaking was simulated by letting participants of the experiment talk from 1 to 100 once.

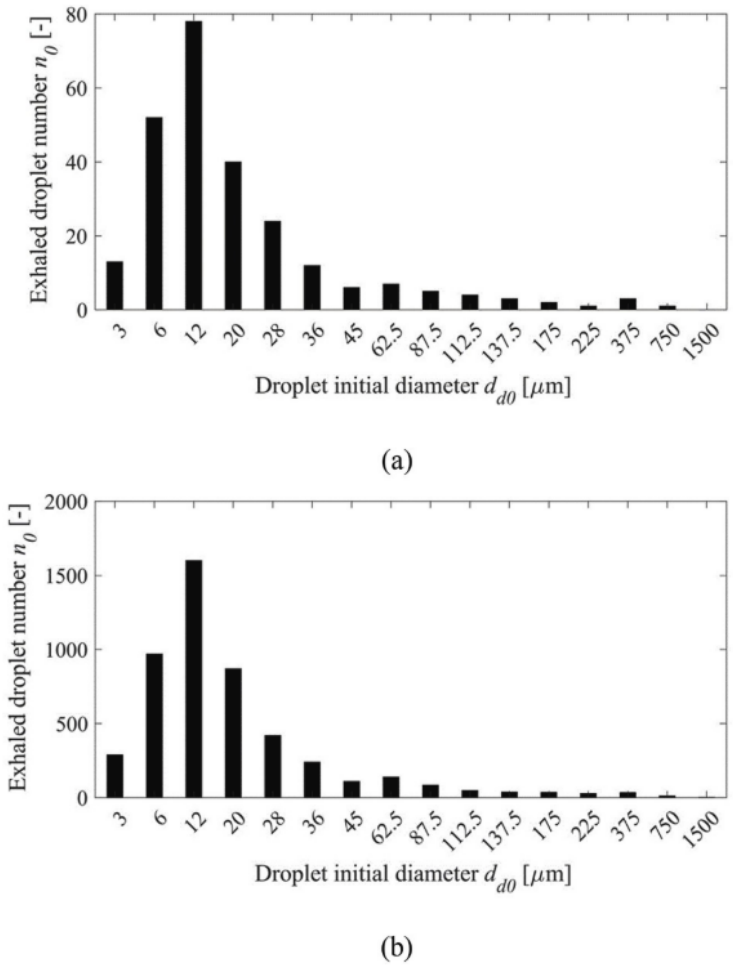

Figure 6: Number distribution of exhaled droplets at the mouth opening for (a) speaking and (b) coughing once (W. Chen et al., 2020).

A similar research has been conducted by Hartmann et al. (2020), however their research focused mainly on the production of bioaerosols. In Figure 7 the ratio of the source strength per particle size is shown for different methods of breathing. Here the particle source strength is the amount of particles per second subjects exhale for different activities. The distribution of these aerosols are significantly different: the particles are in general (>80%) smaller than 1 µm and 99.9% is smaller than 5 µm.

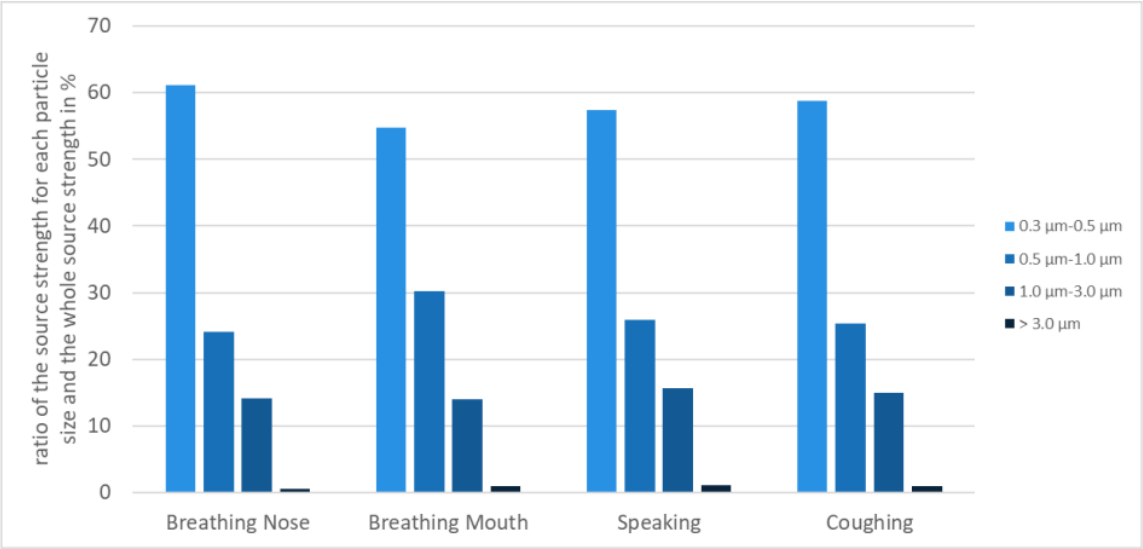

Figure 7: Ratio of source strength for different particle sizes (Hartmann et al., 2020)

The results obtained by Papineni & Rosenthal (1997) show a similar result as Hartmann et al. (2020). In every mode of breathing the number of particles smaller than 1µm are the largest.

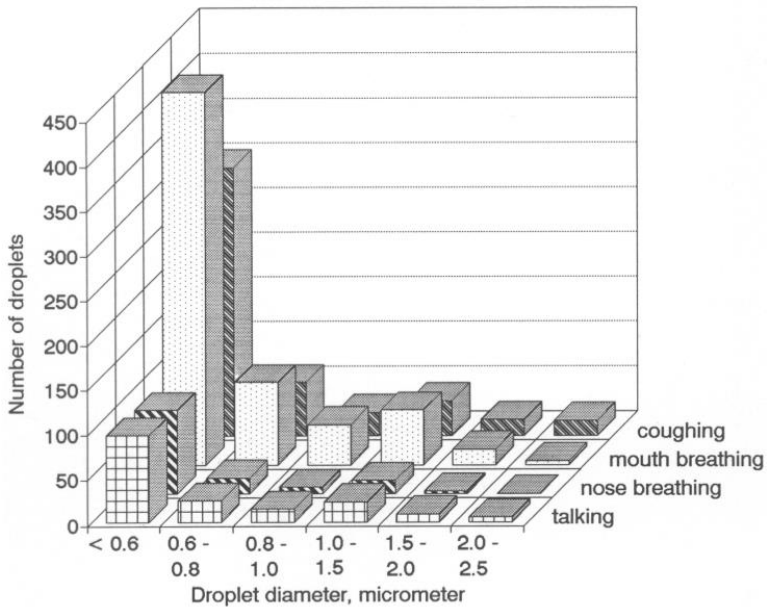

Figure 8: Mean droplet concentration in exhaled breath (Papineni & Rosenthal, 1997)

In a review paper comparing twenty six previous researches it is stated that healthy individuals produces particles with a diameter between 0.01 and 500 µm. Their infected counterparts produce particles between 0.05 and 500 µm in diameter (Gralton et al., 2011).

Coughs produce on average between 900 and 302,200 particles. The peak velocity is located in a range between 8 and 22 m/s while its duration falls within a range between 0.25 to 0.8 seconds (S. Liu & Novoselac, 2014).

Measurements have been done to determine the air volume and flow rate by human coughing (Lindsley et al., 2013). An ultrasonic spirometer has been used to do so. The coughs have a mean volume of 4.15 l and the peak flow rate is 10.5 l/s.

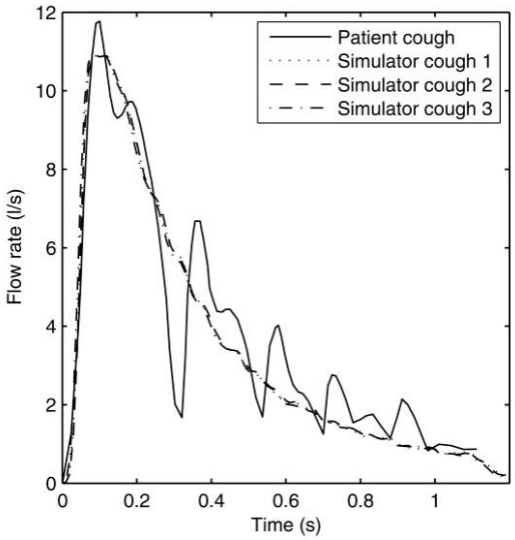

Figure 9: Cough flow rate for an influenza patient

2.2.3 Pulse and steady source jets

Even though human breathing happens in a pattern with a sinusoidal shape, the flow can be described where the peak velocity is a linear function of the (horizontal) distance from the (mouth) opening. This shows huge similarity with the expression of the centreline velocity in a jet. From the measured exhalation trajectories during an experiment, the conclusion was that these trajectories match the non-isothermal jet described theoretically by Xie et al. (2007) Olmedo et al. (2012).

However specific research has been done determining the flow characteristics of pulse jets. Yadav et al. (2016) concluded that in pulse jets, vortices form earlier than in a steady jet. This causes the mixing region to become wider, increase the radial spreading. This decreases the length of the potential core and increases the rate of mixing.

They compared the time-averaged velocity profile of a circular steady jet and a pulse jet. In Figure 10 several jets are compared, with Reynolds number equal to 7550, Strouhal number of 0.63 and amplitude of pulsation 8.5%. In this comparison there are only small differences however it should be noted the Reynolds number is fairly large compared to the expected Reynolds numbers or respiratory particles with limited velocity.

Another important conclusion was that closer to the nozzle, where the distance from nozzle to surface is small, pulsating jets have similar velocity profiles but larger turbulence intensities. In the next subchapter more is discussed about velocity profiles and turbulence of jets.

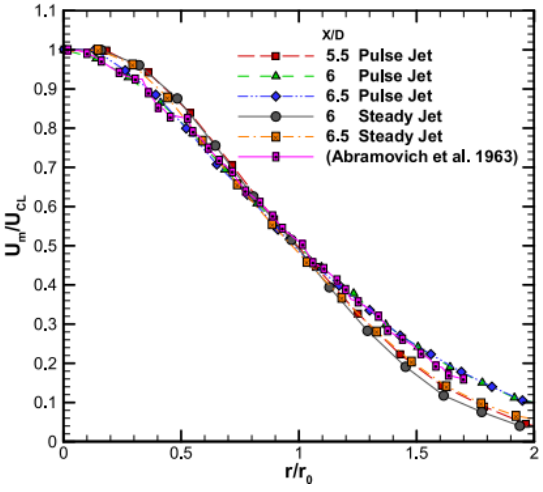

Figure 10: Velocity distribution of circular turbulent jets (Re=7550, St=0.63, A=8.5%) (Yadav et al., 2016).

2.3 Jets and plumes

This section is about jets and plumes. First the general characteristics of a jet and plume will be described. Next turbulence is covered and lastly different particle tracking models are discussed.

2.3.1 Basic characteristics of a jet

Terms as plumes, forced plumes, buoyant jets and jets all belong to the family of free turbulent flows. We speak of a pure plume when a flow is solely being created by buoyancy. On the other hand the term jet is used when a flow is supplied by only momentum (Crapper, 1977). However in many cases a flow will arise from both buoyancy and momentum and the terms forced plumes and buoyant jets are used for those.

For all these free turbulent flows holds that on average the spread follows a Gaussian distribution for both velocity and density. This is shown and described by many researchers (e.g. Chan et al., 2014; Fukushima et al., 2002). Figure 11 shows a typical Gaussian distribution of the mean axial velocity profile of a turbulent jet. Figure 12 shows the radial mean velocity profile which is perpendicular to the axial velocity.

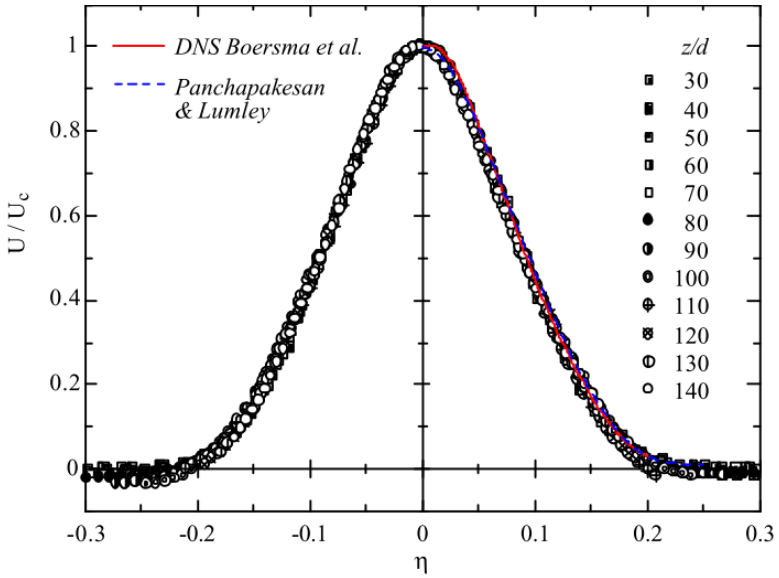

Figure 11: Axial mean velocity profile along the jet (Fukushima et al., 2002).

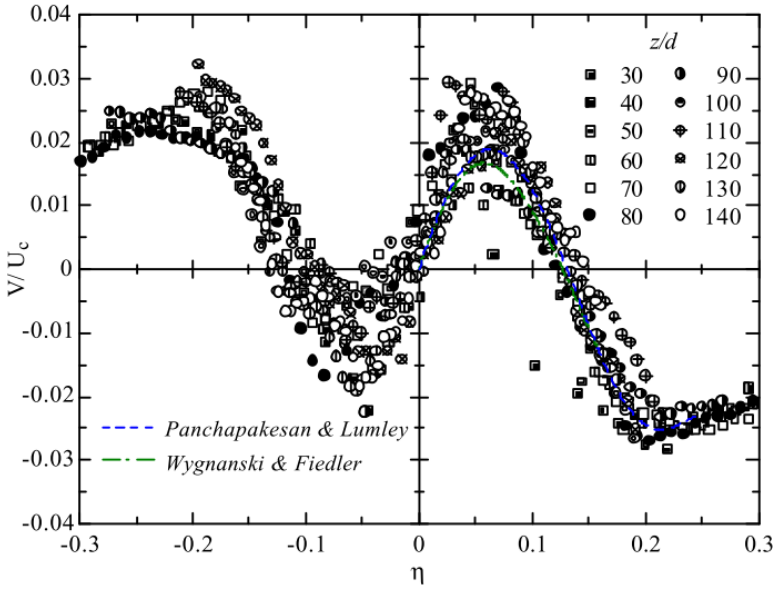

Figure 12: Radial mean velocity profile along the jet (Fukushima et al., 2002).

Close to the orifice of a jet a laminar shear layer arises. This layer is highly unstable and creates ring vortices at the edge of the jet (List, 1982). A similar conclusion is drawn by (Nielsen et al., 2009), stating that "The flow is partly a vortex ring and partly an instantaneous turbulent jet" (Nielsen et al., 2009, p7).

An isothermal jet does not take into account the effect of buoyancy. In the non-isothermal jet the change in diffusion characteristics are taken into account. In case of an exhalation jet the air temperature is typically higher (35 °C) than of the ambient air (20-25 °C). This creates an upward curve in the jet as shown in Figure 13b.

A typical jet has several key characteristics. Firstly an opening with a certain diameter d_0 in case of a circular opening. At this location the flow has an initial velocity u_0. Along the centreline the streamwise velocity is the largest and follows a Gaussian distribution along the radius. In the initial region, flow establishment zone or transitional zone, the distribution of velocity components is equal except that within the potential core the velocity is equal to the initial velocity. The length of the initial region is equal to $6.8d_0$ according to Xie et al. (2007) while Wei & Li (2015), use a length of $6.2d_0$. Fischer et al. (1979) wrote that the time-averaged velocity distribution is Gaussian in a jet at more than six jet diameters from the orifice.

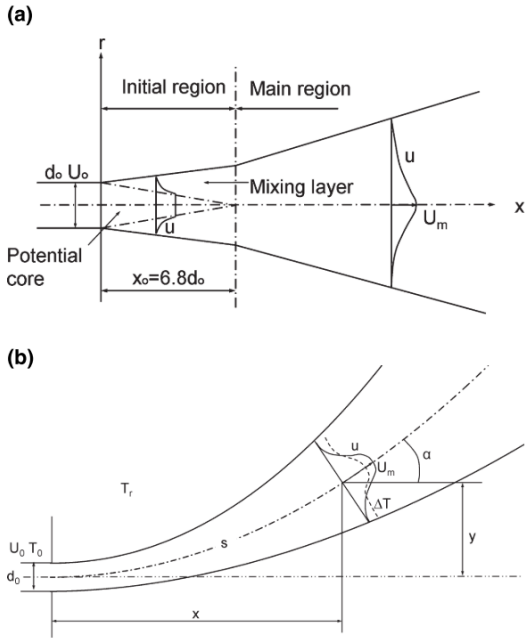

Figure 13: (a) an isothermal jet and (b) a non-isothermal jet (Xie et al., 2007)

Wei & Li (2015) describe the turbulent jet in formulas. The curved centreline of a non-isothermal circular jet is defined by:

$$z = \frac{0.0354 Ar_0 x^3}{\sqrt{A_0}} \sqrt{\frac{T_0}{T_a}} \tag{1}$$

With T_0 the initial temperature of the exhaled jet, T_a the temperature of the ambient air (the room air temperature) and Ar_0 the Archimedes number.

The Archimedes number for gasses is defined by (Xie et al., 2007):

$$Ar_0 = \frac{g\sqrt{A_0}\beta_e \Delta T_0}{u_0^2} \tag{2}$$

Where A_0 is the area of the supply (mouth) opening, β_e the volumetric expansion coefficient, $\Delta T_0 = T_0 - T_a$ where T_0 is the temperature of the exhaled air, T_a the ambient temperature and u_0 the initial velocity of the exhaled air.

The mean centreline velocity u_c is defined by:

$$u_c = 6.2u_0 \frac{d_0}{s} \tag{3}$$

With u_0 the velocity of the supply, d_0 the supply diameter and s the distance along the centreline of the jet curve. The mean streamwise velocity u_r and mean transverse velocity v_r are defined as follows:

$$u_r = u_c \exp\left(-\frac{r^2}{b^2}\right) \tag{4}$$

$$v_r = \alpha u_c \frac{1-\exp\left(-\frac{r^2}{b^2}\right)-\left(\frac{\beta_g}{\alpha}\right)\left(\frac{r^2}{b^2}\right)\exp\left(-\frac{r^2}{b^2}\right)}{\frac{r}{b}} \tag{5}$$

Where $b = \beta_g x$ is the Gaussian half width with $\beta_g = 0.114$; $\alpha = 0.057$ is the jet entrainment coefficient. The top-hat width is given by $b_t = \sqrt{2} * b$. This represents the visual boundary of the jet.

The temperature profile is similar to the velocity profile. The profile is, however somewhat flatter due to the difference between momentum and energy diffusion. The corresponding formulas are:

$$\frac{T_m - T_a}{T_0 - T_a} = \frac{\rho_{vm} - \rho_{va}}{\rho_{v0} - \rho_{va}} = \frac{5.0}{s}\sqrt{\frac{T_0}{T_a}} \tag{6}$$

$$\frac{T - T_a}{T_m - T_a} = \frac{\rho_v - \rho_{va}}{\rho_{vm} - \rho_{va}} = \exp\left[\frac{r^2 \ln 2}{(0.11)^2}\right] \tag{7}$$

At the orifice there are three other key characteristics: the initial volume flux Q, the specific momentum flux M and the buoyancy flux B. In the case of a round jet the corresponding formulas are (Fischer et al., 1979):

$$Q = \frac{1}{4}\pi d_0^2 u_0 \tag{8}$$

$$M = \frac{1}{4}\pi d_0^2 u_0^2 = Q u_0 \tag{9}$$

$$B = g(\Delta\rho_0 / \rho)Q \tag{10}$$

Where $\Delta\rho_0$ is the difference in the density between the receiving fluid and exhausted fluid and g the gravitational acceleration. The book of Fischer et al. (1979) is however about mixing of inland and coastal waters, meaning both receiving and exhausted fluids are water.

2.3.2 Turbulence in free shear flows

"Turbulence is that state of fluid motion which is characterized by apparently random and chaotic three-dimensional vorticity"(George, 2013, p. 11). Turbulence occurs in three-dimensional flows and results in increased heat transfer, drag, energy dissipation and mixing.

Free shear flows are defined as inhomogeneous flows with a certain mean velocity gradient when there are no boundaries present. This means the flow can develop freely, for example air exhausted from one's mouth or nostrils during breathing (George, 2013). The characteristic which distinguishes a free turbulent flow from a homogeneous flow is its turbulent/non turbulent interface, which constrains the jet's fluid.

Essential is the (non-)existence of an external flow on the turbulent jet, as the momentum entering the jet makes a difference in how the flow develops, in particular further downstream (George, 2013). A ventilation cross flow can be indicated as such external flow, influencing how the exhalation jet develops.

A common way to solve turbulence models is by using eddy-viscosity models like the standard k-ε model. These models are highly computational intensive. Zero-equation turbulence models require less computer capacity than the previously mentioned model. The reason for this is that no additional differential equations have to be solved, saving a lot of computational power (Q. Chen & Xu, 1998).

2.3.3 Particle tracking models

There are multiple simulation methods to calculate the mean particle diffusion. Firstly we distinguish the Eulerian and the Langrangian approach. The Eulerian approach is to use and solve the transport equations regarding the concentration of particles. Here a very important variable is the molecular diffusion coefficient (Saidi et al., 2014). Diffusion is the result of Brownian motion caused by molecules of the fluid colliding with the particles creating an uncontrolled movement (Floyd et al., 2017).

The Langrangian approach calculates the trajectory of individual particles which is also known as particle tracking. The trajectories are calculated by taking into account external forces acting on the particle, which are the drag force, gravitational force, pressure gradient force, virtual mass, Basset force, Brownian force and Saffman's life force (Saidi et al., 2014). When the ratio between air density and particle density is large, such as for water droplets in air at atmospheric pressure, all but the drag, gravitational and Brownian forces can be neglected.

Brownian forces can additionally be neglected when the molecular diffusion is much smaller than turbulent diffusion, or when other processes that induce a spread of particles are dominant. For example, the molecular diffusion length of a 1 μm water droplet in air during 200 seconds is less than 0.1 mm. As in this work we are interested in droplets > 1 μm and dispersion lengths typically > 10 mm, Brownian forces can be neglected.

There are resolved-eddy simulations, for example direct numerical simulations (DNS) and large eddy simulations (LES). On the other hand there are unresolved-eddy simulations like the Reynolds-averaged Navier-Stokes (RANS) solution (Bocksell & Loth, 2001).

Langrangian models use the solutions of the RANS simulations, which are the mean flow properties like mean velocity and temperature. These are then used to calculated large amounts of particle trajectories (Bocksell & Loth, 2001). These Langrangian stochastic models, models which contain random variables, can be divided into three categories. They are presented from least computational intensive to most intensive: Discontinuous random walk model (DRW), continuous random walk model (CRW) and stochastic differential equation methods (SDE) (Bocksell & Loth, 2001).

Discontinuous Random Walk model

A discontinuous or discrete random walk (DRW) is a modelling technique used to model particle tracking in turbulent flows. The principle of the DRW model lies in the interaction of the particles with eddies. This interaction last for an interaction time t_{int}. While the interaction between particle

and eddy lasts, the Root Mean Square (RMS) velocity is multiplied by a random number ζ from a Gaussian probability density function to obtain the velocity component.

$$u_i' = \zeta \sqrt{\overline{u}_i'^2} \tag{11}$$

When the interaction time has passed, a new random number is being generated and the mean velocity and its fluctuation depends on the new location of the particle in the jet. The subscript i takes on the values x, y and z, corresponding to the three different axes, respectively. The Root Mean Square (RMS) velocity fluctuation is given as a function of the turbulent kinetic energy:

$$\sqrt{\overline{u}_i'^2} = \sqrt{\frac{2k}{3}} \tag{12}$$

The air velocity in the jet is defined as the addition of the fluctuation and the mean velocity:

$$u = \overline{u} + u' \tag{13}$$

The interaction time t_{int} is the minimum of the eddy lifetime t_e and the transit time t_r, which is the time for a particle to pass through the eddy. For small particles the interaction time will be equal to the eddy lifetime since the particle will follow the fluid motion. For a larger and heavier particle might go through the eddy since this particle won't follow the motion of the fluid exactly. This is the reason why the interaction time is defined as follows (Bocksell & Loth, 2001):

$$t_{\text{int}} = \min(t_e, t_r) \tag{14}$$

$$t_e = 2t_L = 2C_L \frac{k}{\varepsilon} \tag{15}$$

$$t_r = -\tau' \ln\left(1.0 - \frac{l_e}{\tau' \left|u_g - u_p\right|}\right) \tag{16}$$

Where t_L is the Lagrangian integral time scale. $C_L \approx 0.15$ based on the kinematic energy k and dissipation ε (k-ε) turbulence model by Chao & Wan (2006).

$$\tau' = \frac{4\rho_p d_p}{3\rho_g C_D \left|u_g - u_p\right|} \tag{17}$$

$$l_e = \frac{C_\mu^{3/4} k^{3/2}}{\varepsilon} \tag{18}$$

With τ' being the particle relaxation time based on the relative velocity between the particle and the surrounding air. C_μ is an empirically determined constant with a value between 0.07 and 0.09 (Katopodes, 2019). The turbulence length scale is the size of the eddy created by large turbulent energy. l_e is the Eulerian integral length scale as defined by Wei & Li (2015), however Chao & Wan (2006) defined it as follows:

$$l_e = \frac{t_L \sqrt{\overline{u}_i'^2}}{0.36} \tag{19}$$

Plugging in equation (15) into this equation we obtain:

$$l_e = \frac{C_L k \sqrt{\overline{u}_i'^2}}{0.36\varepsilon} \tag{20}$$

The root mean square turbulent velocity fluctuation as well as the dissipation rate profile are derived from a CFD model and are expressed as follows (Wei & Li, 2015):

$$\sigma(r) = u_c C_1 \left[\exp\left(-C_2 \left(\frac{r}{b} - C_3 \right)^2 \right) + \exp\left(-C_2 \left(\frac{r}{b} + C_3 \right)^2 \right) \right] \quad (21)$$

$$\varepsilon(r) = \frac{u_c C_4 \left[\exp\left(-C_5 \left(\frac{r}{b} - C_6 \right)^2 \right) + \exp\left(-C_5 \left(\frac{r}{b} + C_6 \right)^2 \right) \right]^3}{b} \quad (22)$$

The values of the empirical constants C_1 – C_6 are given in Table 4 (Chan et al., 2014).

Table 4: Empirical constants for turbulence model.

Empirical constant	C_1	C_2	C_3	C_4	C_5	C_6
Value	0.2006	1.4147	0.6647	0.2458	1.2498	0.6594

A k-ε turbulence closure model of a pure jet was used to obtain the empirical coefficients C_1 – C_6. The CFD predicted the velocity fluctuation and dissipation rates. The turbulent kinetic energy was calculated using fully developed pipe flow equations with the inflow velocity, the Reynolds number and turbulence intensity as parameters. The dissipation rate ε can then be calculated from the kinetic energy and the length scale. A detailed description is found in Chan et al. (2014).

The turbulence intensity is defined as the ratio between the standard deviation of the fluctuation and the mean air velocity of the space considered. Turbulence intensity in the breathing zone lays between 30-40% (Xu, 2018).

Continuous Random Walk model

The CRW model differs from the DRW model in a way that while the DRW model keeps the fluctuating component fixed over certain time interval, where the CRW fluctuations are continuous in time. This is graphically shown in Figure 14.

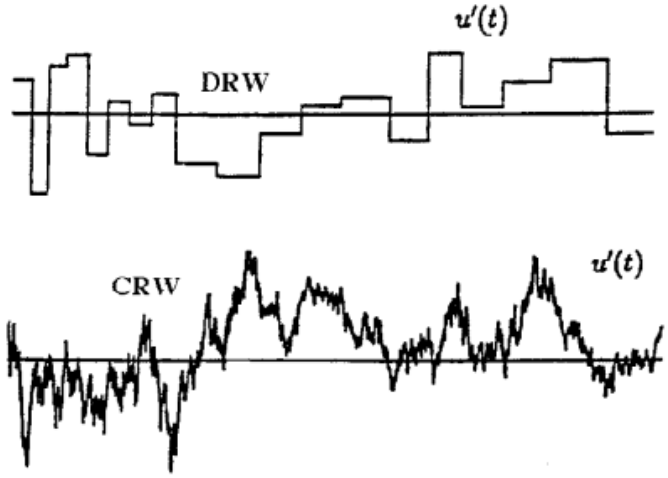

Figure 14: The velocity fluctuation of the DRW and CRW models (Bocksell & Loth, 2001)

2.4 Movement of particles through air

The single droplet model has been used by many researchers to gain knowledge about evaporation, dispersion, settling and migration of water droplets (Redrow et al., 2011). In this paragraph some basic principles are described. Among these are the equations of motion, the Reynolds number and the particle momentum response time.

Liu and Zhai (2007) identify three types of models used in CFD for prediction of droplet movement in air (X. Liu & Zhai, 2007):

- Lazy particle model
- Isothermal particle model
- Vaporizing droplet model

The lazy particle model follows the streamlines in every point of a flow field, which is the Eulerian approach. Size of droplets and temperature are not taken into account. The isothermal and vaporizing models are Lagrangian and take into account the size of the droplets while solving the equation however not the temperature of the particle itself. It is also assumed that particles do not evaporate and remain the same in size. The vaporizing model does take into account the exchange of heat and mass between particle and its environment and is therefore the most complete of the three models. The effect of heat and mass transfer is relevant when predicting virus-laden droplet trajectories (X. Liu & Zhai, 2007).

2.4.1 Equations of motion

From Newton's second law the governing equations for the motion of a droplet are known. The change in momentum per time unit is equal to the total force acting on it (Cheng et al., 2020):

$$\frac{d\vec{p}}{dt} = \vec{F} \tag{23}$$

With the momentum equal to:

$$\vec{p} = m\vec{v} \tag{24}$$

Where m is the droplet mass and v the droplet velocity.

In the following 2D model we define the positive x-direction from the left to the right and the positive z-direction upward (which differs from Cheng et al., 2020). Combining Eq. (23) and (24) then gives:

$$\frac{dp_x}{dt} = m\frac{dv_x}{dt} + v_x\frac{dm}{dt} = -F_{dx} - F_s \tag{25}$$

$$\frac{dp_z}{dt} = m\frac{dv_z}{dt} + v_z\frac{dm}{dt} = F_b - F_{dz} + F_s - F_g \tag{26}$$

p_x and p_z are the momentum components and v_x and v_z the velocity components. The forces on a droplet are gravity force F_g, buoyancy force F_b and drag force F_d and are schematically shown in Figure 15 below. F_s is the force destructing the momentum of vapor from evaporation.

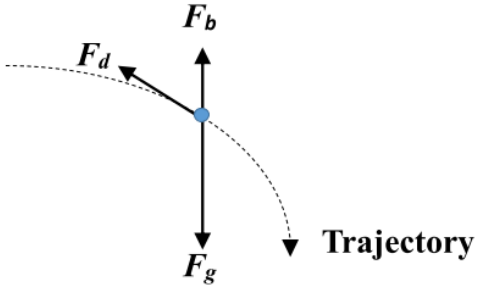

Figure 15: Forces acting on a droplet (Cheng et al., 2020).

For spheres the above mentioned forces are expressed as:

$$F_g = \frac{4\pi}{3}\rho_p g R^3 \tag{27}$$

$$F_b = \frac{4\pi}{3}\rho_f g R^3 \tag{28}$$

$$F_d = \frac{1}{2}C_d \rho_f v^2 \pi R^2 \tag{29}$$

With ρ_p the density of a water droplet, ρ_f air density, R the radius of the droplet, g the gravitational acceleration, v the velocity components and C_d the drag coefficient.

The velocity v is defined as:

$$v = \sqrt{v_x^2 + v_z^2} \tag{30}$$

The components of F_D are defined by the ratio between the velocity and drag force:

$$\begin{aligned} F_{dx} &= \frac{F_d v_x}{v} \\ F_{dz} &= \frac{F_d v_z}{v} \end{aligned} \tag{31}$$

Plugging in Eq. (27) - (31) into Eq. (25) and (26):

$$m\frac{dv_x}{dt} = -\frac{1}{2}C_d \rho_f \pi R^2 v_x \sqrt{{v_x}^2 + {v_z}^2} \tag{32}$$

$$m\frac{dv_z}{dt} = \frac{4\pi}{3}\rho_f g R^3 - \frac{1}{2}C_d \rho_f \pi R^2 v_z \sqrt{{v_x}^2 + {v_z}^2} - \frac{4\pi}{3}\rho_p g R^3 \tag{33}$$

The force F_s is not included because it only affects the motion indirectly, namely because of the size decrease due to evaporation. The mass m of a droplet is equal to:

$$m = \frac{4\pi}{3}\rho_p R^3 \tag{34}$$

This results in the following system of differential equations:

$$\begin{aligned} \frac{dv_x}{dt} + \frac{3C_d}{8R}\frac{\rho_f}{\rho_p} v_x \sqrt{v_x^2 + v_z^2} &= 0 \\ \frac{dv_z}{dt} + \frac{3C_d}{8R}\frac{\rho_f}{\rho_p} v_z \sqrt{v_x^2 + v_z^2} &= \left(\frac{\rho_f}{\rho_p} - 1\right) g \end{aligned} \tag{35}$$

With initial conditions $v_x(0) = v_{x0}$, $v_y(0) = v_{y0}$, $v_z(0) = v_{z0}$ and $R(0) = R_0$. Note that only the velocity in z direction (vertical) is influenced by gravity.

For $0.2 \leq R_e \leq 10^3$, the drag coefficient C_d for spheres can be approximated by (Cheng et al., 2020):

$$C_d = \frac{21.12}{R_e} + \frac{6.3}{\sqrt{R_e}} + 0.25 \tag{36}$$

However Wei & Li (2015) defined the drag coefficient as:

$$C_d = \frac{24}{R_e}, R_e \leq 1$$
$$C_d = \frac{24}{R_e}\left(1 + 0.15R_e^{0.687}\right), R_e > 1 \quad (37)$$

2.4.2 Relaxation time and stopping distance

The particle momentum response time or relaxation time τ′ is defined by:

$$\tau' = mB = \rho_p \frac{\pi}{6} d_p^3 \left(\frac{C_c}{3\pi\eta d_p}\right) = \frac{\rho_p d_p^2 C_c}{18\eta} \quad (38)$$

With:

d_p = droplet diameter

ρ = density of water

η = viscosity of air

C_c = slip correction factor defined by:

$$C_c = 1 + \frac{\lambda}{d_p}\left[2.34 + 1.05\exp\left(-0.39\frac{d_p}{\lambda}\right)\right] \quad (39)$$

λ = mean free path of gas

The travel distance S as a function of time t is defined by:

$$S(t) = u_0\tau'\left[1 - \exp(-t/\tau')\right] \quad (40)$$

For an initial velocity of 10 m/s this yields the following table:

Table 5: Stopping distance for several droplet diameters.

d_p (µm)	S (cm)
0.01	0.0000068
0.1	0.000088
1	0.0036
10	0.23
100	12.7

2.5 Interaction of a turbulent buoyant jet with a crossflow

To determine the influence of ventilation on the trajectory of the respiratory particles, we look at the interaction between a turbulent buoyant jet and a crossflow. In this section the assumption is made that the ambient crossflows are uniform with a constant velocity and thus not turbulent.

The ambient crossflow will be denoted by U_a.

List (1982) describes the fundamental parameter when it comes to interaction between jets and crossflows:

> The fundamental parameter in the description of buoyant-jet trajectories in crossflows in the ratio of the length scale $Z_M = M^{1/2}/U_a$ to the equivalent length scale for a plume in a crossflow, defined by $Z_B = B/U_a^3$
>
> Two asymptotic cases occur, corresponding to $Z_M > Z_B$ and $Z_M < Z_B$ and within each case there are three regimes. For $Z_M > Z_B$ jet momentum is dominant and the regimes can be loosely described as "vertical" jet, "bent" jet, and "bent" plume. When $Z_B > Z_M$ jet buoyancy is important so that the regimes can be called vertical jet, vertical plume, and bent plume. In all cases, the buoyancy ultimately controls the trajectory (List, 1982, p. 205).

In case where $z/Z_M < 1$, M dominates the solution meaning the jet is still dominated by the momentum flow. z stands here for the distance from the orifice in the direction of the initial flow. When $z/Z_M > 1$, the crossflow dominates the momentum. The trajectory of a jet in a crossflow is given as (Fischer et al., 1979; Knudsen, 1988):

$$z / z_M = C_1 (x / z_M)^{1/2}, z \ll z_M \tag{41}$$

$$z / z_M = C_2 (x / z_M)^{1/3}, z \gg z_M \tag{42}$$

$$z / z_M = C_3 (x / z_B)^{3/4}, z \ll z_B \tag{43}$$

$$z / z_M = C_4 (x / z_B)^{2/3}, z \gg z_B \tag{44}$$

Where C_1, C_2, C_3 and C_4 are empirically determined constants. These results are asymptotic solutions. The ranges of the values of the constant as given by Fischer et al. (1979) are shown in Table 6.

Table 6: Experimentally determined constants (Fischer et al., 1979).

Constant	C_1	C_2	C_3	C_4
Range of value	1.8 – 2.5	1.44 – 2.1	1.4 – 1.8	$0.82 - 1.4(z_M/z_B)^2$

So based on the proportion of z_m and z_B, the jet will follow the trajectory of

- a jet, bent jet and bent plume for $z_M > z_B$
- a jet, plume and bent plume for $z_M < z_B$

However, this holds when the buoyancy and the momentum flux have the same direction.

2.6 Evaporation

It is clear that the movement of particles through air is highly depending on the size of the droplets. From the moment respiratory particles are exhaled evaporation starts. Respiratory particles are aqueous however not pure water. The droplets humans exhale are sputum and have several constituents. The main constituents are water, sodium chloride (salt), carbohydrate, protein, lipids and DNA (Redrow et al., 2011). In Table 7 both the components of sputum as well as the initial concentration per constituent are shown. Table 8 shows several constants of the different constituents.

Table 7: Initial concentration of sputum components (Redrow et al., 2011).

Component	Concentration (mg/mL)
Water	945
Protein	23.25
Lipid	19.5
Carbohydrate	13.5
DNA	0.834
Salt	9.0

Table 8: Molecular weights and densities of sputum components (Redrow et al., 2011).

Component	Molecular weight (g/mol)	Density (kg/m^3)
Water	18	1000
Protein	58.4	2160
Lipid	66500	1300
Carbohydrate	255	1100
DNA	180.16	1600
Salt	700	1650

However a simplified approach could be used too as described by Cheng et al. (2020). Considering that sputum exists mainly out of water, a droplet consisting 100% of water is considered. The droplet radius R is given by:

$$R = \left[R_0^2 - 2k_1 t \right]^{1/2} \tag{45}$$

With R_0 the initial droplet radius, t the time and k_1 a constant dependent on air temperature, droplet temperature and relative humidity. The droplets are assumed to be non-deforming spheres. The values of the evaporation constant k_1 are given in Table 9.

Table 9: Values of k_1 at initial droplet temperature T_{p0} = 33 °C and air temperature T_f = 18 °C.

RH (%)	0	30	50	70	90
k_1 (μm^2/s)	180	115	74	42	13

According to Wei & Li (2015) droplets evaporate to a droplet nuclei, based on the initial solid volume ratio and the maximum solid volume ratio:

$$d_{p,nuclei} = \left(\frac{\Phi_i}{\psi_{\max}} \right)^{1/3} d_p \tag{46}$$

The initial solid volume ratio Φ_i is given as 1.8% and the maximum ψ_{max} = 0.5236. This results in that the nuclei radius of a given droplet is equal to $0.325d_p$.

Next we present the equations for evaporation of a pure water droplet as given by Redrow et al. (2011).

$$4\pi R^2 \rho_p \frac{dR}{dt} = \pi d_p \rho_c D_v \left(\omega_\infty - \omega_{surf} \right) \tag{47}$$

$$\frac{dT}{dt} = \frac{Nu}{2} \frac{T_a - T}{\tau_t} + \frac{Sh}{2\tau_t} \frac{\Pr}{Sc} \frac{L_v}{c_p} \left(\omega_\infty - \omega_{surf} \right) \tag{48}$$

Here τ_t is the temperature relaxation time and is defined as:

$$\tau_t = \frac{\rho_p c_p d_p^2}{12 k_c} \tag{49}$$

The Nusselt number is defined as:

$$Nu = 2 + 0.6 \,\mathrm{Re}^{1/2} \,\mathrm{Pr}^{1/3} \tag{50}$$

The mass fractions in the free stream and at the droplet surface are defined as:

$$\begin{aligned} \omega_\infty &= \rho_\infty / \rho_c \\ \omega_{surf} &= \rho_{surf} / \rho_c \\ \rho_c &= \left(\rho_{surf} + \rho_\infty \right) / 2 \end{aligned} \tag{51}$$

Where in above equations are:

R	the droplet radius
t	the time
D_v	diffusivity of water vapor in air
T_a	local air temperature
T	instantaneous droplet temperature
ρ_p	the particle density
ρ_c	the representative density given as the average of the surface and free stream
ω_∞	mass fraction in the free stream
ω_{surf}	mass fraction at the droplet surface
L_v	the latent heat of vaporization of water
k_a	the thermal conductivity of air
Nu	Nusselt number
Sh	Sherwood number
Sc	Schmidt number
Pr	Prandtl number

The Sherwood number is defined by the Froessling equation (Steinberger & Treybal, 1960):

$$Sh = 2 + \left(0.552 \right) \mathrm{Re}^{1/2} \, Sc^{1/3} \tag{52}$$

A more complete and complex model takes into account many variables regarding evaporation and components of sputum by e.g. Redrow et al. (2011); Wei & Li (2015); Xie et al. (2007). Redrow et al. (2011) presented a model which takes into account different chemical components, surface tension, relative humidity and the ambient temperature to simulate the evaporation of real-world droplets.

The droplet change rate over time is giving by equation (53)

$$R\frac{dR}{dt}=\frac{D_v M_w e_{sat}(T_a)}{\rho_s R_g T_a}\left\{R_g H-\frac{1}{1+\delta}\exp\left[\frac{L_v M_w}{R_g T_a}\left(\frac{\delta}{1+\delta}\right)+\frac{2M_w\sigma_s}{R_g T_a(1+\delta)\rho_w R}-\frac{M_w\rho_N r_N^3}{\rho_w(R^3-R_N^3)}\sum_y\frac{\nu_y\phi_y R_N^3}{M_y}\right]\right\}$$

(53)

$$\delta=\frac{T}{T_a}-1=\frac{L_v\rho_s}{T_a k_a}R\frac{dR}{dt} \tag{54}$$

With:

R	the droplet radius
t	the time
D_v	diffusivity of water vapor in air
M_w	molecular weight
T_a	local air temperature
T	instantaneous droplet temperature
e_{sat}	saturation vapor pressure
ρ	the density
R_g	the universal gas constant
RH	the relative humidity as a fraction
L_v	the latent heat of vaporization of water
σ	the surface tension
φ_y	the practical osmotic coefficient
ν_y	the number of ions into which a solute molecule dissociates
ε_y	the mass fraction of a constituent y with respect to the total dry mass
k_a	the thermal conductivity of continuous phase (air)

The subscripts w and s stand for water and solution of droplets respectively. Subscript N is the reference to a dry particle while y refers to a particular constituent of the particle.

The relative humidity RH, saturation vapor pressure e_{sat} and partial vapor pressure e_v are given by equations (55) - (57).

$$RH=\frac{e_v}{e_{sat}} \tag{55}$$

$$e_{sat}=6.1121\left(1.0007+3.46e^{-6}P\right)\exp\left(\frac{17.502T_a}{240.97+T_a}\right) \tag{56}$$

With e_{sat} in millibars when the ambient air pressure P, is also in millibars.

$$e_v=\left(\frac{T_a-T_\infty}{T_0-T_\infty}\right)e_{v,0}+\left(1-\frac{T_a-T_\infty}{T_0-T_\infty}\right)e_{v,\infty} \tag{57}$$

The change rate of droplet temperature is given as:

$$\frac{d}{dt}(T_a-T)=\frac{-3}{R^2\rho_s c_{ps}}\left\{k_a(T_a-T)+L_v D_v(Q_\infty-Q_{surf})\right\} \tag{58}$$

Where C_{ps} is the specific heat of the droplet, k_a the thermal conductivity and Q_∞ and Q_{surf} are the ambient and surface water vapor density. The surface water vapor density is given by:

$$Q_{surf} = \frac{100 M_w e_{sat}}{R_g T} \exp\left\{ \frac{2 M_w \sigma_s}{R T_a \rho_w R} - \frac{M_w \rho_N R_N^3}{\rho_w (R^3 - R_N^3)} \sum_y \frac{\nu_y \phi_y \varepsilon_y}{M_y} \right\} \tag{59}$$

3. Models

In this chapter three particle tracking models are presented, each with increasing complexity. The characteristics of the models will be described using the results of the literature study and by adding own interpretations. The implementation of these models in the programming language Python will be explained. The final Python scripts will be added to the appendix. Model 1 is a simplified model describing the trajectories of large respiratory particles. Model 2 describes a turbulent buoyant jet which predicts the dispersion of particles. Model 3 shows the influence of an ambient crossflow on the turbulent jet.

3.1 Model 1: Simplified model for large respiratory droplets

This model uses the model described by Cheng et al. (2020) as a starting point. A 2D model was presented however here we propose a 3D model by adding the transverse y-axis, as the streamwise axis x and vertical axis z had been given already. The equation for the y-direction are the same as for the x-direction.

$$\frac{dp_y}{dt} = m\frac{dv_y}{dt} + v_y\frac{dm}{dt} = -F_{dy} - F_s \tag{60}$$

Since the particle is able to have a velocity component in the y-direction, Eq. (30) needs to be updated:

$$v = \sqrt{v_x^2 + v_y^2 + v_z^2} \tag{61}$$

When there is an ambient airflow, the velocity components in all directions need to be added to Eq. (29), because the drag force F_d is determined by the relative velocity of the particle:

$$F_d = \frac{1}{2}C_d\rho_f\pi R^2\sqrt{(v_x-u_x)^2+(v_y-u_y)^2+(v_z-u_z)^2}^2 \tag{62}$$

The drag forces in the three axes then become:

$$\begin{aligned} F_{dx} &= \frac{F_d(v_x-u_x)}{v} \\ F_{dy} &= \frac{F_d(v_y-u_y)}{v} \\ F_{dz} &= \frac{F_d(v_z-u_z)}{v} \end{aligned} \tag{63}$$

Where the relative velocity v now is equal to:

$$v = \sqrt{(v_x-u_x)^2+(v_y-u_y)^2+(v_z-u_z)^2} \tag{64}$$

The system of equations in (35) becomes:

$$\begin{aligned} &\frac{dv_x}{dt} + \frac{3C_d}{8R}\frac{\rho_f}{\rho_p}(v_x-u_x)v = 0 \\ &\frac{dv_y}{dt} + \frac{3C_d}{8R}\frac{\rho_f}{\rho_p}(v_y-u_y)v = 0 \\ &\frac{dv_z}{dt} + \frac{3C_d}{8R}\frac{\rho_f}{\rho_p}(v_z-u_z)v = \left(\frac{\rho_f}{\rho_p}-1\right)g \end{aligned} \tag{65}$$

For $A = \frac{3C_d}{8R}\frac{\rho_f}{\rho_p}$, Eq. (65) becomes:

$$\begin{aligned}
&\frac{dv_x}{dt} + A(v_x - u_x)v = 0 \\
&\frac{dv_y}{dt} + A(v_y - u_y)v = 0 \\
&\frac{dv_z}{dt} + A(v_z - u_z)v = \left(\frac{\rho_f}{\rho_p} - 1\right)g
\end{aligned} \tag{66}$$

Then we solve the equations semi-implicitly:

$$\begin{aligned}
&\frac{v_x(t+\Delta t) - v_x(t)}{\Delta t} + A(v_x(t+\Delta t) - u_x)v(t) = 0 \\
&v_x(t+\Delta t) - v_x(t) = -\Delta t A(v_x(t+\Delta t) - u_x)v(t) \\
&(1 + \Delta t A v(t))v_x(t+\Delta t) = v_x(t) + \Delta t A u_x v(t) \\
&v_x(t+\Delta t) = \frac{v_x(t) + \Delta t A u_x v(t)}{1 + \Delta t A v(t)}
\end{aligned} \tag{67}$$

In similar way the other equations of (66) are solved to obtain:

$$\begin{aligned}
v_x(t+\Delta t) &= \frac{v_x(t) + \Delta t A u_x v(t)}{1 + \Delta t A v(t)} \\
v_y(t+\Delta t) &= \frac{v_y(t) + \Delta t A u_y v(t)}{1 + \Delta t A v(t)} \\
v_z(t+\Delta t) &= \frac{v_z(t) + \Delta t\left(A u_z v(t) + \left(\frac{\rho_f}{\rho_p} - 1\right)g\right)}{1 + \Delta t A v(t)}
\end{aligned} \tag{68}$$

Now the velocity in each time step can be calculated. Now the trajectory of particles is calculated by multiplying the velocity and the timestep. Here we propose a central difference scheme to calculate the particle's next location S_i:

$$S_i(t+\Delta t) = S_i(t) + \frac{v_i(t) + v_i(t+\Delta t)}{2}\Delta t \tag{69}$$

3.2 Model 2: Model of a turbulent exhalation jet

In this paragraph the numerical approach and intermediate results are presented to explain and validate model 2. Primarily the turbulent jet is presented, then the particle tracking model including the dispersion pattern and particle spread and finally the evaporation.

3.2.1 The isothermal turbulent jet

Firstly a 3D-frame of data points is created. The centreline of the jet is the starting point of the frame. The underlying idea is that all main equations (4) - (22) are based on the centreline and some radial distance r from the centreline. Because of the jets circular shape, it could be divided into twelve equal segments, each with radius r and an angle θ of $\pi/6$. As the jet expands along the streamwise direction the radius increases. For each given streamwise distance x, the corresponding radius with length equal to the corresponding top-hat boundary is linearly divided in 10 segments plus 5 additional ones laying outside of the jet top-hat boundaries. In Figure 16 the frame is shown in two perspectives.

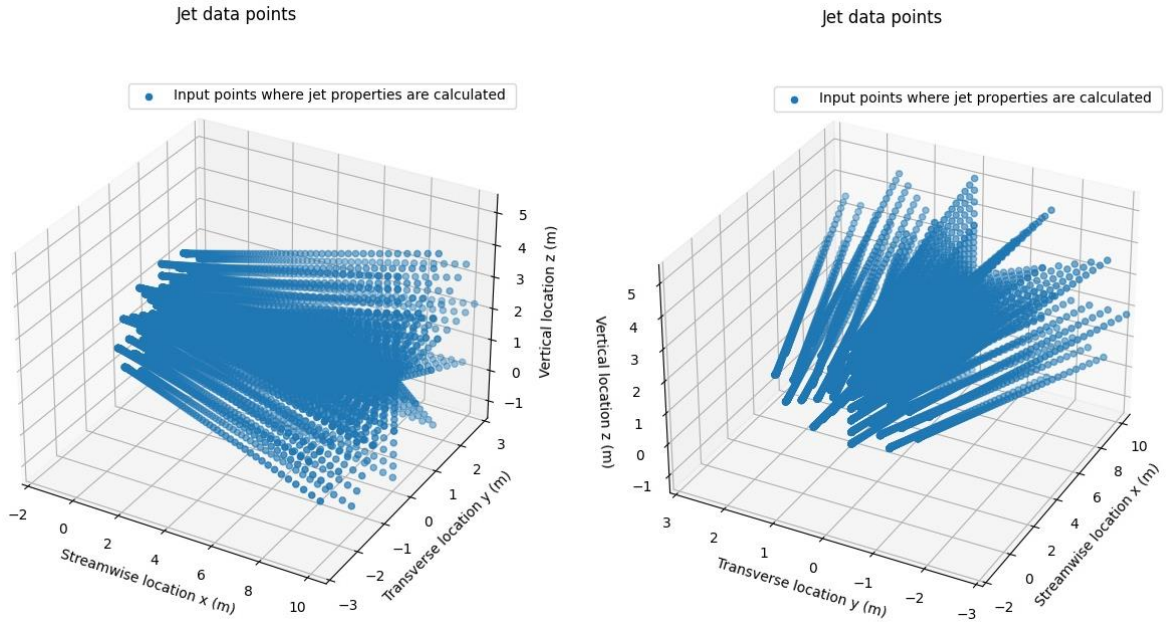

Figure 16: Jet data point frame from two perspectives. The origin of the jet is at z = 2 m and the length of the curve reaches x = 10 m.

With the coordinates and radial distances known the streamwise velocity, transverse velocity, temperature profile, velocity fluctuation and dissipation rates are calculated.

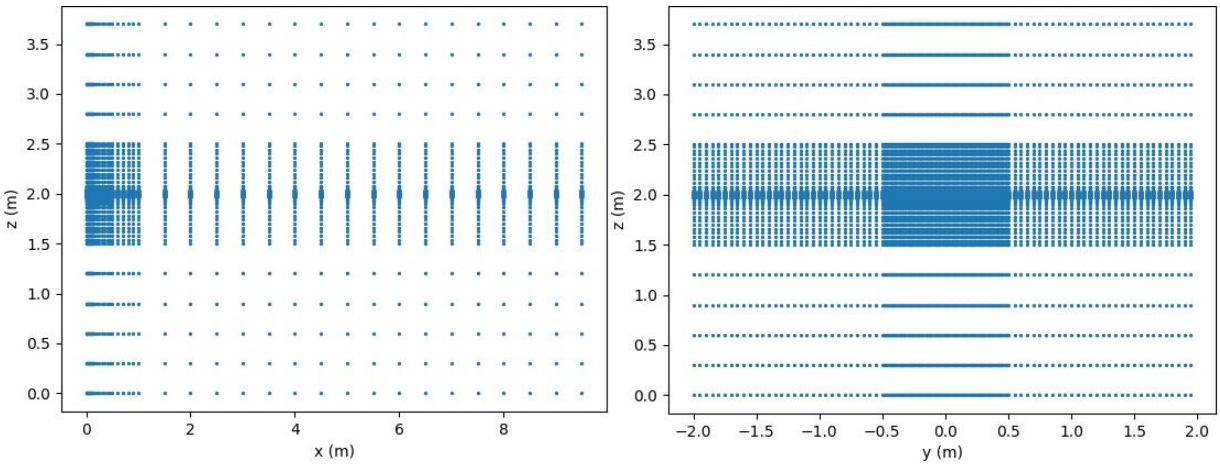

Figure 17: Interpolation grid in the x-z plane (left) and x-y plane (right).

To make the obtained values usable they have to be interpolated over a rectangular grid. This simplifies and increases the calculation speed in the particle tracking model, which will be discussed later. The calculated jet properties have high change rates around the origin and the centreline of the jet. Therefore the interpolation grid has larger density around the centreline, see Figure 17.

After interpolation the results are checked by plotting e.g. the velocity in x and z direction in the plane y = 0. When the interpolation is done adequately, a Gaussian velocity profile should be obtained along the x-axis.

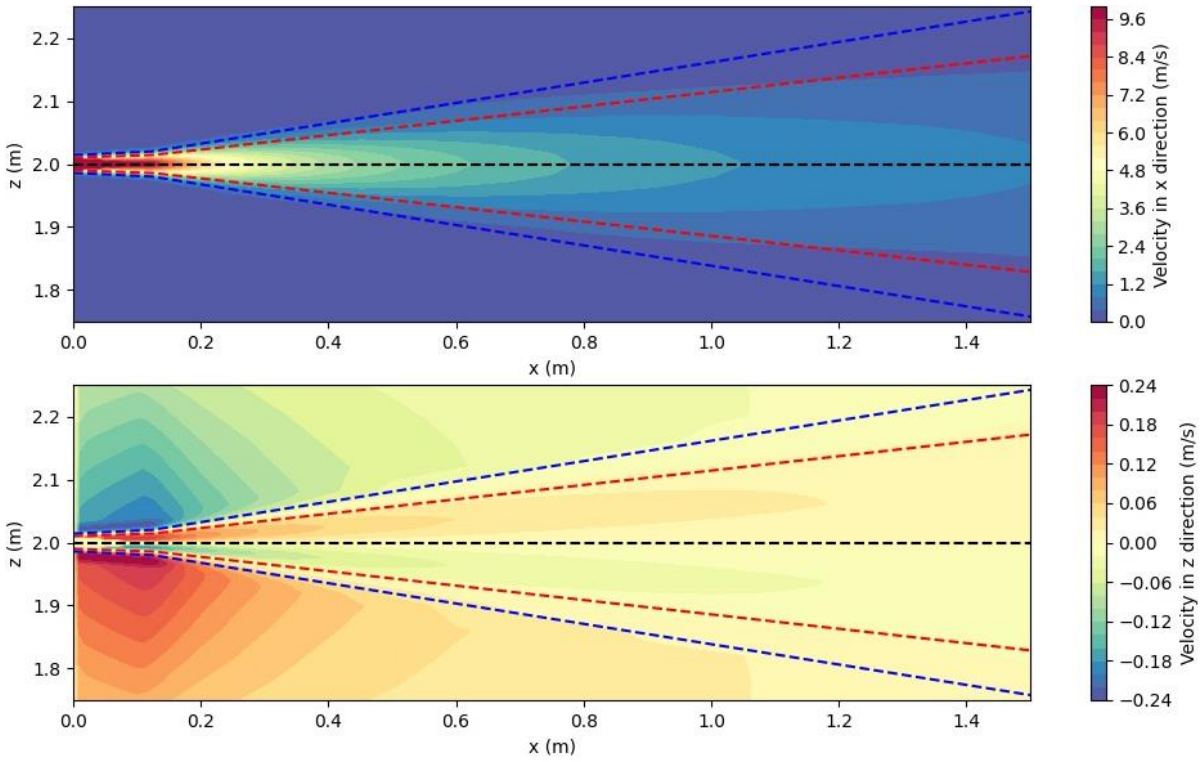

Figure 18: Velocity profiles in the plane y = 0. The x-velocity profile (top) is Gaussian and the z-velocity profile (bottom). The figure shows a non-buoyant jet with u_0 = 10 m/s. The red and blue dashed lines represent the Gaussian half-width and the top-hat boundaries.

The axial velocity of the turbulent jet develops in a Gaussian profile, in agreement with the analytical equation (4). The horizontal velocity decreases to 20% of the initial velocity at a distance of 1 m.

As can be seen from Figure 18 the radial mean velocity switches sign at the jet boundary. While this might seem peculiar at first, it actually shows the actual behaviour of a turbulent jet, where at the boundary layer air from the jet and ambient air mix, causing the jet to expand over distance.

3.2.2 The buoyant turbulent jet

The buoyant turbulent jet is very similar to the isothermal turbulent jet. The main difference is found in the trajectory of the jet, which is an upward curve due to the buoyancy difference from the warmer exhaled air in comparison with the ambient air. The calculation of the velocity profiles, temperature profile and turbulence quantities works the same: the values along the centreline are calculated and change over some radial distance r.

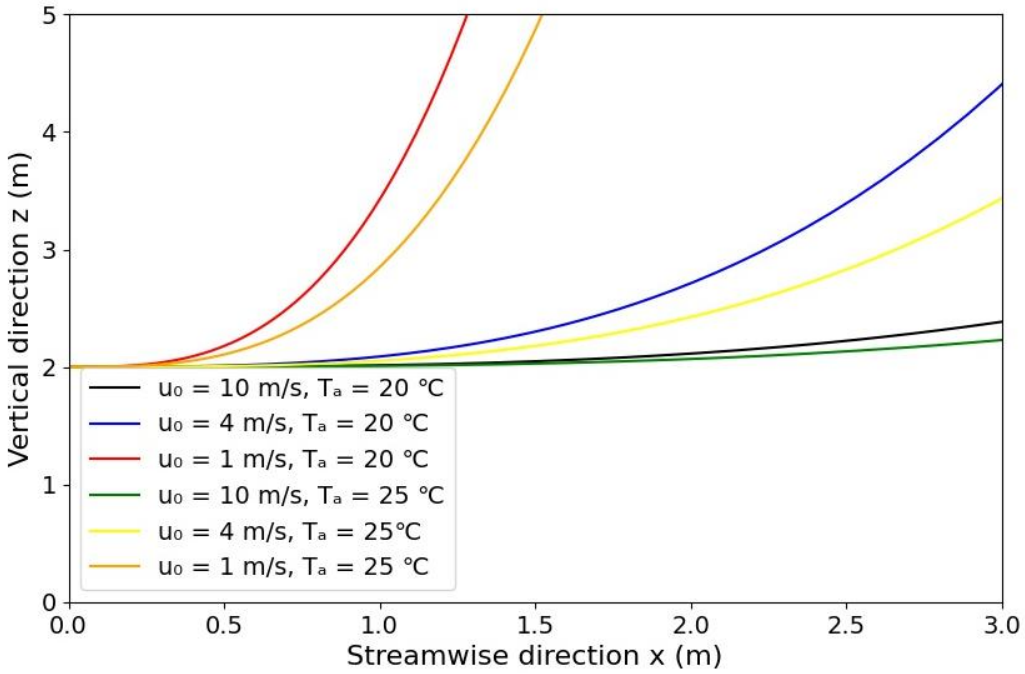

Figure 19: Trajectory centrelines for buoyant jets with several initial velocities and temperatures.

Due to the curve of the jet, the calculated velocities need to be decomposed into velocities along the x-, y- and z-axis. Rotation matrices are used to obtain the decomposed vectors. The rotation matrices along the x and y axis are shown in Eq. (70) and (71).

The following steps need to be executed:

- Rotate the radius r = (0, 0, r) by the slope of the centreline φ
- Rotate the coordinate system by φ
- This means the coordinate of the initial radius in the original coordinate system is equal to the rotated radius in the new coordinate system which is (x, y, z) = (0, 0, r)
- Rotate the radius over x' by an angle θ to obtain the coordinates of the radius in the translated system
- Rotate the translated system back to the original system to obtain the coordinates in the original system
- With these coordinates the velocity and temperature in the 3D jet can be determined

$$R_x(\theta) = \begin{pmatrix} 1 & 0 & 0 \\ 0 & \cos\theta & -\sin\theta \\ 0 & \sin\theta & \cos\theta \end{pmatrix} \quad (70)$$

$$R_y(\theta) = \begin{pmatrix} \cos\theta & 0 & \sin\theta \\ 0 & 1 & 0 \\ -\sin\theta & 0 & \cos\theta \end{pmatrix} \quad (71)$$

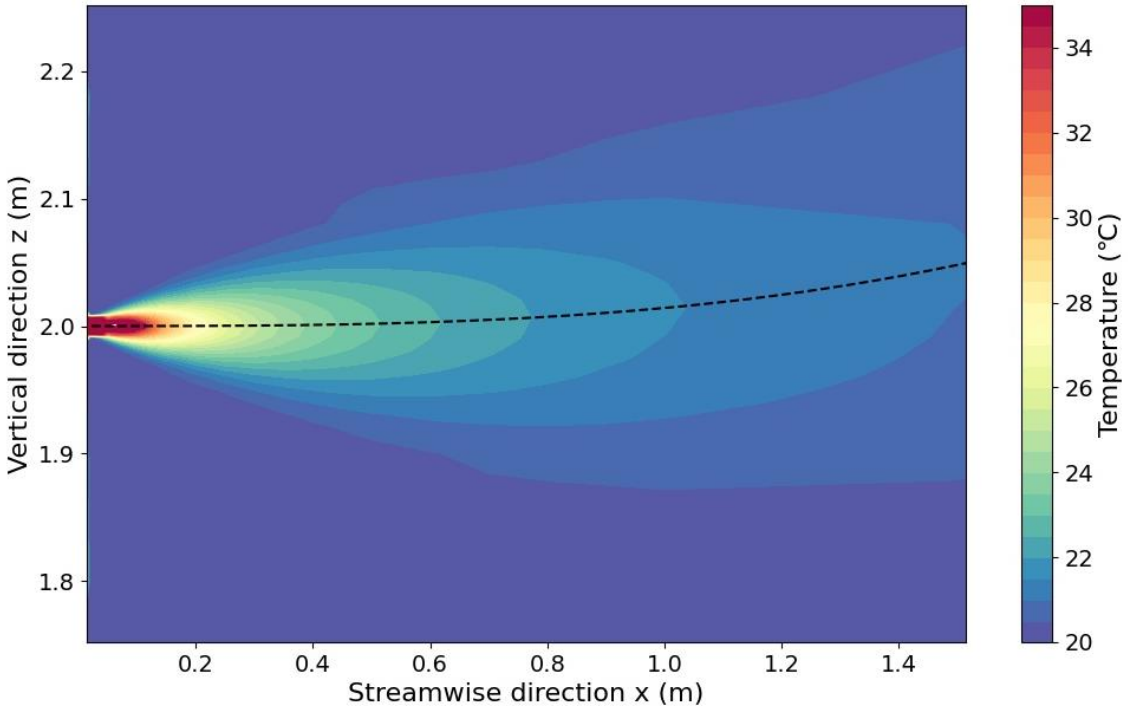

Figure 20: Temperature profile of a buoyant jet with initial temperature T_0 = 35 °C and ambient temperature T_a = 20 °C.

The temperature and water vapour density have the same profile, in accordance with Eq. (6) & (7). At the jet orifice we find the highest temperature and fully saturated air. Along the jet centreline the highest temperatures and densities are found. A decrease can be seen at a radial distance from the centreline, similar to the streamwise velocity profile.

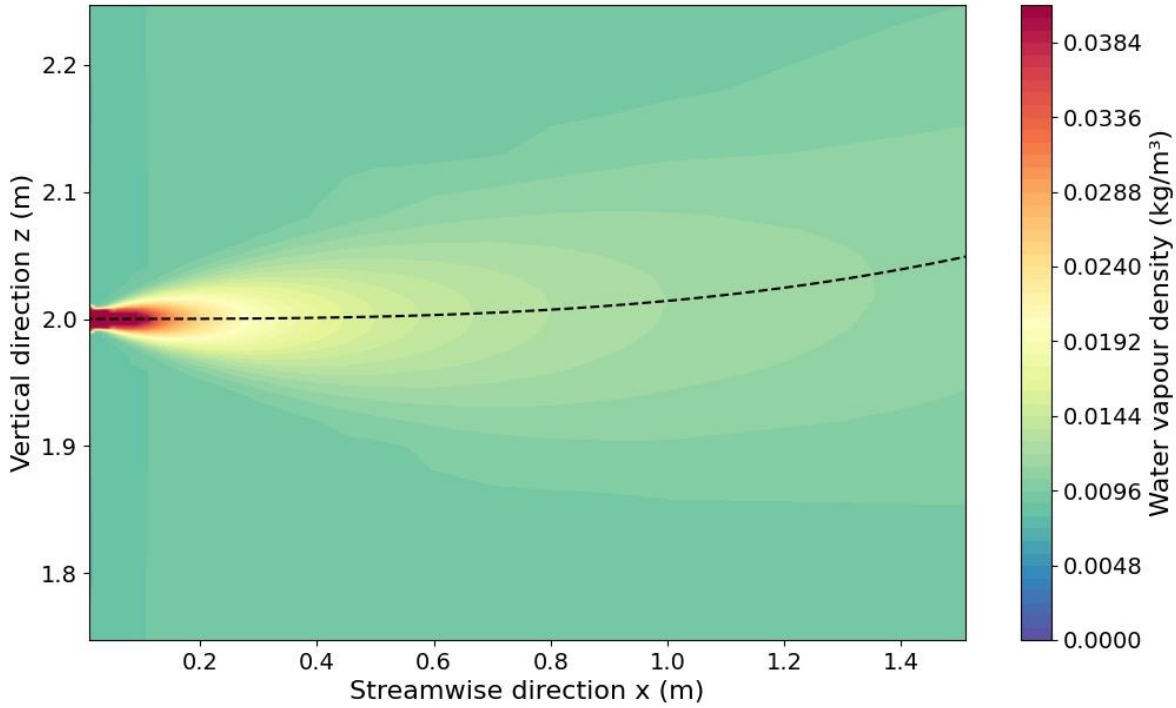

Figure 21: Water vapour density profile of a buoyant jet with initial temperature T_0 = 35 °C and ambient temperature T_a = 20 °C

3.2.3 Particle tracking

The mouth is represented by a circle with diameter d_0 = 0.02 m. In the model presented by Wei & Li (2015) the mouth area is divided into 100 subregions and each particle is randomly released from one of them. Another method to randomly release particles from any point in the mouth opening is proposed here:

Let ρ be defined as the square root of a random number from a uniform distribution with lower boundary zero and upper boundary r^2, with r the radius of the circle. The upper boundary is chosen this way because the area of a circle corresponds to its radius squared. Would the upper boundary be chosen equal to r, the amount of chosen points would be significantly higher closer to the origin.

Let φ be a randomly chosen angle from a uniform distribution with lower boundary zero and upper boundary 2π.

Then the coordinate of a randomly selected particle release location is equal to:

$$(y, z) = \rho \cdot (\cos(\varphi), \sin(\varphi)) \tag{72}$$

Figure 22 shows an example of this method where 500 particles have randomly been distributed over a circle with diameter = 0.02 m. The different colors are used for contrast and have no further meaning in this context.

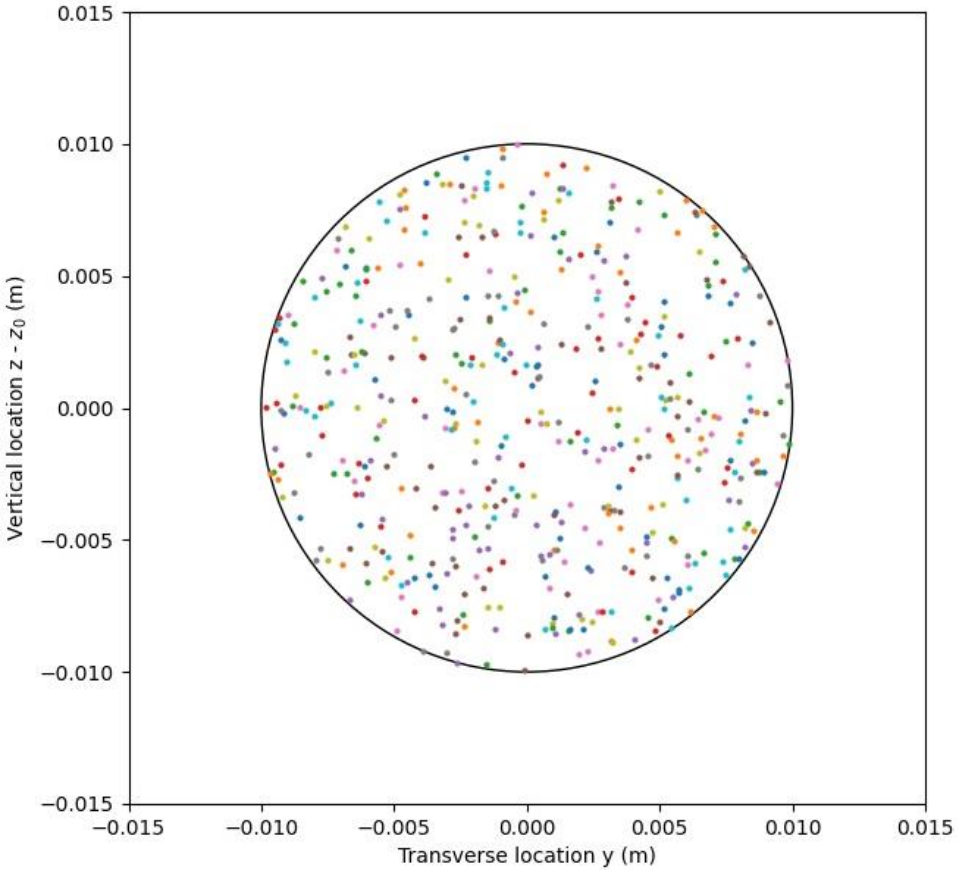

Figure 22: uniformly generated locations of 500 particles in a circular mouth model (d_0 = 0.02 m).

Then the trajectories of the particles are calculated by releasing them in the jet making use of the DRW model. The goal is to be able to validate the model and thus the initial parameters are set as the parameters in the model of Wei & Li (2015). Their results and the results of this research will be presented side to side. The particle dispersion pattern, particle reach probability and particle spread will be compared.

3.2.4 Evaporation

The pure water droplet evaporation model from Redrow et al. (2011) is used. To obtain results with a relative small error using a reasonable time step, implicit integration is used.

Solving Eq. (47) implicitly we obtain:

$$
\begin{aligned}
&4\pi R^2 \rho_p \frac{R(t+\Delta t)-R(t)}{\Delta t} = \pi d_p \rho_c D_v \left(\omega_\infty - \omega_{surf}\right) \\
&\frac{R(t+\Delta t)-R(t)}{\Delta t} = \frac{2\pi R(t+\Delta t)\rho_c D_v \left(\omega_\infty - \omega_{surf}\right)}{4\pi R(t+\Delta t)^2 \rho_p} \\
&R(t+\Delta t)-R(t) = \frac{\Delta t \rho_c D_v \left(\omega_\infty - \omega_{surf}\right)}{2R(t+\Delta t)\rho_p} \\
&H = \frac{\Delta t \rho_c D_v \left(\omega_\infty - \omega_{surf}\right)}{2\rho_p} \Rightarrow \\
&R(t+\Delta t)^2 - R(t)R(t+\Delta t) - H = 0 \\
&R(t+\Delta t) = \frac{R(t) \pm \sqrt{R(t)^2 + 4H}}{2}
\end{aligned}
\tag{73}
$$

In this case the solution is only valid for the positive root of the quadratic equation.

For the droplet temperature we solve Eq. (48) implicitly:

$$
\begin{aligned}
&\frac{T(t+\Delta t)-T(t)}{\Delta t} = \frac{Nu}{2}\frac{T_a - T(t+\Delta t)}{\tau_t} + \frac{Sh}{2\tau_t}\frac{\mathrm{Pr}}{Sc}\frac{L_v}{c_p}\left(\omega_\infty - \omega_{surf}\right) \\
&G = \frac{Sh}{2\tau_t}\frac{\mathrm{Pr}}{Sc}\frac{L_v}{c_p}\left(\omega_\infty - \omega_{surf}\right) \Rightarrow \\
&\frac{T(t+\Delta t)-T(t)}{\Delta t} = \frac{Nu}{2}\frac{T_a - T(t+\Delta t)}{\tau_t} + G \\
&T(t+\Delta t)-T(t) = \Delta t\left(\frac{Nu}{2}\frac{T_a - T(t+\Delta t)}{\tau_t} + G\right) \\
&\left(1+\frac{Nu}{2\tau_t}\right)T(t+\Delta t) = T(t) + \Delta t\left(\frac{Nu}{2}\frac{T_a}{\tau_t} + G\right) \\
&T(t+\Delta t) = \frac{T(t) + \Delta t\left(\frac{Nu}{2}\frac{T_a}{\tau_t} + G\right)}{\left(1+\frac{Nu}{2\tau_t}\right)}
\end{aligned}
\tag{74}
$$

By applying these formulas simultaneously, the droplet radius and droplet temperature in each next timestep are calculated.

3.3 Model 3: Model of an exhalation jet with turbulence in a uniform crossflow

The ambient flow will be considered a crossflow perpendicular to the exhalation jet in the horizontal xy-plane. The direction of the buoyancy (vertical) and the ambient flow (horizontal) differ from each other. That is why the buoyancy terms defined by Fischer et al. (1979) do not need to be taken into account because we already obtained a well analytically described buoyant jet from other researches.

However the trajectory of the jet in the xy-plane can be described by the asymptotic solutions. The coordinate system used by Fischer et al. (1979) is different than the one formulated in this research. They defined the streamwise direction as z and the direction of the crossflow as x. in our case x is the streamwise direction and y the direction of the crossflow and hence, Eq. (41) – (42) need to be rewritten:

$$\begin{aligned} x / z_M &= C_1 (y / z_M)^{1/2}, x \ll z_M \\ y &= \frac{x^2}{C_1^2 z_M}, x \ll z_M \end{aligned} \tag{75}$$

$$\begin{aligned} x / z_M &= C_2 (y / z_M)^{1/3}, x \gg z_M \\ y &= \frac{x^3}{C_2^3 z_M^2}, x \gg z_M \end{aligned} \tag{76}$$

When x takes on a value around z_M the solution is not given and hence this grey area needs to be defined in a way that the total solution is a continuous function. To solve this, a logistic function containing a sigmoid curve is proposed. The general version of this function is defined as:

$$f(x) = \frac{L}{1 + e^{-k(x - x_0)}} \tag{77}$$

Where x_0 is the midpoint of the sigmoid curve, L is the curve's maximum value and k is called the logistic growth rate (steepness). In our case x_0 is equal to z_M and L is 1. Then the trajectory can be described by:

$$y = \left(1 - \frac{1}{1 + e^{-k(x - z_M)}}\right) \frac{x^2}{C_1^2 z_M} + \frac{1}{1 + e^{-k(x - z_M)}} \frac{x^3}{C_2^3 z_M^2} \tag{78}$$

4. Results & Validation

In this chapter the models in the previous chapter are used to generate results for initial conditions of interest. The models are verified by analysing the intermediate results. In this way it is verified that each additional step in complexity of the model is implemented correctly.

4.1 Model 1

Particles of four different sizes have been entered into the model with an initial velocity of 10 m/s and height of 1.65 m. The ambient air has a velocity of 0 m/s. The simulation ran for 7 seconds with time steps of 0.000025 s to obtain accurate results for comparison.

With ρ_p the density of a water droplet 0.9986 * 10^3 kg/m^3 at 20 °C, ρ_f air density 1.2077 kg/m^3 at 20 °C. The kinematic viscosity v of air at 20 °C equals 1.488*10^{-5} m^2/s.

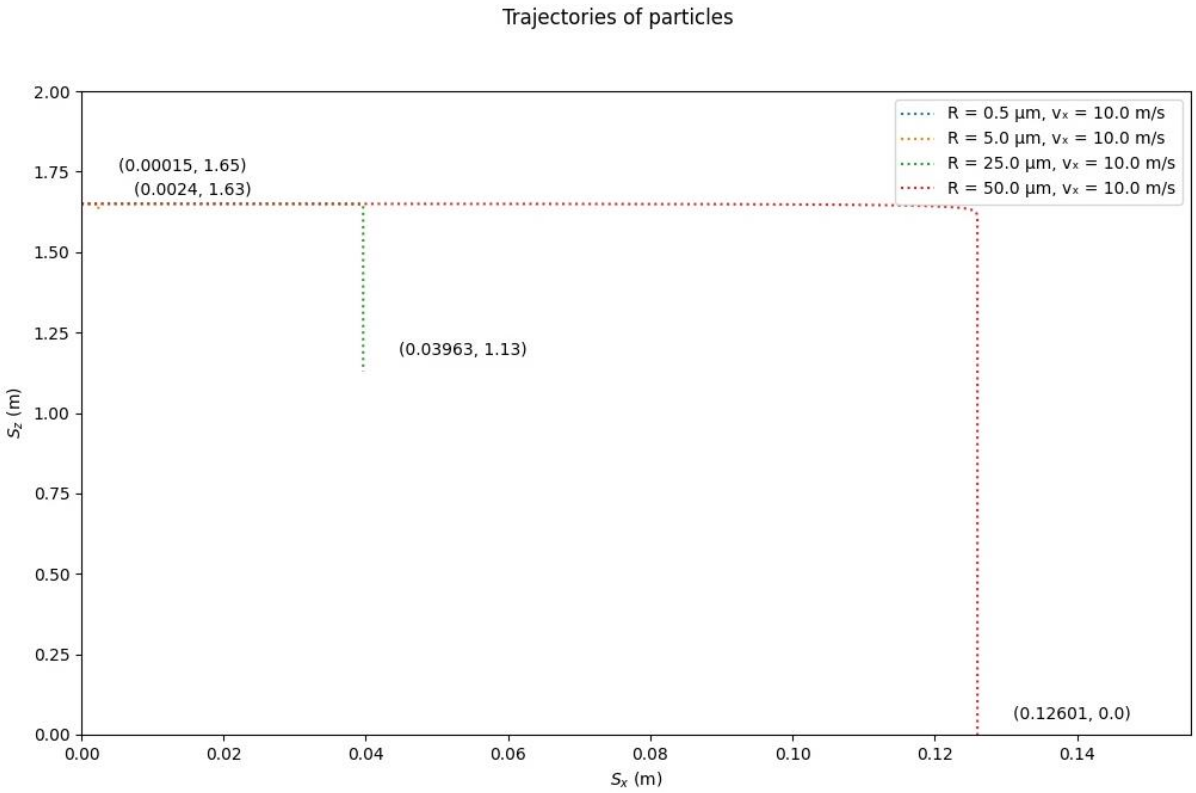

Figure 23: Trajectories of particles of four sizes (d_0 = 1, 10, 50 , 100 µm)

Then we compare it to the stopping distances from Table 5.

Table 10: Comparison of stopping distances from Table 4 and Model 1.

Particle size	Table 4	Model 1
d_p (µm)	S (cm)	S (cm)
1	0.0036	0.015
10	0.23	0.24
100	12.7	12.6

Since model 1 was developed to simulate large respiratory droplets it is logical the discrepancy is smaller for the larger particle sizes and highest for the smallest particles size.

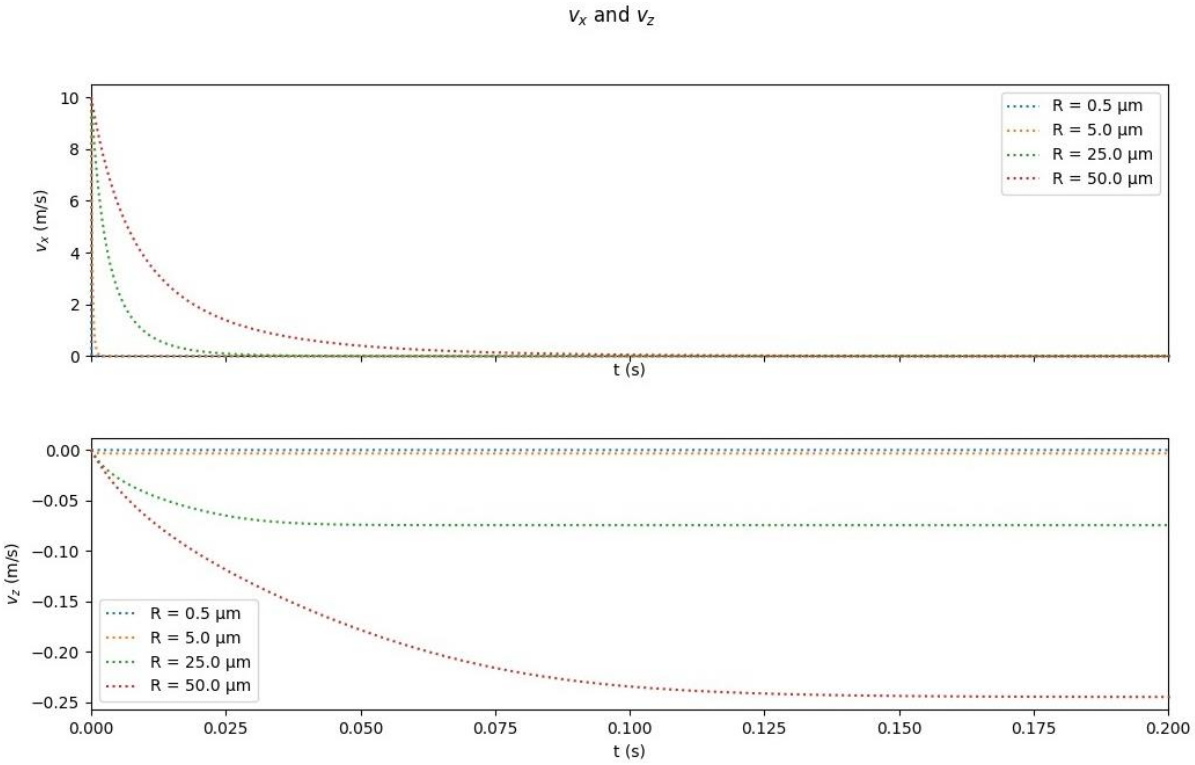

Figure 24: Velocities in x- and z-direction for four different particle sizes

4.2 Model 2

First the results of the non-buoyant jet are shown and validated. In the next subchapter the results of the buoyant jet are displayed and compared. Initially large amounts of three different sizes of particles are investigated to understand the behaviour of these different sizes. Then a distribution of exhaled droplets from the literature is used to determine concentration levels during speaking.

4.2.1 The isothermal turbulent jet

The following results show the dispersion pattern of 3 sizes of particles: 10 µm (blue), 50 µm (black) and 100 µm (brown). Droplets in the range of these sizes are the most common found in the distribution of exhaled particles. A turbulent buoyant-neutral jet is used for this simulation and the integration timestep is 0.001 s. 5000 particles have been released and the simulation does not include evaporation. Figure 25 shows the result of this study and Figure 26 shows the result of Wei & Li (2015).

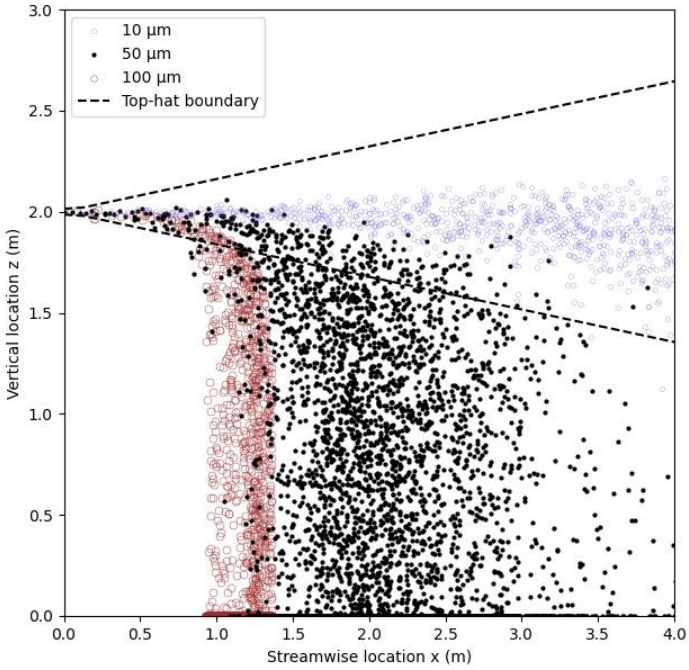

Figure 25: Instantaneous dispersion pattern of particles (t = 50 s) in the turbulent buoyant-neutral jet (d_0 = 2 cm, u_0 = 10 m/s, T_{amb} = 25 °C). The top-hat width boundary of the jet is indicated by the black dashed line.

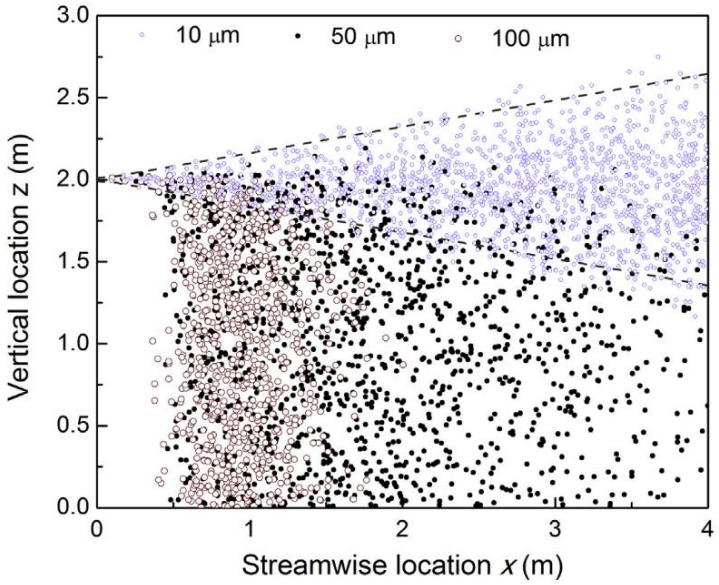

Figure 26: Instantaneous dispersion pattern of particles (t = 100 s) from Wei & Li (2015).

The result is very similar to that of Wei & Li (2015) in Figure 26, yet there exist some differences. They have simulated a larger amount of particles and simulated for 100 s. Moreover the spread of the 10 micron and the 100 micron particles is larger in their study, however the larger particles do follow a similar ballistic trajectory while the smallest particles follow the jet.

This can also be seen in the particle reach probability graph in Figure 27, which is defined as:

$$p(x) = \frac{N_{tot} - N_{dep}(x)}{N_{tot}} \tag{79}$$

with N_{tot} the total number of droplets released and N_{dep} the amount of droplets which have deposited before reaching a certain distance x.

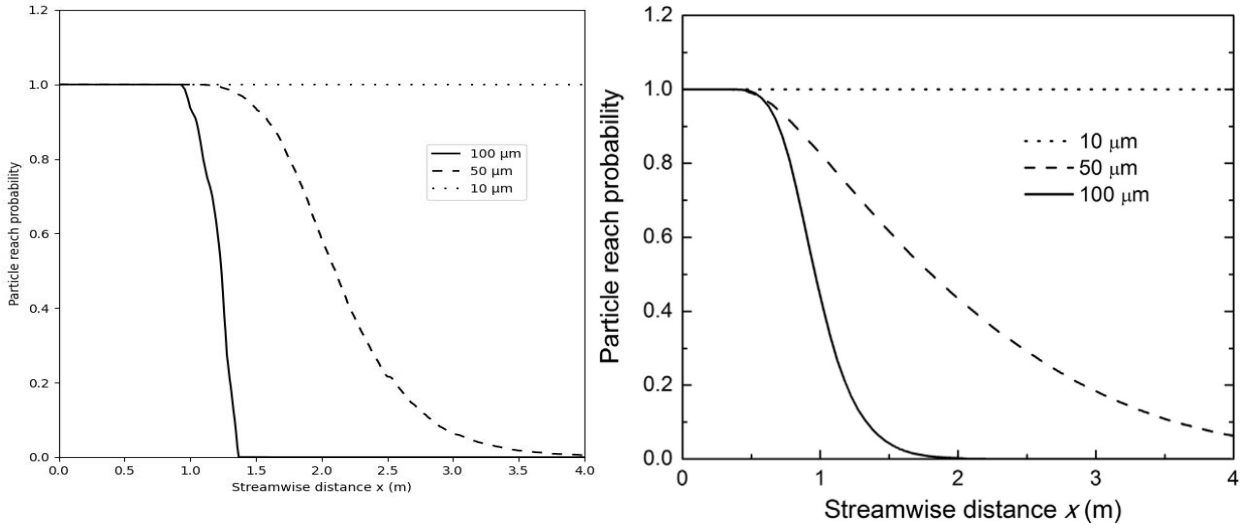

Figure 27: Particle reach probability as a function of the streamwise distance. 5.000 particle trajectories have been calculated in each case in this study (left). 50.000 particle trajectories were calculated by Wei & Li (2015) (right).

In the example study the spread of the larger particles is also seen in the probability reach curve, while the middle sized particles are more comparable. At x = 4 m, the reach probability of this study goes toward zero while in the example the probability also reaches below 10%.

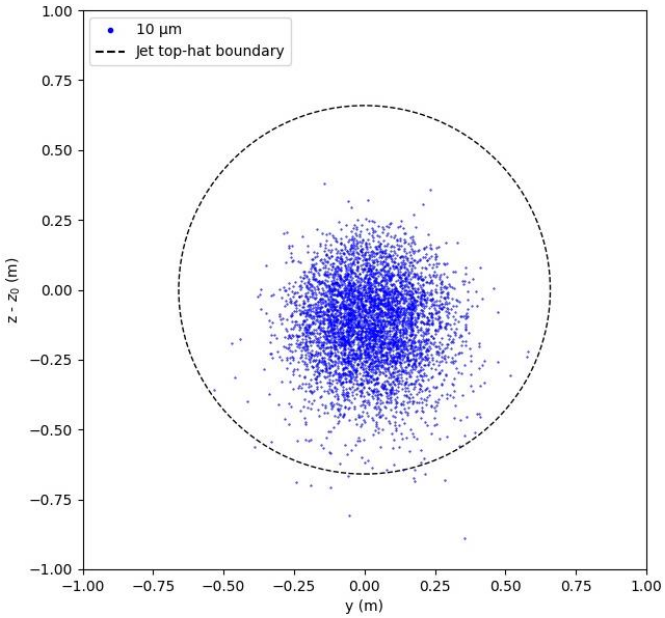

Figure 28: particle spread at x = 4 m for small particles of 10 micron.

Next the particle spread is compared. The main results are comparable where the most droplets stay relatively close to the center of the jet while a smaller amount spreads towards the outer boundary. The gravity seems to have a slightly stronger influence in the results of this study considering that a larger part of the particles are located in the lower section of the jet.

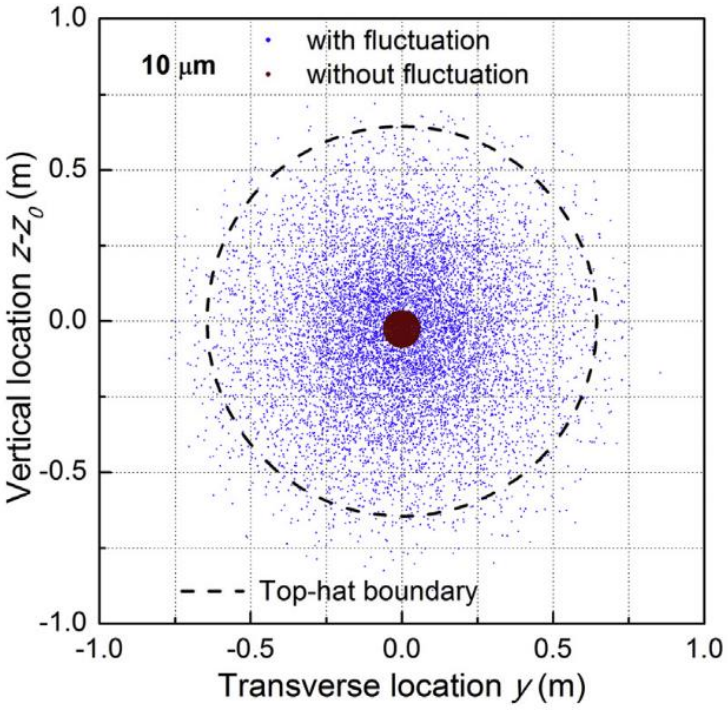

Figure 29: particle spread at x = 4 m from Wei & Li (2015).

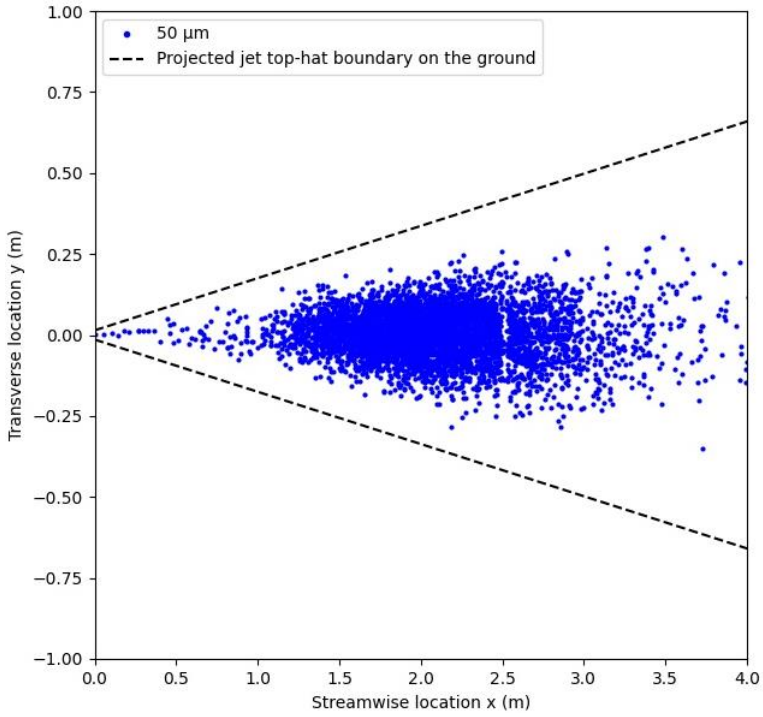

Figure 30: Particle spread of medium particles (d_p = 50 µm) fallen onto the ground. 5.000 particle trajectories have been calculated for 50 s (d_0 = 2 cm, u_0 = 10 m/s, T_{amb} = 25 °C).

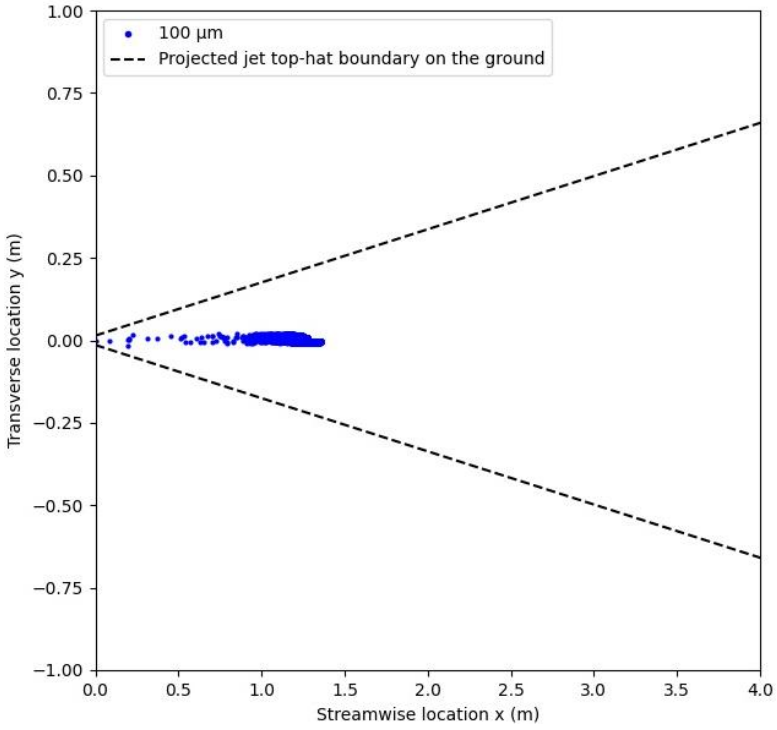

Figure 31: Particle spread of large particles (d_p = 100 µm) fallen onto the ground. 5.000 particle trajectories have been calculated for 50 s (d_0 = 2 cm, u_0 = 10 m/s, T_{amb} = 25 °C).

There is a large discrepancy comparing the results of the particle spread on the ground for the large particles. While it was already evident from the dispersion pattern that the spread in the streamwise direction was different, the transverse spread is also significantly different.

The results for the medium particles are more similar. The differences are similar to those of the smallest particles where in the example model the particles tend to reach closer to the top-hat boundary. Up to this moment we have compared the results based on a calculation with an integration timestep of 0.001 s. In Appendix B the results of the calculation with an integration timestep of 0.01 s are shown. The instantaneous dispersion pattern, the particle spread and the particle reach probability all show equal results. For this reason it is safe to continue with an integration timestep of 0.01 s, which will increase the calculation speed tremendously.

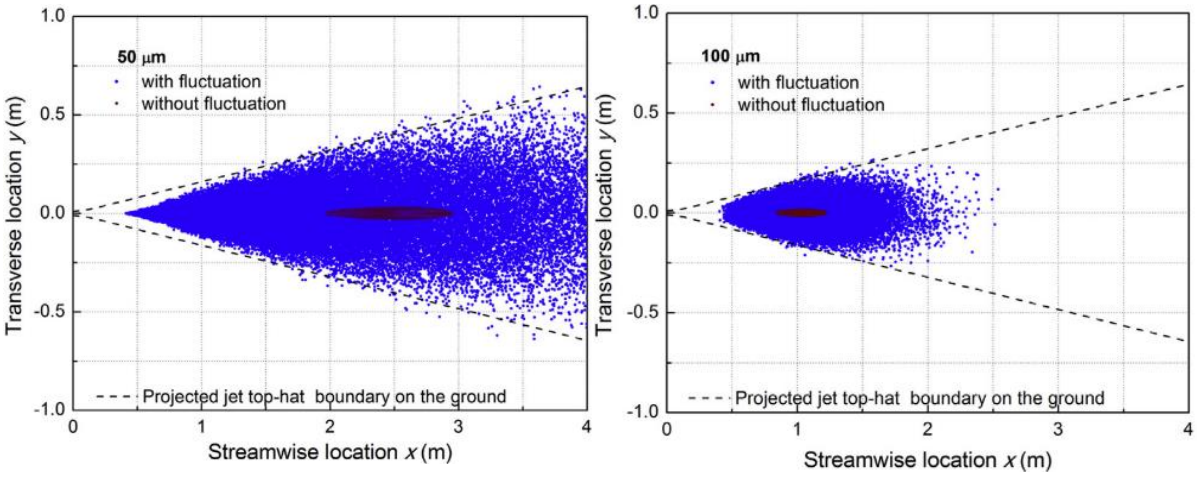

Figure 32: Particle spread of medium and large particles on the ground from Wei & Li (2015)

4.2.2 The buoyant turbulent jet

Firstly we take a look at the evaporation model results. Five different ambient conditions have been simulated for three particles sizes: 10, 50 and 100 µm. One drop of each particle was released at exactly the centre of the jet opening, with a fixed relative humidity, ambient temperature and relative velocity. Here it is assumed all droplet sizes evaporate to 32.5% of their original size. Thus the Kelvin effect is ignored. Wei & Li (2015) took the Kelvin effect into account as can be seen in Figure 35. There, larger droplets evaporate to a larger normalised diameter. The integration timesteps are nonlinear: from 0 to 0.05 s Δt = 5e-6 s, from 0.05 to 10 s Δt = 0.001 s and from 10 to 50 s Δt = 0.1 s. This division is used to generate accurate results for all droplet sizes and is also used to calculate the trajectories of the droplets.

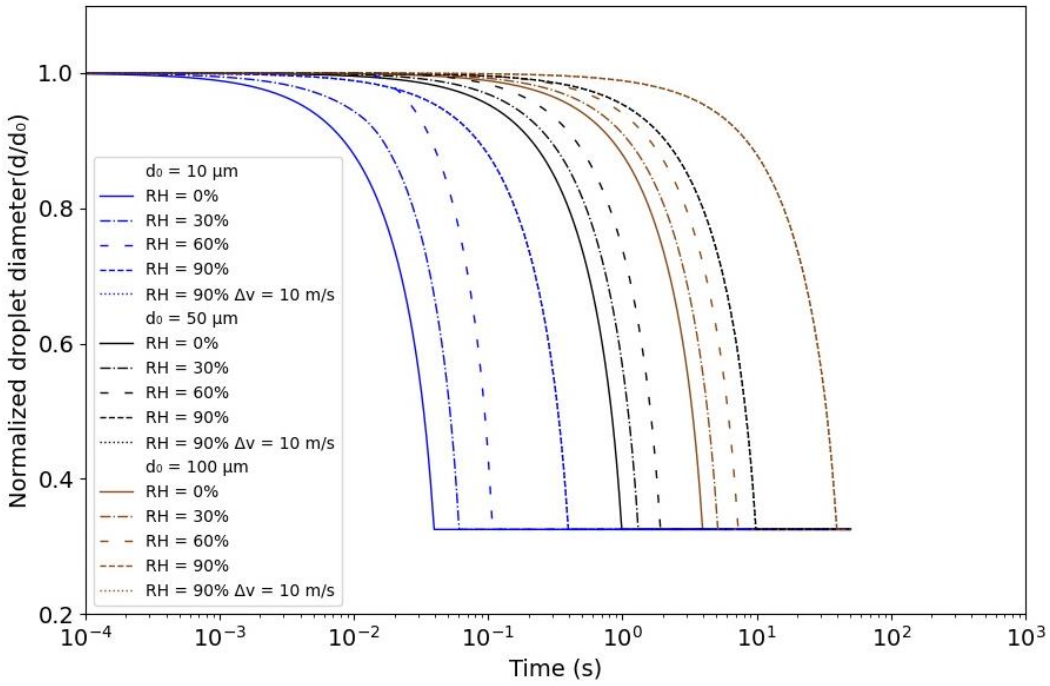

Figure 33: Evaporation of droplets under different conditions. The ambient temperature T_a =25 °C and initial droplet temperature T_0 35 °C.

In this simulation, the different conditions of 90% RH did not result in different evaporation curves, meaning the relative velocity did hardly have any impact. Comparing these results with the ones from Redrow et al. (2011) in Figure 34 we see that the results are very similar.

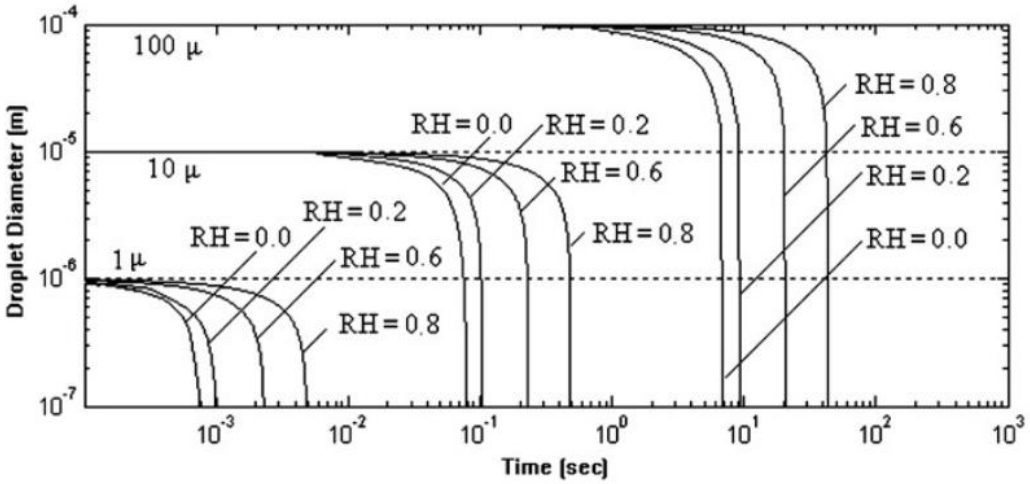

Figure 34: Evaporation curves of pure water droplets from Redrow et al. (2011) with T_a =20 °C and initial droplet temperature T_0 37 °C.

From the evaporation curves it is evident that the relative humidity has a large impact on the evaporation process. Small droplets of 10 μm and smaller evaporate to their nuclei within 1 second. This is however somewhat different than the evaporation curves shown by Wei & Li (2015). The relative velocity between air and droplet also affects the evaporation. The relative velocity increases the speed of evaporation. However this effect is significantly smaller than the effect of relative humidity. Especially considering that the relative velocity between the droplets and the air is in general much smaller than 10 m/s.

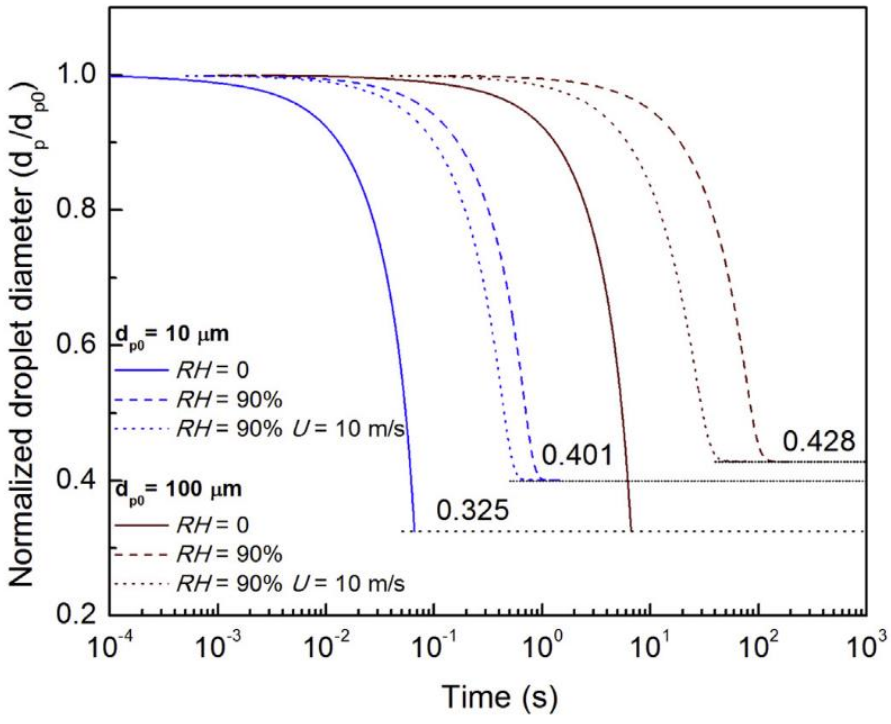

Figure 35: Evaporation curves from Wei & Li (2015).

Under normal conditions the relative humidity in indoor spaces is not 0% nor 90%. For this reason simulations were done with RH = 30%, RH = 50% and RH = 70%. The ambient air temperature is set at 20 °C. Furthermore we distinguish two other conditions: a sneezing or coughing person with an estimated u_0 = 10 m/s initial velocity, a talking person with u_0 = 4 m/s and a calmly breathing person with u_0 = 1 m/s. This results in four distinct cases of which the results are presented in Figure

40 - 37. The corresponding transverse spreads are presented in Appendix B Additional results of Model 2.

As stated before the integration timesteps are nonlinear. Therefore it was chosen to not show the dispersion of droplets in the first 0.1 s. This would result in a large amount of droplets in close proximity of the jet orifice, creating a distorted view of the result. The number of timesteps between 0.1 s and the end of the simulation have been linearly distributed.

First the results of the breathing jet (u_0 = 1 m/s) are shown (Figure 36 - Figure 38). For clarity the x-axis in this case reaches to 1.5 m. The results of the talking and coughing jet are shown with an x-axis reaching 4 m. The three graphs look similar, yet have some differences which can be explained by the difference in relative humidity.

In all of the three cases small droplets settle on the ground within a streamwise distance of 0.2 m. However we see as the relative humidity increases, the amount of droplets decreases. This is the result of evaporation happening faster in conditions of low relative humidity. In the case of 30% RH, the 100 µm droplets have evaporated faster and are therefore lighter. Hence these droplets settle in a longer time compared to conditions of higher relative humidity.

A similar phenomenon happens to the medium sized droplets. In case of low relative humidity, the droplets evaporate quickly to nuclei and become airborne. When evaporation does not happen as fast, the droplets fall out of the jet which is no different as the large droplet behaviour. The only difference is that these droplets need a significant amount more time to settle on the ground.

The smallest droplets are in all cases airborne and move along with the direction of the jet.

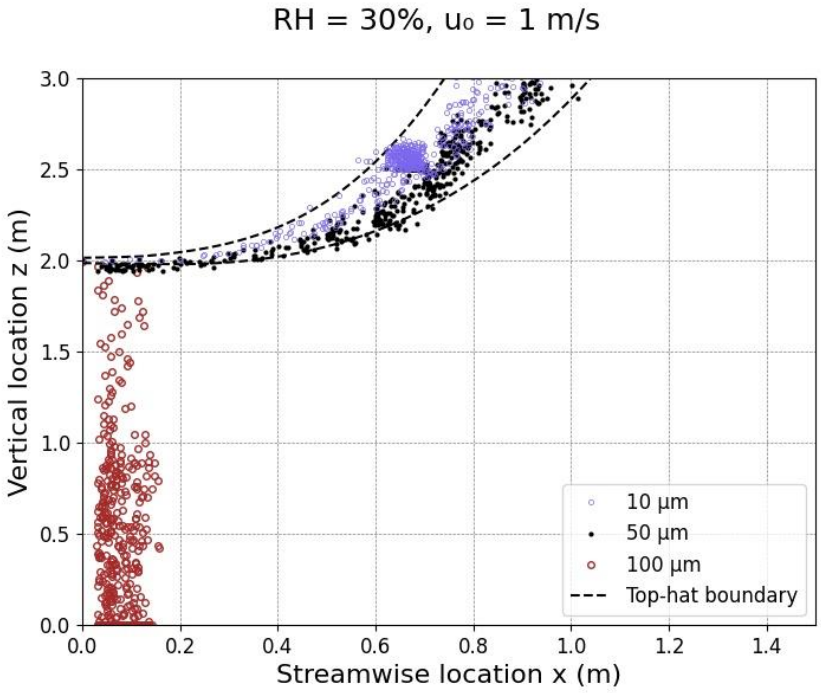

Figure 36: Instantaneous dispersion pattern of 500 droplets (t = 60 s) in the turbulent buoyant jet (d_0 = 2 cm, u_0 = 1 m/s, T_{amb} = 20 °C, RH = 30%).

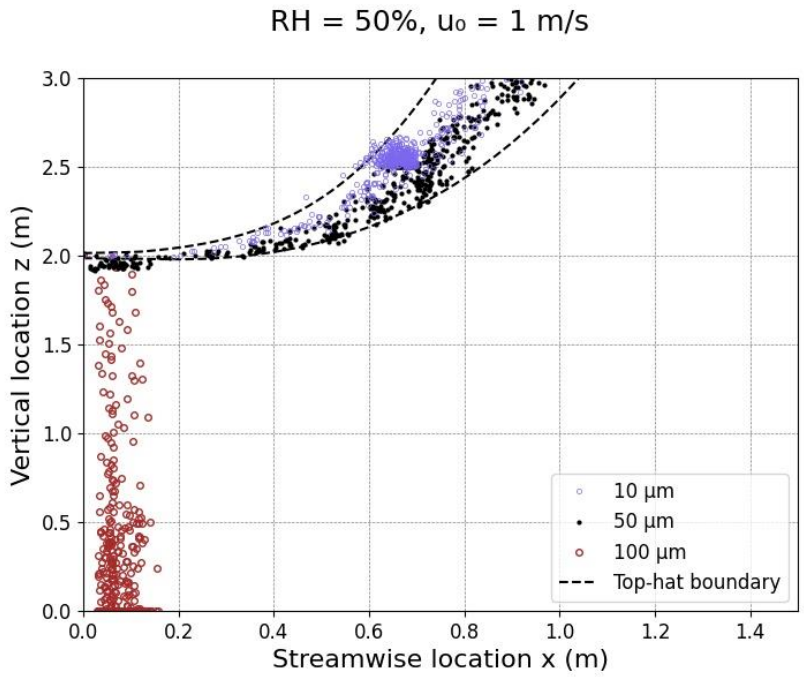

Figure 37: Instantaneous dispersion pattern of 500 droplets (t = 60 s) in the turbulent buoyant jet (d_0 = 2 cm, u_0 = 1 m/s, T_{amb} = 20 °C, RH = 50%).

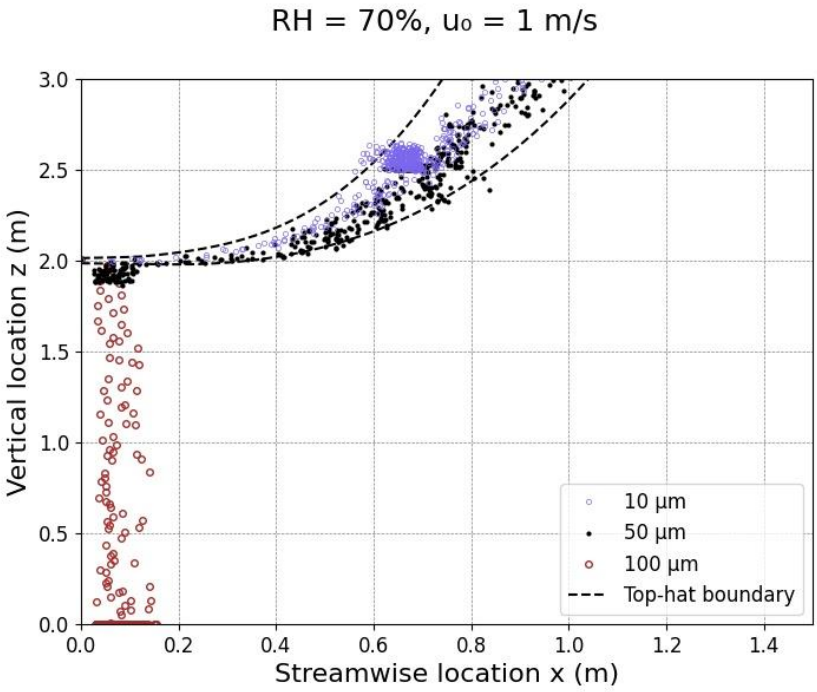

Figure 38: Instantaneous dispersion pattern of 500 droplets (t = 60 s) in the turbulent buoyant jet (d_0 = 2 cm, u_0 = 1 m/s, T_{amb} = 20 °C, RH = 70%).

For a speaking jet (u_0 = 4 m/s) the results are similar to the breathing jet in terms of the effect of the relative humidity.

The large droplets have the same pattern and fall out of the jet quickly. Because of the larger initial momentum they reach between 0.2 – 0.6 m streamwise distance. We see that the 50 µm droplets are clustered together between 0.9 – 1.7 m streamwise distance from the orifice in the lower part of the jet. The reason is that initially the droplets are influenced by their own weight to stay on the lower side and after one meter the velocity of the jet has already decreased to 12% of the initial velocity.

For the same reason the small droplets are located in the upper side of the jet due to the limited influence of gravity from an early stage on. In general holds that there are less droplets in the dispersion pattern visible for higher relative humidity conditions as the droplets have either already settled on the ground, or moved out of the figure's boundary.

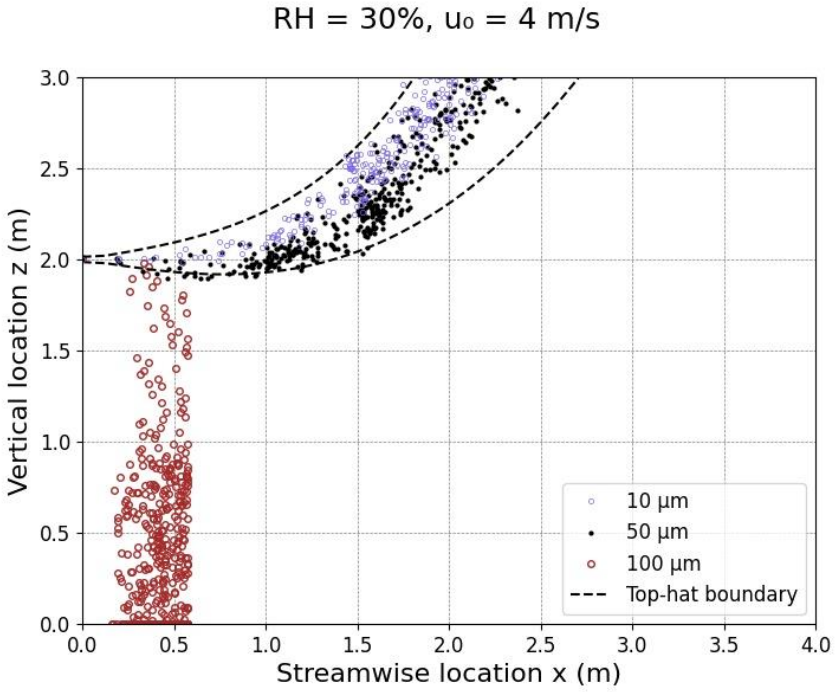

Figure 39: Instantaneous dispersion pattern of 500 droplets (t = 60 s) in the turbulent buoyant jet (d_0 = 2 cm, u_0 = 4 m/s, T_{amb} = 20 °C, RH = 30%).

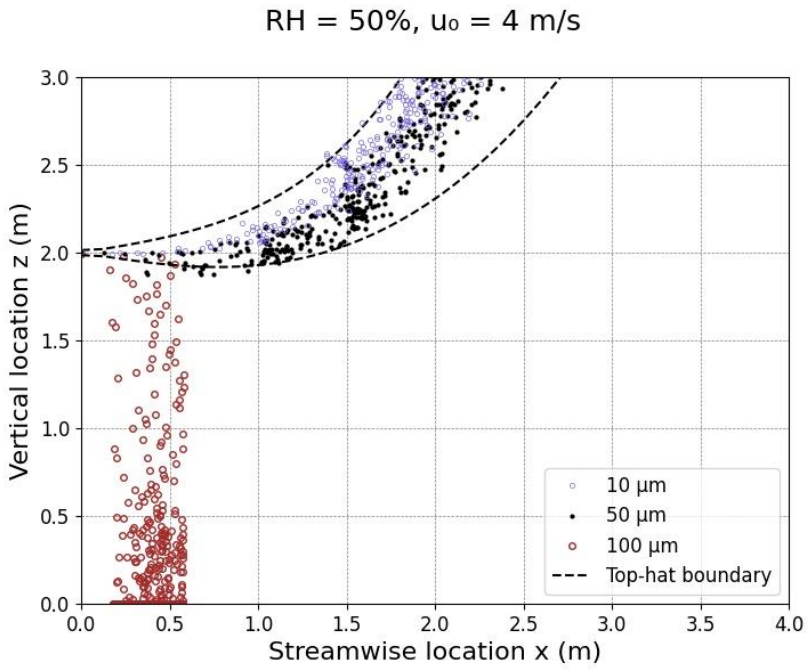

Figure 40: Instantaneous dispersion pattern of 500 droplets (t = 60 s) in the turbulent buoyant jet (d_0 = 2 cm, u_0 = 4 m/s, T_{amb} = 20 °C, RH = 50%).

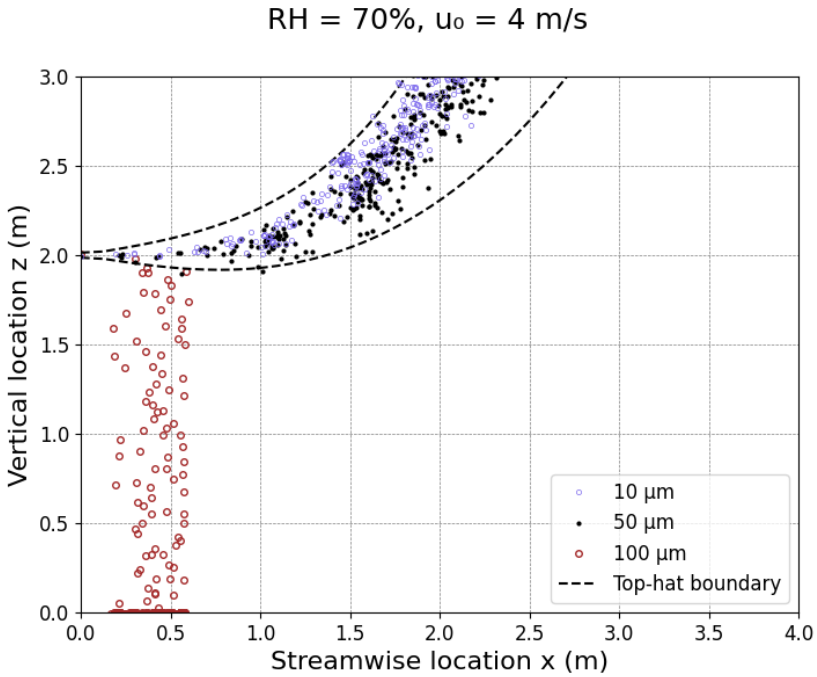

Figure 41: Instantaneous dispersion pattern of 500 droplets (t = 60 s) in the turbulent buoyant jet (d_0 = 2 cm, u_0 = 4 m/s, T_{amb} = 20 °C, RH = 70%).

For a cough jet (u_0 = 10 m/s) we see the same phenomena (Figure 42 - 44). In lower relative humidity, the droplets fall slower and the medium particles are relatively higher in the jet because they are lighter. For all three droplet sizes applies that because of the larger initial velocity, particles reach a larger streamwise distance. In the speaking jet, large droplets settle between a streamwise distance of 0.2 and 0.6 m. In the cough jet the same size droplets reach distances between 0.9 and 1.3 m, which corresponds to an average increase of 0.7 m. We see however in higher relative humidity conditions a larger spread both in streamwise direction as well in transverse direction (see B.2.3 Initial velocity u0 10 m/s). Here a combination of the turbulence and evaporation cause this increase.

The medium sized droplets remain in the jet meaning they have become airborne because of evaporation. Here we see as well that in higher relative humidity the droplets are located in the lower region of the jet.

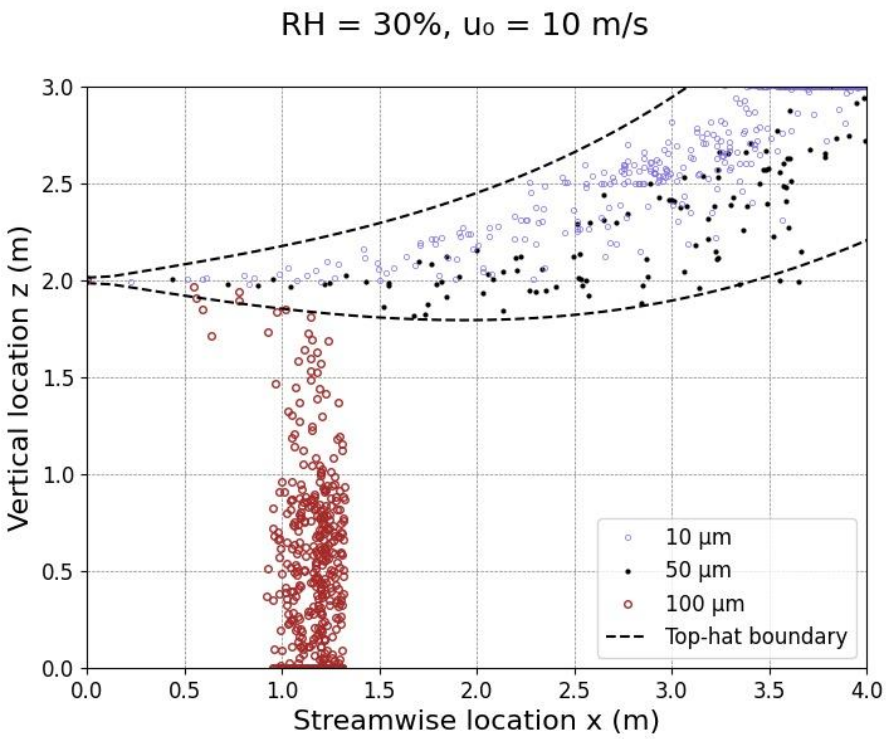

Figure 42: Instantaneous dispersion pattern of 500 droplets (t = 60 s) in the turbulent buoyant jet (d_0 = 2 cm, u_0 = 10 m/s, T_{amb} = 20 °C, RH = 30%).

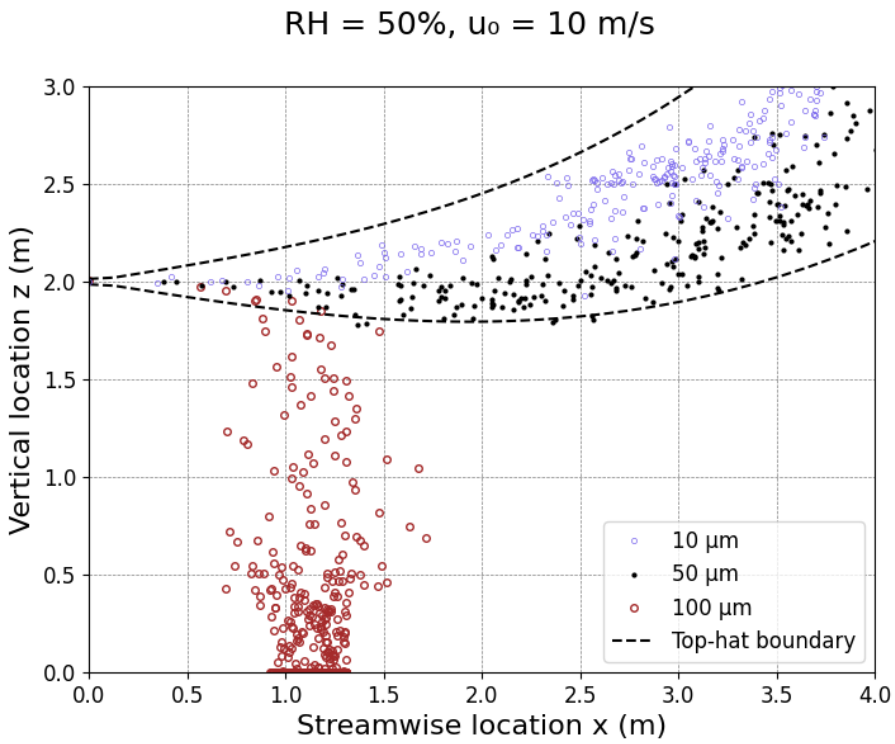

Figure 43: Instantaneous dispersion pattern of 500 droplets (t = 60 s) in the turbulent buoyant jet (d_0 = 2 cm, u_0 = 10 m/s, T_{amb} = 20 °C, RH = 50%).

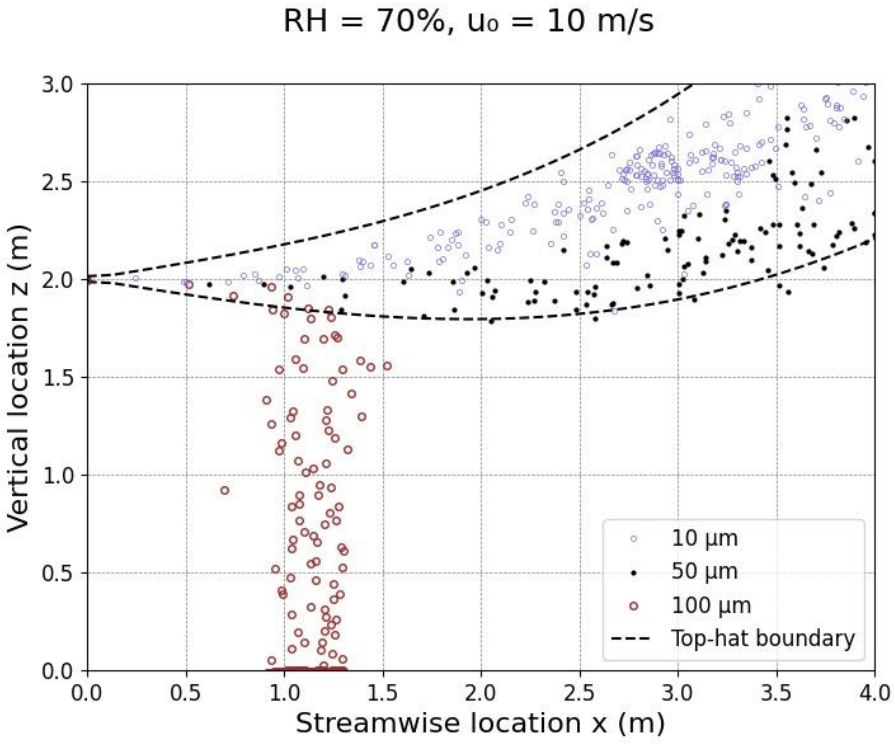

Figure 44: Instantaneous dispersion pattern of 500 droplets (t = 60 s) in the turbulent buoyant jet (d_0 = 2 cm, u_0 = 10 m/s, T_{amb} = 20 °C, RH = 70%).

Next the droplet distribution of W. Chen et al. (2020) was used to simulate a person speaking. The distribution measured letting participants count from 1 to 100 out loud and therefore a fair estimation of the measurement time is 100 seconds. They measured on average 250 respiratory droplets during counting and placed them in 16 different droplet size (diameter) categories ranging from 3 µm to 1500 µm. 1000 droplets have been sampled from this droplet distribution and their trajectories have been calculated by means of the speaking jet with a relative humidity of 50% and ambient temperature 20 °C.

To gain understanding in the behaviour of the different droplet sizes, the droplet positions are plotted in 5 different figures at time points: 0.5, 1, 10, 50 and 100 seconds.

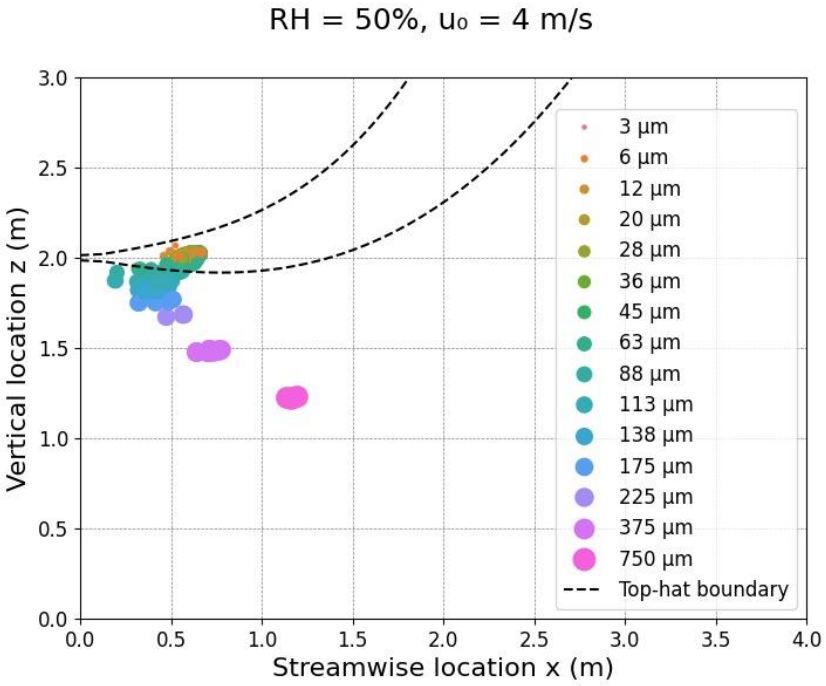

Figure 45: Dispersion pattern of 1000 droplets from a speaking distribution (t = 0.5 s).

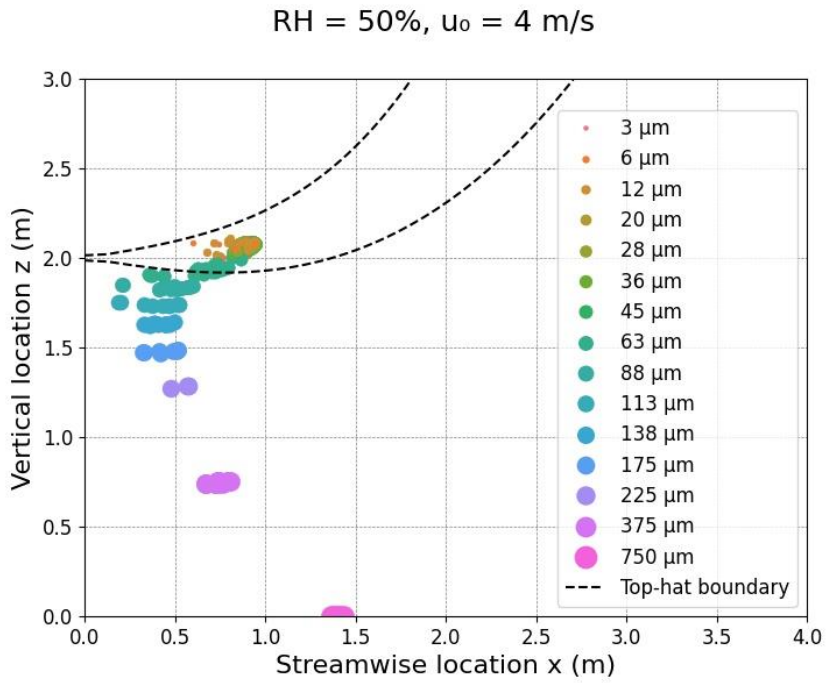

Figure 46: Dispersion pattern of 1000 droplets from a speaking distribution (t = 1 s).

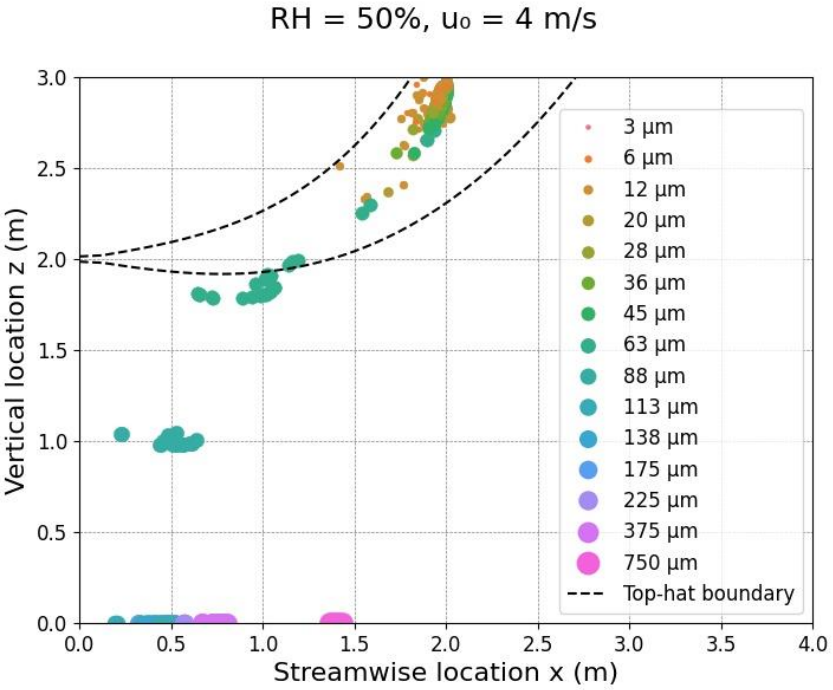

Figure 47: Dispersion pattern of 1000 droplets from a speaking distribution (t = 10 s).

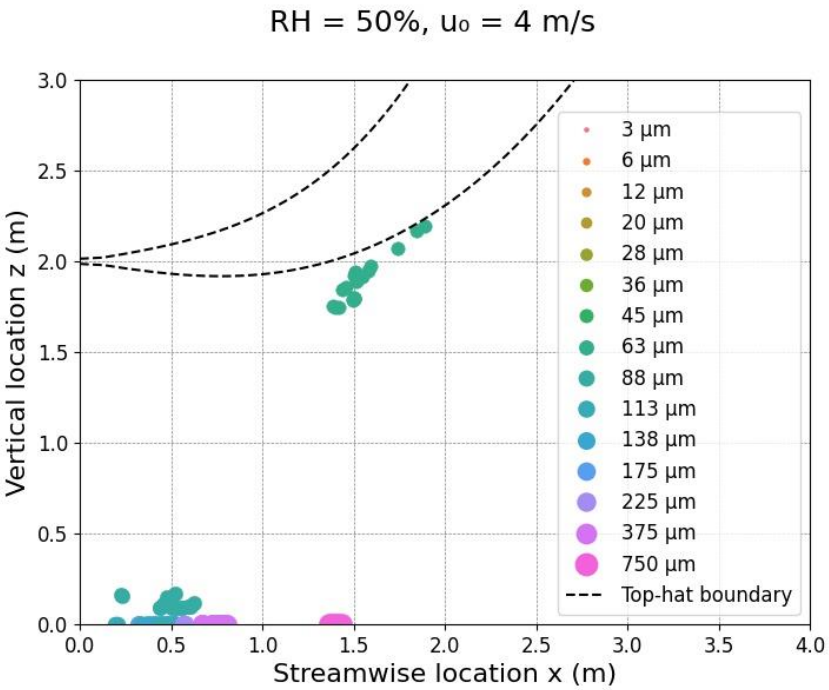

Figure 48: Dispersion pattern of 1000 droplets from a speaking distribution (t = 50 s).

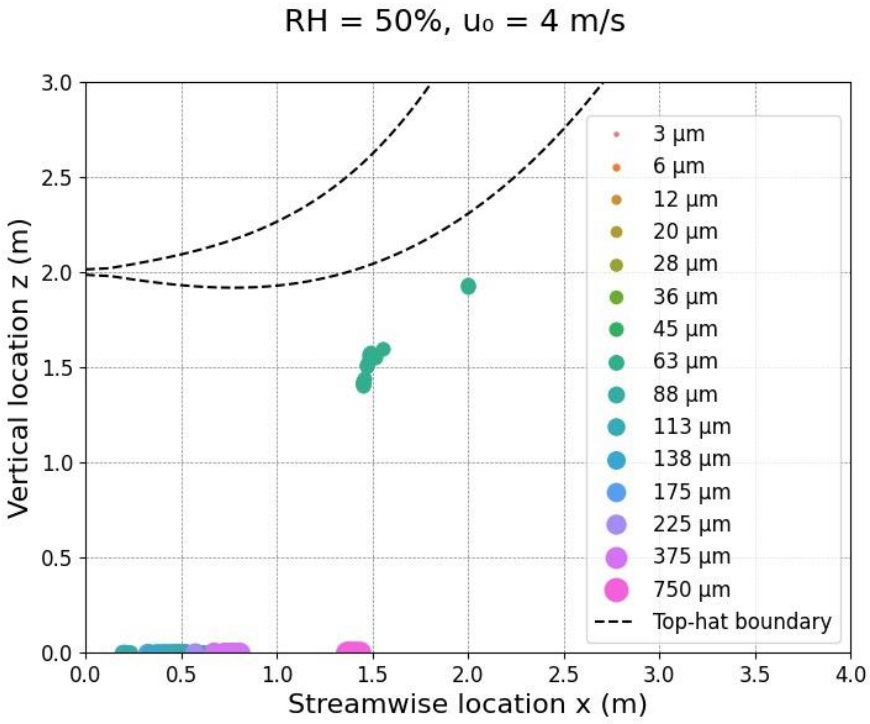

Figure 49: Dispersion pattern of 1000 droplets from a speaking distribution (t = 100 s).

From the first figure of this series several conclusions can be drawn immediately. After 0.5 seconds all droplets ≥ 88 µm have fallen out of the jet. Next to that we see that larger droplets reach a larger distance and also fall faster. All droplets < 63 µm are airborne and follow the direction of the jet. After 50 seconds almost all large size droplets have settled on the ground and reached between 0.2 and 0.8 m. This is in agreement with the results of W. Chen et al. (2020).

The droplets of 63 µm are at the boundary where some have become airborne following the jet and some have fallen out. Because of its size it would however take several minutes to settle on the ground.

Now that we have gained some knowledge and understanding about the behaviour of all these particles it is possible to calculate the concentration of respiratory droplets. Every 0.1 seconds a droplet is released given a total of 1000 droplets in a 100 second simulation. At any given timepoint, the droplets are divided into bins of size $x \cdot y \cdot z = 1 \cdot 0.5 \cdot 0.1$ m. The length in x-direction has been chosen to take into account the droplet spread in streamwise direction. A width of 0.5 m was chosen because > 95% of the droplets are within this range at a streamwise distance of 2.5 m. After adding the initial droplet size volumes, the total is divided by 4 to account for the larger sample size, and then divided by the volume of the bin to obtain the concentration of respiratory droplets in $\mu L/m^3$. The concentration levels at four randomly chosen timepoints (t = 1, 10, 50 and 80 s) are shown.

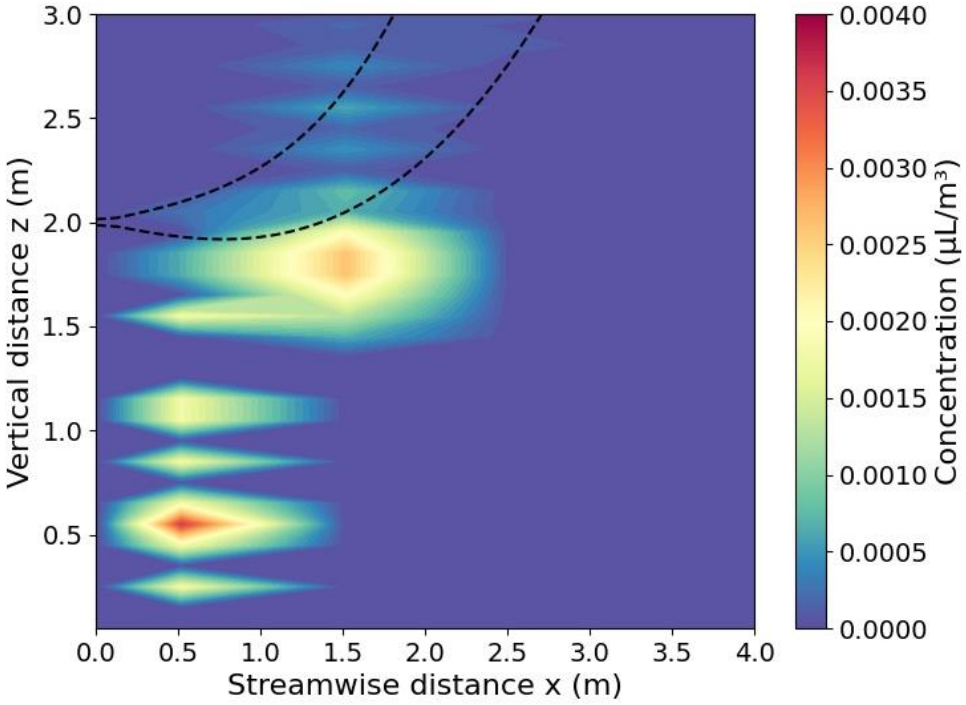

Figure 50: Concentration levels of respiratory droplets of a talking person (t = 1 s).

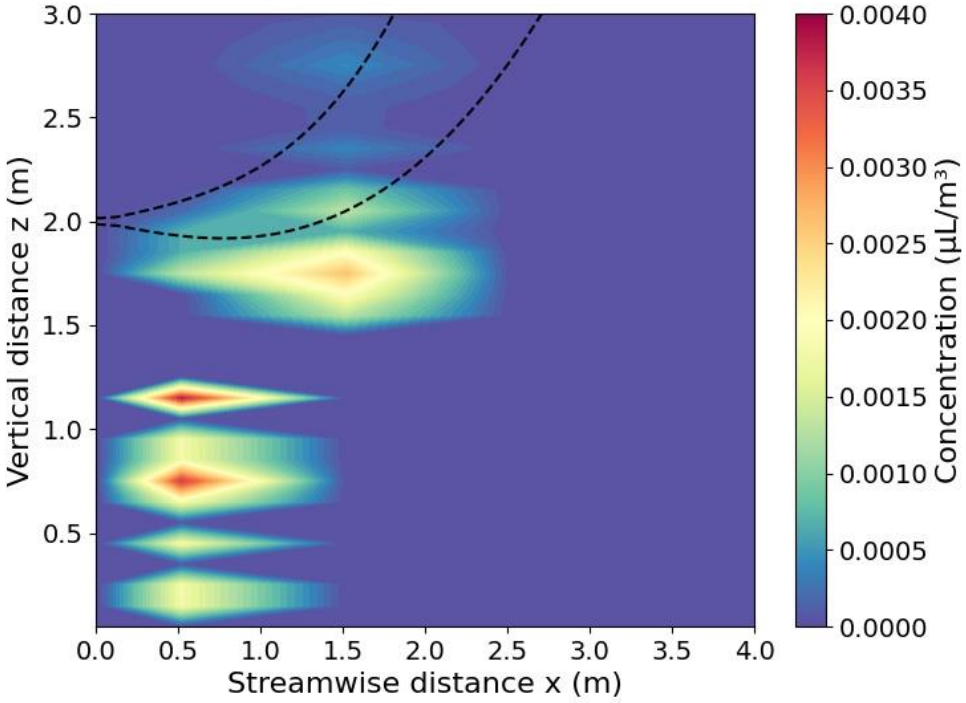

Figure 51: Concentration levels of respiratory droplets of a talking person (t = 10 s).

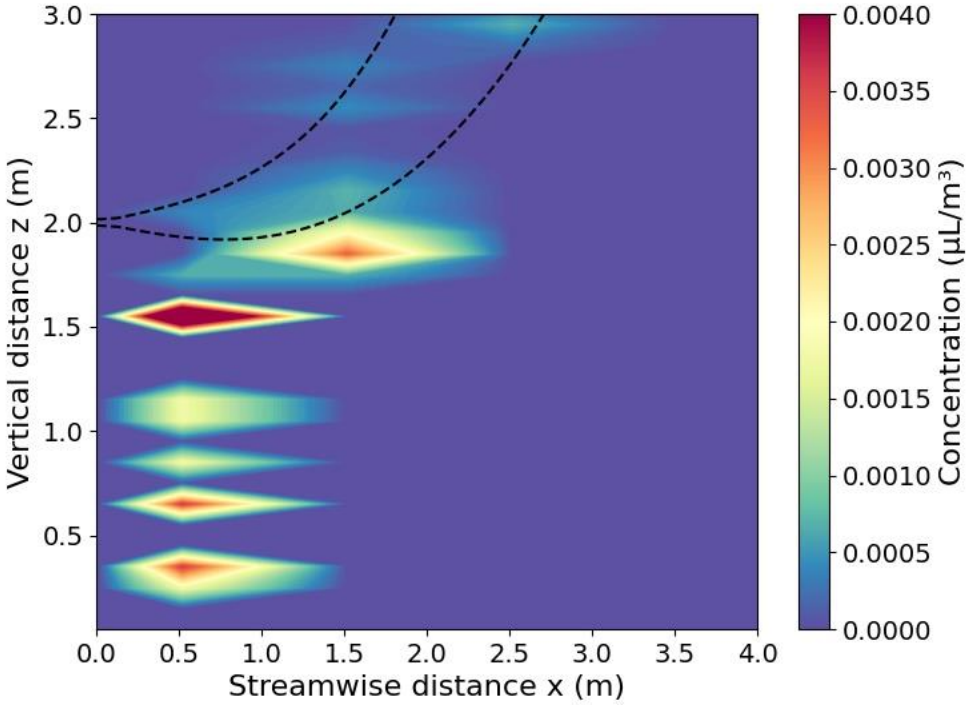

Figure 52: Concentration levels of respiratory droplets of a talking person (t = 50 s).

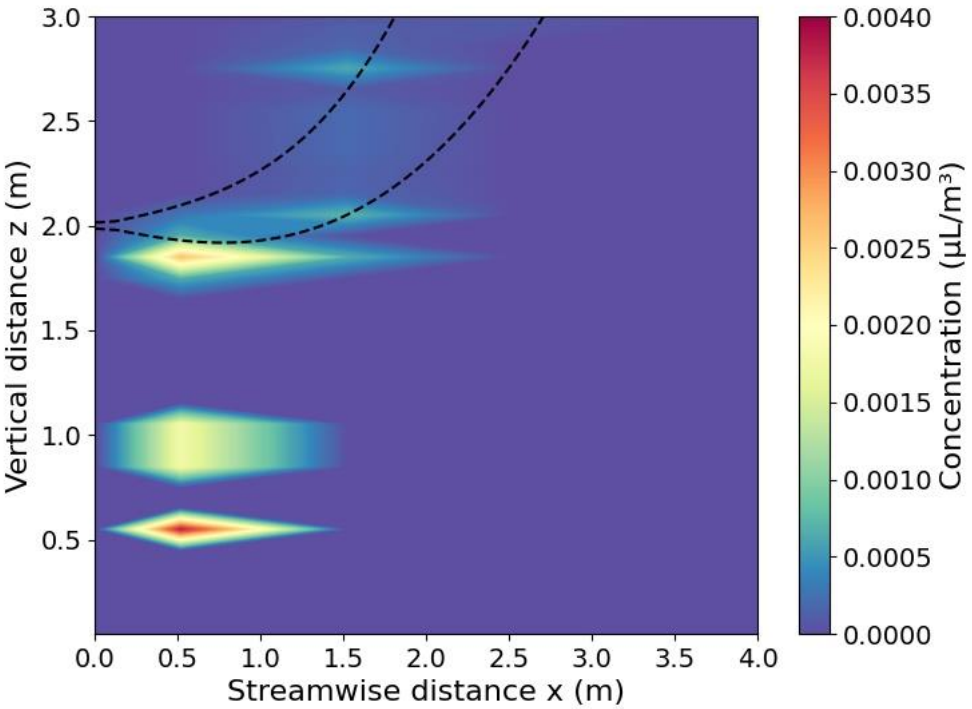

Figure 53: Concentration levels of respiratory droplets of a talking person (t = 80 s).

4.3 Model 3

The trajectory of the turbulent jet is estimated using the logistics function. It is easily seen that when x = z_M, the logistic's function has a value of 0.5 and both parts of the formula contribute for the same amount to the trajectory. Furthermore the value of k should be chosen in a way that when x has a value close to zero, Eq. (75) is dominant. For example when the initial velocity u_0 = 10 m/s, ambient crossflow U_a = 0.1 m/s and d_0 = 0.02 m we have:

$$M = \frac{1}{4}\pi d_0^2 u_0^2 = \frac{1}{4}\pi 0.02^2 10^2 = 0.00314\, m^4/s^2$$

$$z_M = M^{1/2}/U_a = 0.00314^{1/2}/0.1 = 0.56m$$

In the same way z_M has been calculated for u_0 = 4 m/s and U_a = 0.2 m/s (Table 11).

Table 11: Calculated values of z_M for several initial values.

u_0\U_a	0.1 m/s	0.2 m/s
10 m/s	0.56 m	0.28 m
4 m/s	0.35 m	0.18 m

In Figure 54 the logistic function corresponding to the quadratic solution has been plotted for z_M = 0.56 m and several values of k. in this case a value of k = 20 looks appropriate.

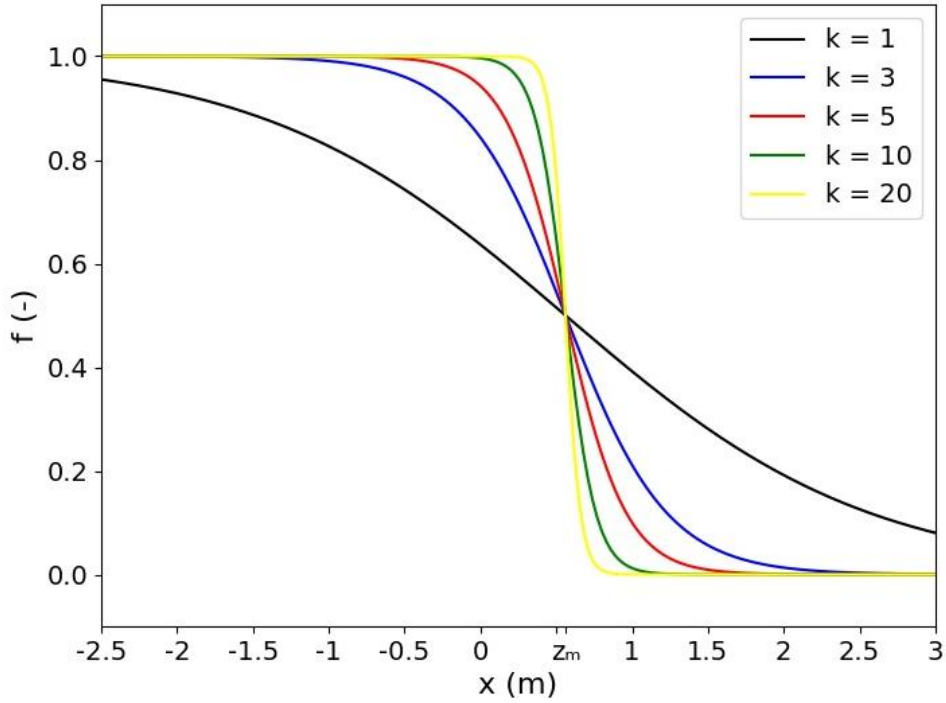

Figure 54: Sigmoid curve for z_m = 0.56 m and several values of k.

For smaller values of z_M a different value for k might fit better. To demonstrate the difference the Sigmoid curve for z_M = 0.28 m has been plotted in Figure 55. We see that at x = 0 the curve is barely equal to 1. We can conclude that when z_M gets smaller, the value of k should be larger. On the other hand the difference in trajectory is so small that one could argue that you could leave out the quadratic part of the equation and use only Eq. (76) to determine the trajectory of the jet in ambient flow. The trajectories of the four different conditions in Table 11 have been plotted in Figure 56. We see that the trajectories where U_a = 0.2 m/s have the steepest curve even compared to a relative low initial jet velocity (4 m/s) in a weaker ambient flow (U_a = 0.1 m/s).

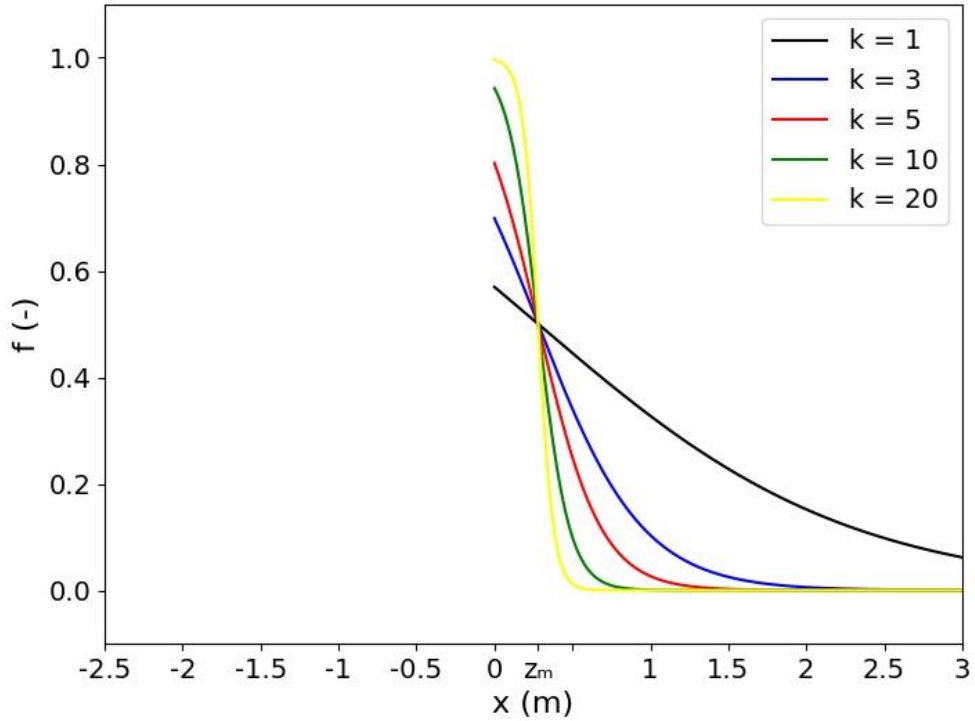

Figure 55: Sigmoid curve for z_M = 0.28 m and several values of k.

The properties along the centreline of the bent jet are still well defined. However the analytical model used in model 2 does not take into account the new boundary conditions. The Gaussian half width (β_g) and the jet entrainment velocities (α) are not defined in this problem. Therefore the influence on the velocity profiles, temperature profiles and turbulent velocity fluctuations and dissipations rates are not clear. Fischer et al. (1979) provided some Eulerian solutions to determine the dilution of a jet in an ambient crossflow. These solutions won't be used in this research because the Langrangian approach was used.

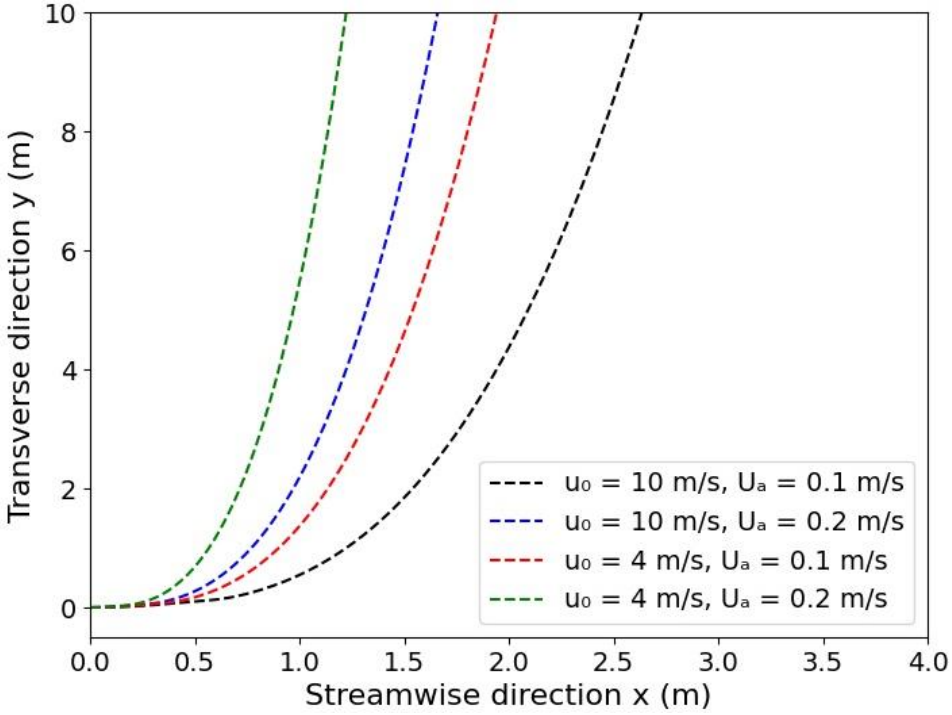

Figure 56: Trajectories of a jet in an ambient crossflow for several values of u_0 and U. (d_0 = 0.02 m, C1 = 2.0, C2 = 1.8, k = 20).

5 Discussion & Conclusion

In this chapter the main findings of the study are presented and recommendations are given to improve the presented models and expand the research. The thesis is concluded by giving practical implications.

5.1 Answers to the research questions

First the research questions are answered based on the results of the literature study and the results of the simulations.

5.1.1 What is the range of particle sizes relevant for the direct and airborne transmission?

Respiratory particles come in a wide variety of sizes. The majority of the sources indicate that exhaled droplets have diameters between 3 and 750 µm. In this research we have mainly focused on droplets of three different sizes: 10, 50 and 100 µm.

5.1.2 What is the distribution of respiratory particles for different human breathing modes?

The distribution of particles for speaking and coughing are similar. The mean value of the distribution in both modes is approximately 12 µm (Figure 5).

5.1.3 What is the influence of evaporation on the travel distance and lifetime of exhaled particles?

Evaporation of the droplets which humans exhale happens in a short period of time and therefore has a strong effect on the dispersion of droplets. In particular on the medium size droplets of 50 µm. These droplets evaporate to approximately 16 µm, which takes approximately 1 second in 0% RH and 10 seconds in 90% RH. Then these droplets behave similar to the 10 µm droplets, namely airborne. The jet airflow becomes dominant and gravity has a strongly reduced impact on the trajectories. Therefore these droplets travel further than if they had fallen out of the respiratory jet. This is particularly visible comparing the results of the non-buoyant jet without evaporation and the buoyant jet including evaporation. In general holds that droplets settle faster when they are larger. The travel distance and lifetime of droplets increase because of evaporation.

In cases of higher relative humidity, evaporation of droplets happens slower. In this case the larger particles fall out of the jet and settle on the ground. The relative velocity between a droplet and the surrounding air also contribute to the evaporation process. Altogether evaporation and the relative humidity of indoor space are important factors contributing to the dispersion of respiratory particles.

5.1.4 How does a turbulent jet interact with a crossflow?

Ambient crossflows bend the jet trajectory into the direction of the ambient crossflow. The curvature depends on the ratio of initial momentum flux of the jet and the ambient crossflow, named the length scale. No mean velocity and turbulence properties of such bent jets have been found in this study. Solutions for an Eulerian approach have been found to calculate dilution in such flows. Based on the results of turbulent jets in quiescence environments the small particles are likely to follow to trajectory of the bent jet. The larger particles are expected to fall out of the jet and settle on the ground. Whether the curved trajectory influences the settling distance of large respiratory particles remains a topic of research.

5.1.5 What is the influence of ventilation air flows on the travel distance and lifetime of exhaled particles?

This study has shown that droplets ≤ 68 µm are airborne or become airborne after evaporation. This is in accordance with the results of Chen et al. (2020). The characteristic length scales indicate when an ambient flow becomes dominant over the initial momentum- or buoyancy flux of a jet. When an

ambient flow becomes dominant the airborne particles will follow start following its direction. Also larger droplets are effected, although the effect is significantly less.

5.2 Discussion

The velocity and temperature profiles of jets are well researched and described in many sources. The semi-empirical RMS turbulent velocity fluctuation and turbulent dissipation rate are derived from a CFD model for determining sediment settling in water. The results are normalized with the mean jet properties: the centreline velocity and the Gaussian half width. The experiment which included this CFD model has been conducted for jets with a diameter of 6 mm and different initial velocities, sediment concentrations and sediment settling velocities. At a distance of $20d_0$, the turbulence velocity fluctuation and the dissipation rate are higher than the equations predict. The inclusion of this effect however, has been tested and found to be insignificant.

The results of this CFD model been adopted to calculate the trajectories of particles in a turbulent jet. A turbulent jet causes a larger spread compared to its non-turbulent counterpart. The breathing zone was found to be turbulent. In this study a DRW model has been used to determine the effect of turbulence. This model was chosen due to its relative simplicity and low amount of computational power needed.

The trajectory of the exhalation jet is influenced by both the initial velocity and the temperature difference between the jet and the ambient air. Higher temperature differences cause steeper trajectory curves as the effect of the buoyancy increases. Lower initial velocities decrease the momentum flux and therefore buoyancy becomes dominant in the jet.

The analysis of the concentration levels of respiratory droplets from a speaking person showed that the largest concentration levels are found along the trajectories of the large particles. This does not directly imply that the area where such droplets fall out of the jet lead to highest exposure of others. Interestingly, the largest droplets of 750 µm reach significantly further than the 100 µm droplets. In accordance with Chen et al. (2020) it is safe to assume that such droplets reach further than 2 meters when a person coughs or sneezes.

The dispersion patterns are comparable to the study of Wei & Li (2015). The largest discrepancy is found in the spread of the large respiratory droplets of 100 µm. The turbulence does not seem to have the same influence in both models. The initial momentum of the large particles is the largest factor contributing to its trajectory.

This study showed similar results as other studies in this field however some small differences were noted. The origin of the discrepancies are unknown. There are several potential reasons for these differences. The mean properties of the jet have been calculated over a predetermined grid. In a denser grid, these properties are calculated with higher accuracy. The calculated properties have then been interpolated on a rectangular grid, also with a predetermined grid size. The grid size was chosen densely around the jet orifice and less dense further downstream. Yet deviations might have occurred in this process. Also in this step a choice had to be made between accuracy and calculation speed.

5.3 Limitations of the study

The chemical composition of sputum has a significant effect on droplet evaporation. Sputum evaporates slower because of its saline and other component in comparison to pure water droplets. This effect has not been taken into account in this study.

Dispersion patterns have been compared with a fixed ambient temperature of 20 °C. However the indoor temperatures could fluctuate or set at a lower or higher temperature than in this study. The temperature in indoor space can also be stratified due to displacement ventilation with supply air from the floor. As temperature and the directly related water vapour density have a significant impact on the evaporation process, such stratification may have an effect on the dispersion of droplets.

All differential equations, both in the particle tracking model and evaporation model, have been solved implicitly or semi-implicitly. There are other mathematical methods to solve such equations more precisely. Up to which extent the programming language Python, in which the model has been written, can provide these, has not been investigated in this study.

The turbulence model uses stochastic principles. To obtain results with a stronger statistical significance, all simulations would have to be executed with an increased amount of particles.

All simulations had a person breathing perfectly horizontal as a starting point and keeping their head still for the full simulation time. In reality this is not the case. A person can also exhale through their nose and also rotate their head while speaking, beathing or coughing.

5.4 Practical implications

We have seen that the smallest airborne droplets and the largest droplets reach the furthest distances. Movement of large droplets could still be effectively stopped by for example masks or glass panes. In indoor environments personal ventilation strategies could be an effective way to guide the airborne particles to filters or other locations where others won't inhale or have droplets deposited on their mouth, nose or eyes.

Considering that one would implement such measures against airborne droplets, a lower relative humidity in the room would be desirable. In that way a smaller amount of droplets will settle on surfaces which others might touch and a larger amount will join the other airborne droplets to a designated location. This holds in the condition that the personal ventilation would capture the exhaled airborne particles before they are dispersed into the room air. For rooms with traditional ventilation, a higher relative humidity would be preferred as a larger amount of droplets will settle on the ground and won't become airborne.

Because of the buoyant nature of the exhalation jet, persons which are taller than other persons in their proximity are potentially at higher risk because of airborne particles. On the other hand smaller persons are more likely to be in the trajectory of larger respiratory particles of taller people around them.

5.5 Outlook

It seems safe to say that the semi-empirical equations regarding the turbulence velocity fluctuation and the dissipation rate are well established for buoyant turbulent jets. However for a more trustworthy model, it is advised to create a CFD model with initial parameters of this research. These parameters should include a larger jet diameter, comparable to a human mouth and air as the medium instead of water.

Another more advanced CFD model can provide great insight in the mean properties of jets in crossflows. Among these properties are mean velocities, temperatures, velocity fluctuations and dissipation rates. Also data from experiments would be highly usable to validate such CFD model results. An Eulerian approach could be used to validate the dispersion of small particles, considering this method is based on concentration levels rather than individual particle trajectories.

The turbulence properties from the CFD model could be used in a more accurate random walk model such as the continuous random walk or stochastic differential equation model. The computing power needed would be increased, however also here exist ways to decrease the calculation time. With handy use of parallel processing, a computer can use its multiple cores to execute the same process parallel. The particle tracking of each individual particle has no influence on the outcome of another particle. This makes parallel processing and ideal optimization for this model.

References

Bocksell, T. L., & Loth, E. (2001). *Random Walk Models for Particle Diffusion in Free-Shear Flows*. *39*(6). https://doi.org/10.2514/2.1421

Brohus, H., & Nielsen, P. V. (1996). Personal exposure in displacement ventilated rooms. *Indoor Air*, *6*(3), 157–167. https://doi.org/10.1111/j.1600-0668.1996.t01-1-00003.x

Chan, S. N., Lee, K. W. Y., & Lee, J. H. W. (2014). Numerical modelling of horizontal sediment-laden jets. *Environmental Fluid Mechanics*, *14*(1), 173–200. https://doi.org/10.1007/s10652-013-9287-2

Chao, C. Y. H., & Wan, M. P. (2006). A study of the dispersion of expiratory aerosols in unidirectional downward and ceiling-return type airflows using a multiphase approach. *Indoor Air*, *16*(4), 296–312. https://doi.org/10.1111/j.1600-0668.2006.00426.x

Chao, C. Y. H., Wan, M. P., Morawska, L., Johnson, G. R., Ristovski, Z. D., & Hargreaves, M. (2009). *Characterization of expiration air jets and droplet size distributions immediately at the mouth opening*. *40*, 122–133. https://doi.org/10.1016/j.jaerosci.2008.10.003

Chen, Q., & Xu, W. (1998). A zero-equation turbulence model for indoor airflow simulation. *Energy and Buildings*, *28*(2), 137–144. https://doi.org/10.1016/s0378-7788(98)00020-6

Chen, W., Zhang, N., Wei, J., Yen, H. L., & Li, Y. (2020). Short-range airborne route dominates exposure of respiratory infection during close contact. *Building and Environment*, *176*(January), 106859. https://doi.org/10.1016/j.buildenv.2020.106859

Cheng, C. H., Chow, C. L., & Chow, W. K. (2020). Trajectories of large respiratory droplets in indoor environment : A simplified approach. *Building and Environment*, *183*(August), 107196. https://doi.org/10.1016/j.buildenv.2020.107196

Chong, K. L., Ng, C. S., Hori, N., Yang, R., Verzicco, R., & Lohse, D. (2021). Extended Lifetime of Respiratory Droplets in a Turbulent Vapor Puff and Its Implications on Airborne Disease Transmission. *Physical Review Letters*, *126*(3), 34502. https://doi.org/10.1103/PhysRevLett.126.034502

Crapper, P. F. (1977). Forced plume characteristics. *Tellus*, *29*(5), 470–475. https://doi.org/10.3402/tellusa.v29i5.11380

Fischer, H. B., List, E. J., Koh, R. C. Y., Imberger, J., & Brooks, N. H. (1979). *Mixing in Inland and Coastal Waters*. Elsevier. https://doi.org/10.1016/C2009-0-22051-4

Floyd, K. A., Eberly, A. R., & Hadjifrangiskou, M. (2017). Adhesion of bacteria to surfaces and biofilm formation on medical devices. In *Biofilms and Implantable Medical Devices: Infection and Control*. Elsevier Ltd. https://doi.org/10.1016/B978-0-08-100382-4.00003-4

Fukushima, C., Aanen, L., & Westerweel, J. (2002). Investigation of the mixing process in an axisymmetric turbulent jet using PIV and LIF. *Laser Techniques for Fluid Mechanics*, 339–356. https://doi.org/10.1007/978-3-662-08263-8_20

George, W. K. (2013). Lectures in Turbulence for the 21st Century. *Department of Applied Mechanics Chalmers University of Technology Gothenburg, Sweden*, *January*, 303.

Gralton, J., Tovey, E., McLaws, M. L., & Rawlinson, W. D. (2011). The role of particle size in aerosolised pathogen transmission: A review. In *Journal of Infection* (Vol. 62, Issue 1, pp. 1–13). W.B. Saunders. https://doi.org/10.1016/j.jinf.2010.11.010

Gupta, J. K., Lin, C. H., & Chen, Q. (2010). Characterizing exhaled airflow from breathing and talking. *Indoor Air*, *20*(1), 31–39. https://doi.org/10.1111/j.1600-0668.2009.00623.x

Hartmann, A., Lange, J., Rotheudt, H., & Kriegel, M. (2020). Emission rate and particle size of bioaerosols during breathing , speaking and coughing. *Preprint*, 1–5.

Katopodes, N. D. (2019). Turbulent Flow. *Free-Surface Flow*, 566–650. https://doi.org/10.1016/B978-0-12-815489-2.00008-3

Knudsen, M. (1988). *Buoyant horizontal jets in an ambient flow*. *March*.

Lindsley, W. G., Reynolds, J. S., Szalajda, J. V., Noti, J. D., & Beezhold, D. H. (2013). A cough aerosol simulator for the study of disease transmission by human cough-generated aerosols. *Aerosol Science and Technology*, *47*(8), 937–944. https://doi.org/10.1080/02786826.2013.803019

List, E. J. (1982). Turbulent jets and plumes. *In: Annual Review of Fluid Mechanics*, *14*, *M. Va*, 189–212. https://doi.org/10.1016/b978-0-08-051177-1.50013-1

Liu, S., & Novoselac, A. (2014). Transport of airborne particles from an unobstructed cough jet. *Aerosol Science and Technology*, *48*(11), 1183–1194. https://doi.org/10.1080/02786826.2014.968655

Liu, X., & Zhai, Z. (2007). Identification of appropriate CFD models for simulating aerosol particle and droplet indoor transport. *Indoor and Built Environment*, *16*(4), 322–330. https://doi.org/10.1177/1420326X06079890

Monto, A. S. (2012). Epidemiology of Respiratory Infection. *Pathy's Principles and Practice of Geriatric Medicine: Fifth Edition*, *1*, 549–554. https://doi.org/10.1002/9781119952930.ch46

Nielsen, P. V., Jensen, R. L., Litewnicki, M., & Zajas, J. (2009). Experiments on the microenvironment and breathing of a person in isothermal and stratified surroundings. *9th International Conference and Exhibition - Healthy Buildings 2009, HB 2009*, 1–10.

Olmedo, I., Nielsen, P. V., Ruiz de Adana, M., Jensen, R. L., & Grzelecki, P. (2012). Distribution of exhaled contaminants and personal exposure in a room using three different air distribution strategies. *Indoor Air*, *22*(1), 64–76. https://doi.org/10.1111/j.1600-0668.2011.00736.x

Papineni, R. S., & Rosenthal, F. S. (1997). The size distribution of droplets in the exhaled breath of healthy human subjects. *Journal of Aerosol Medicine: Deposition, Clearance, and Effects in the Lung*, *10*(2), 105–116. https://doi.org/10.1089/jam.1997.10.105

Redrow, J., Mao, S., Celik, I., Posada, J. A., & Feng, Z. gang. (2011). Modeling the evaporation and dispersion of airborne sputum droplets expelled from a human cough. *Building and Environment*, *46*(10), 2042–2051. https://doi.org/10.1016/j.buildenv.2011.04.011

Saidi, M. S., Rismanian, M., Monjezi, M., Zendehbad, M., & Fatehiboroujeni, S. (2014). Comparison between Lagrangian and Eulerian approaches in predicting motion of micron-sized particles in laminar flows. *Atmospheric Environment*, *89*, 199–206. https://doi.org/10.1016/J.ATMOSENV.2014.01.069

Steinberger, R. L., & Treybal, R. E. (1960). Mass transfer from a solid soluble sphere to a flowing liquid stream. *AIChE*, *6*(2), 227–232. https://doi.org/https://doi.org/10.1002/aic.690060213

Team, R. (2020). *De druppel die de emmer deed overlopen ? Van insignificant naar ' smoking gun .'* 1–19.

Tellier, R., Li, Y., Cowling, B. J., & Tang, J. W. (2019). *Recognition of aerosol transmission of infectious agents : a commentary*. 1–10.

Wei, J., & Li, Y. (2015). Enhanced spread of expiratory droplets by turbulence in a cough jet. *Building and Environment*, *93*(P2), 86–96. https://doi.org/10.1016/j.buildenv.2015.06.018

Xie, X., Li, Y., Chwang, A. T. Y., Ho, P. L., & Seto, W. H. (2007). How far droplets can move in indoor environments - revisiting the Wells evaporation-falling curve. *Indoor Air*, *17*(3), 211–225. https://doi.org/10.1111/j.1600-0668.2007.00469.x

Xu, C. (2018). *Characterizing human breathing and its interactions with room ventilation*.

Yadav, H., Agrawal, A., & Srivastava, A. (2016). Mixing and entrainment characteristics of a pulse jet. *International Journal of Heat and Fluid Flow*, *61*, 749–761. https://doi.org/10.1016/J.IJHEATFLUIDFLOW.2016.08.006

Appendix A Buoyant jet results of Model 2

A.1 Velocity profile of Model 2

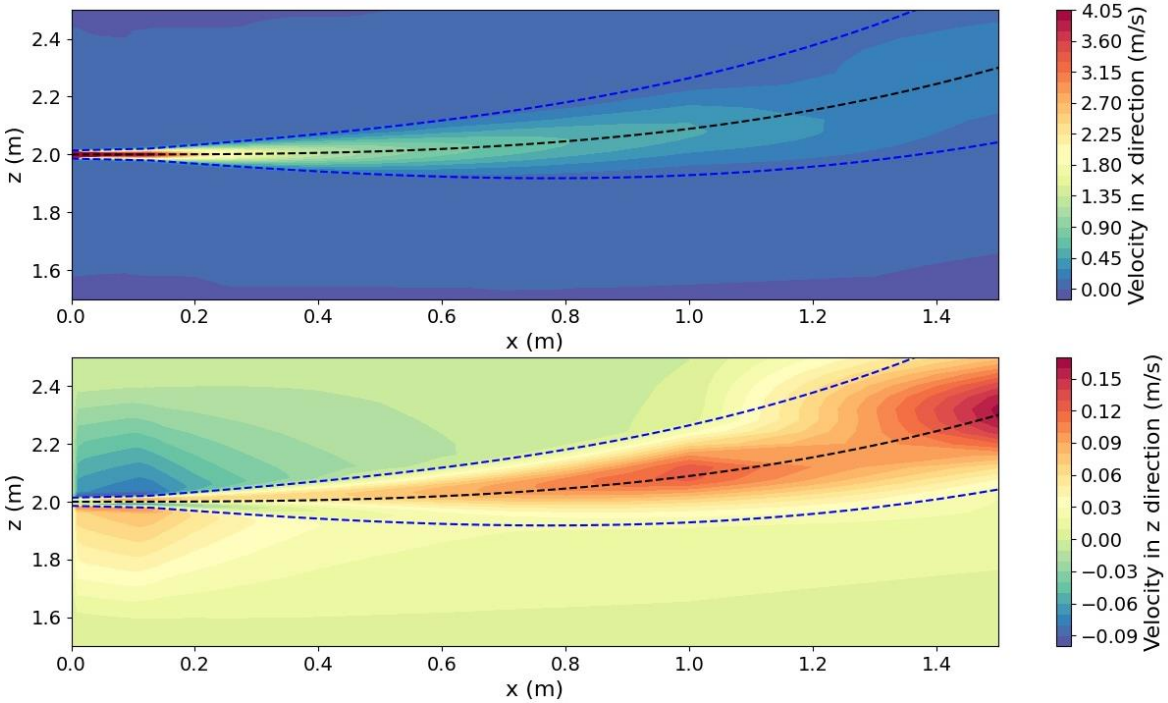

Figure 57: Velocity profiles in the plane y = 0. The figure shows a buoyant jet with u0 = 4 m/s, T_0 = 35℃ and T_a =20 ℃. The blue dashed lines represent the top-hat boundary of the jet.

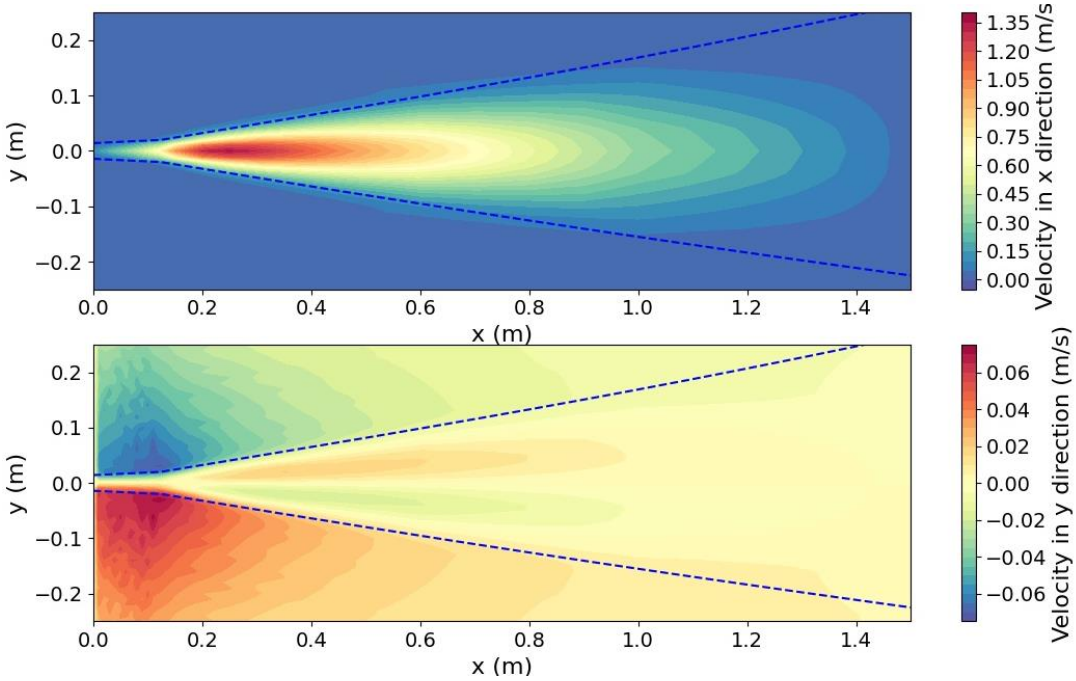

Figure 58: Velocity profiles in the plane z = 0. The figure shows a buoyant jet with u0 = 4 m/s, T0 = 35°C and Ta =20 °C. The blue dashed lines represent the top-hat boundary of the jet.

Appendix B Additional results of Model 2

B.1 Results of isothermal jet with an integration timestep of 0.01 s

The results show the simulation of 5000 droplets for each droplet size.

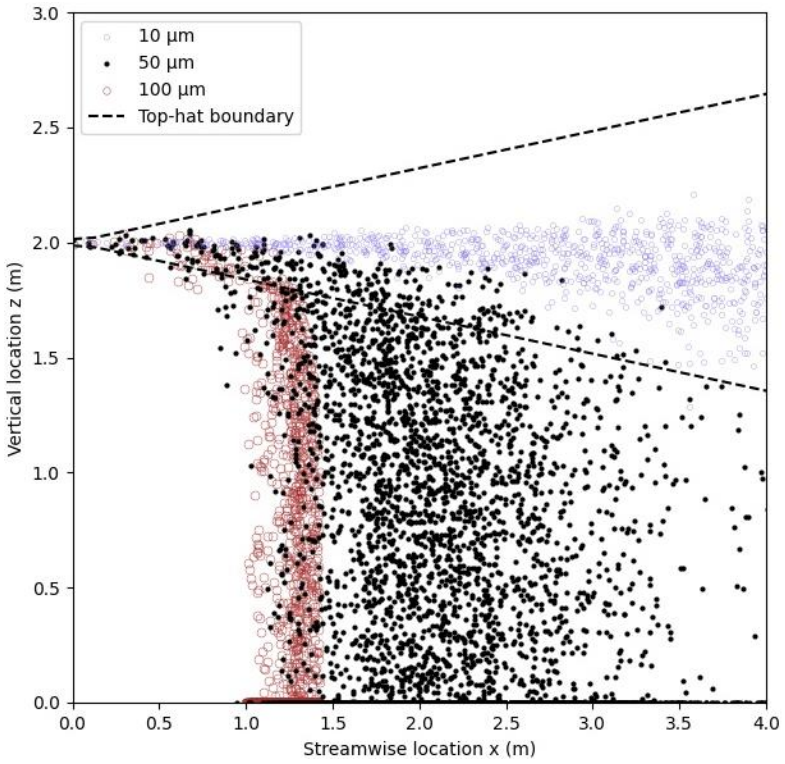

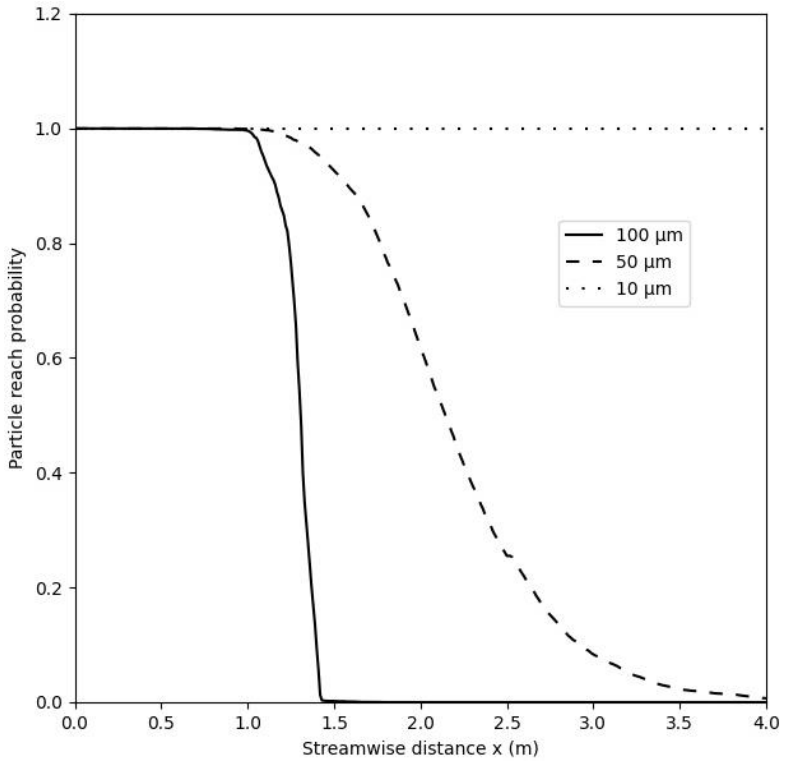

The spread at x = 4 m

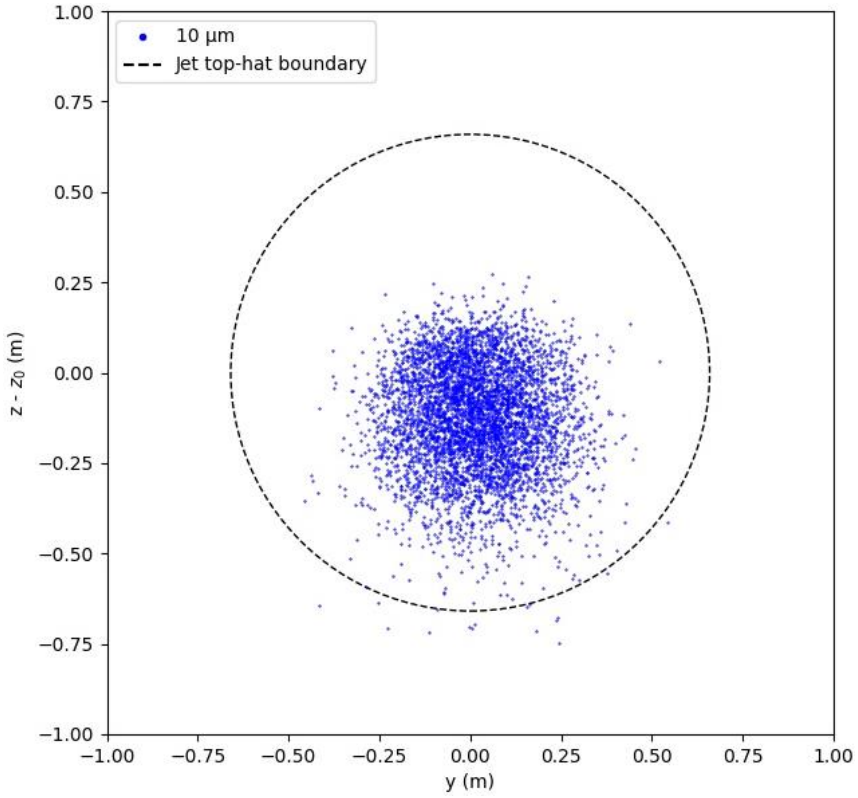

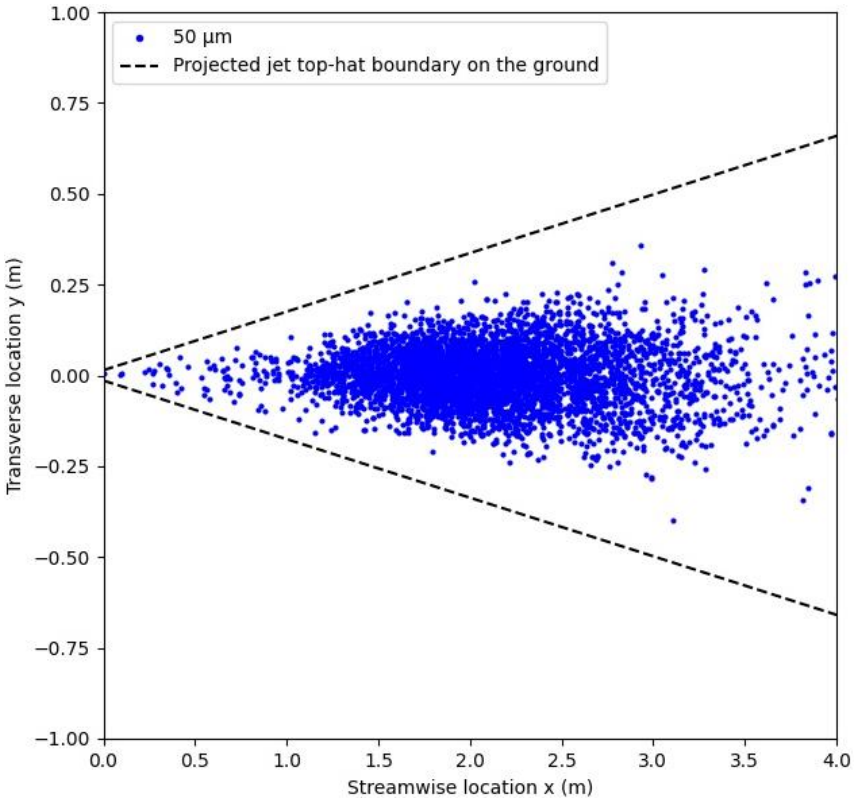

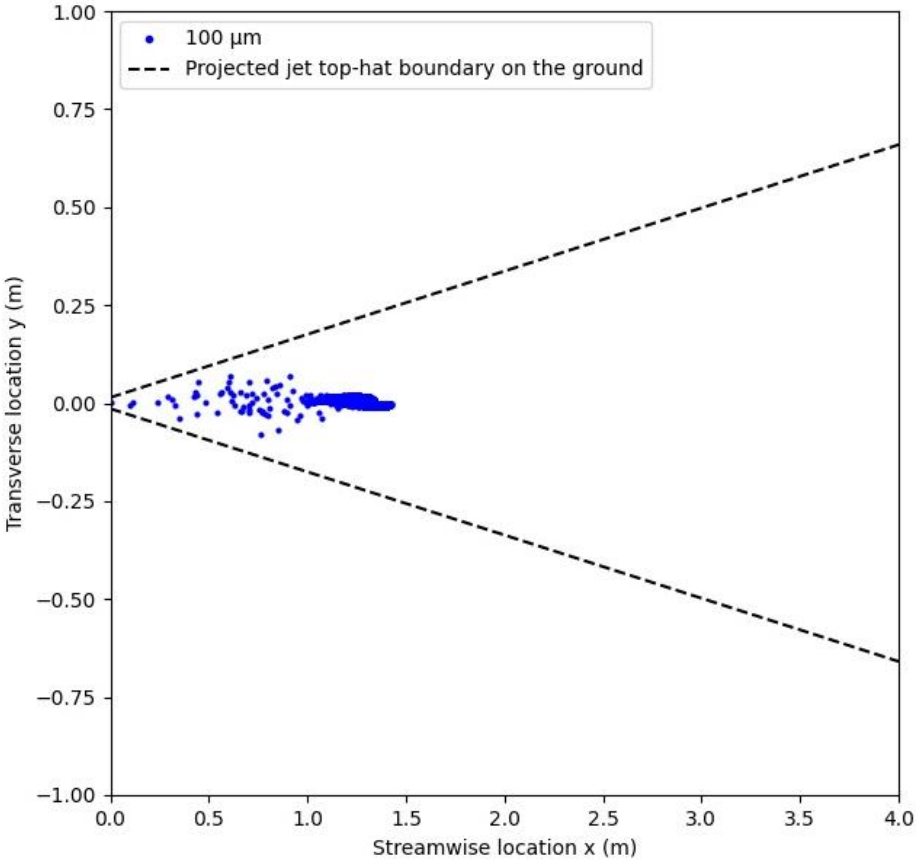
100 µm
Projected jet top-hat boundary on the ground
Transverse location y (m)
Streamwise location x (m)
1.00
0.75
0.50
0.25
0.00
−0.25
−0.50
−0.75
−1.00
0.0
0.5
1.0
1.5
2.0
2.5
3.0
3.5
4.0

B.2 Results of buoyant jet

B.2.1 Initial velocity u_0 1 m/s

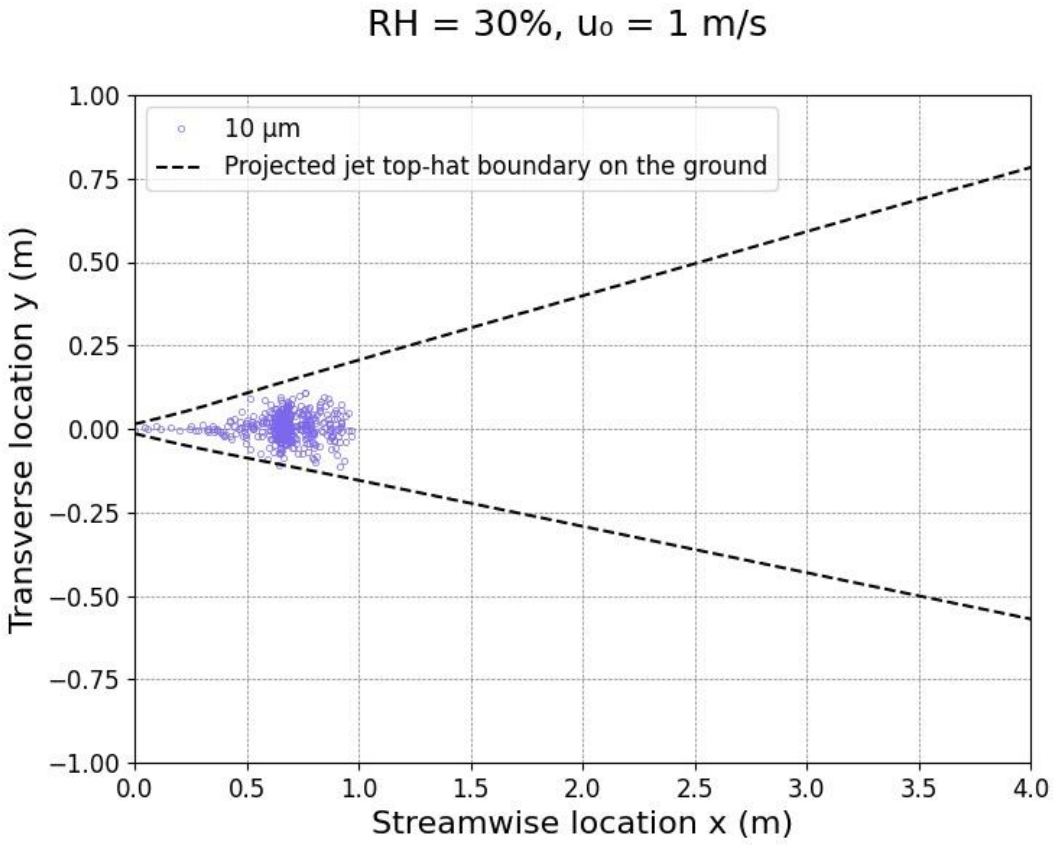

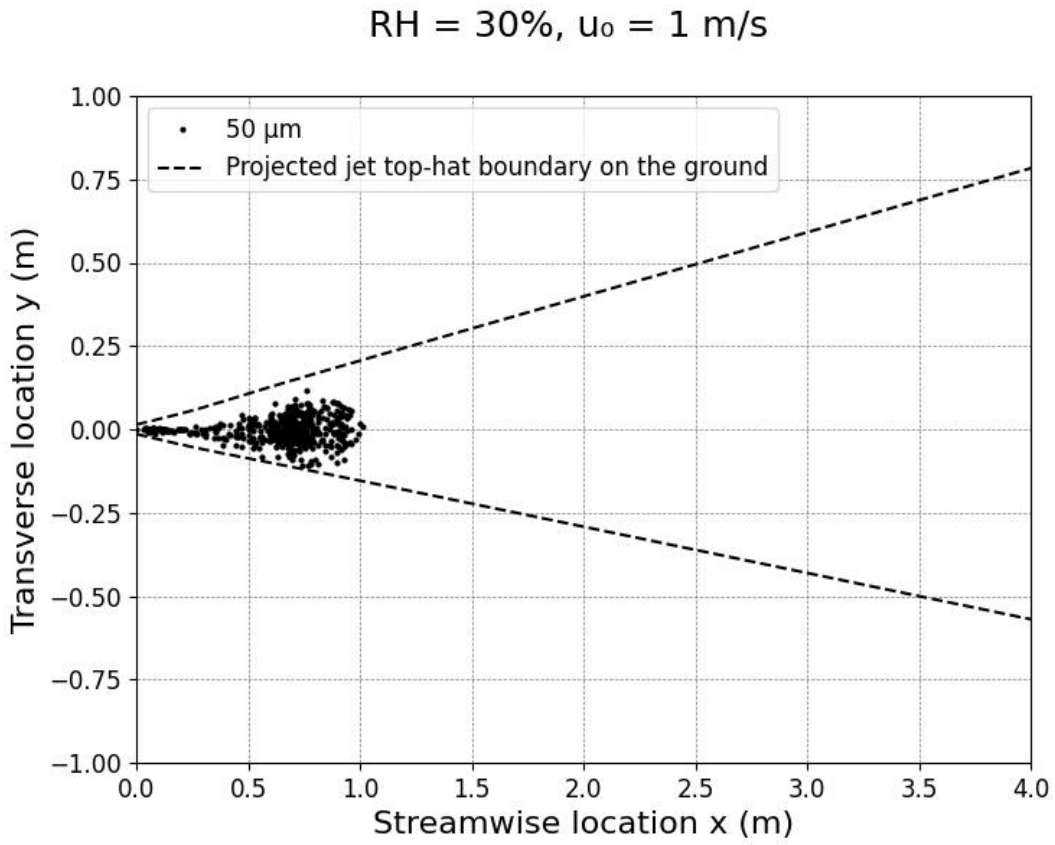

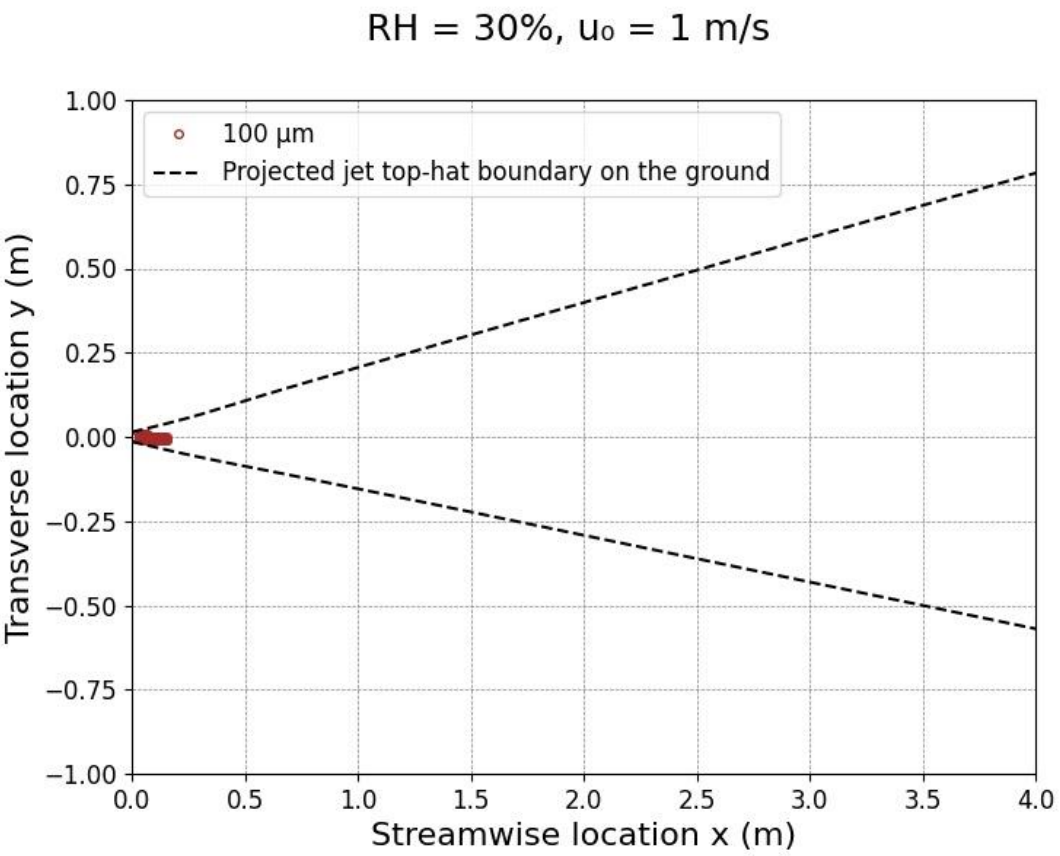
RH = 30%, u₀ = 1 m/s
100 µm
Projected jet top-hat boundary on the ground
Transverse location y (m)
Streamwise location x (m)
1.00
0.75
0.50
0.25
0.00
−0.25
−0.50
−0.75
−1.00
0.0
0.5
1.0
1.5
2.0
2.5
3.0
3.5
4.0

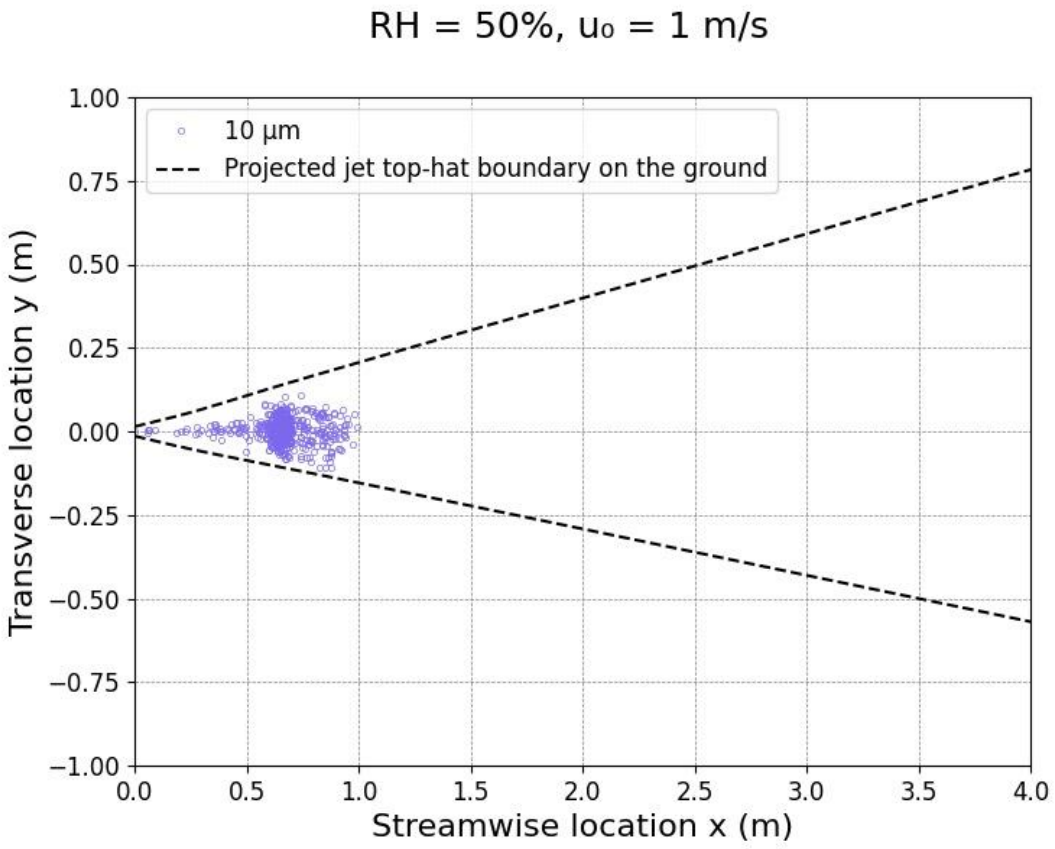
RH = 50%, u₀ = 1 m/s
10 µm
Projected jet top-hat boundary on the ground
Transverse location y (m)
Streamwise location x (m)
1.00
0.75
0.50
0.25
0.00
−0.25
−0.50
−0.75
−1.00
0.0
0.5
1.0
1.5
2.0
2.5
3.0
3.5
4.0

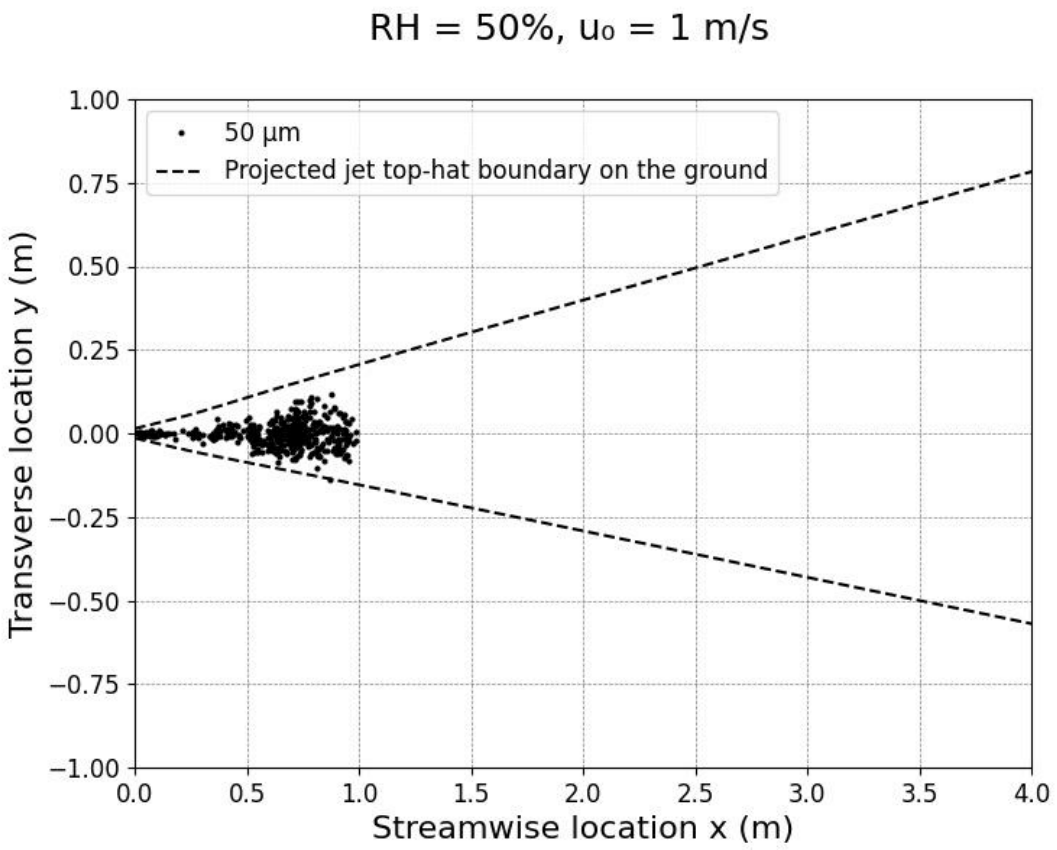
RH = 50%, u₀ = 1 m/s
50 µm
Projected jet top-hat boundary on the ground
Transverse location y (m)
Streamwise location x (m)
1.00
0.75
0.50
0.25
0.00
−0.25
−0.50
−0.75
−1.00
0.0
0.5
1.0
1.5
2.0
2.5
3.0
3.5
4.0

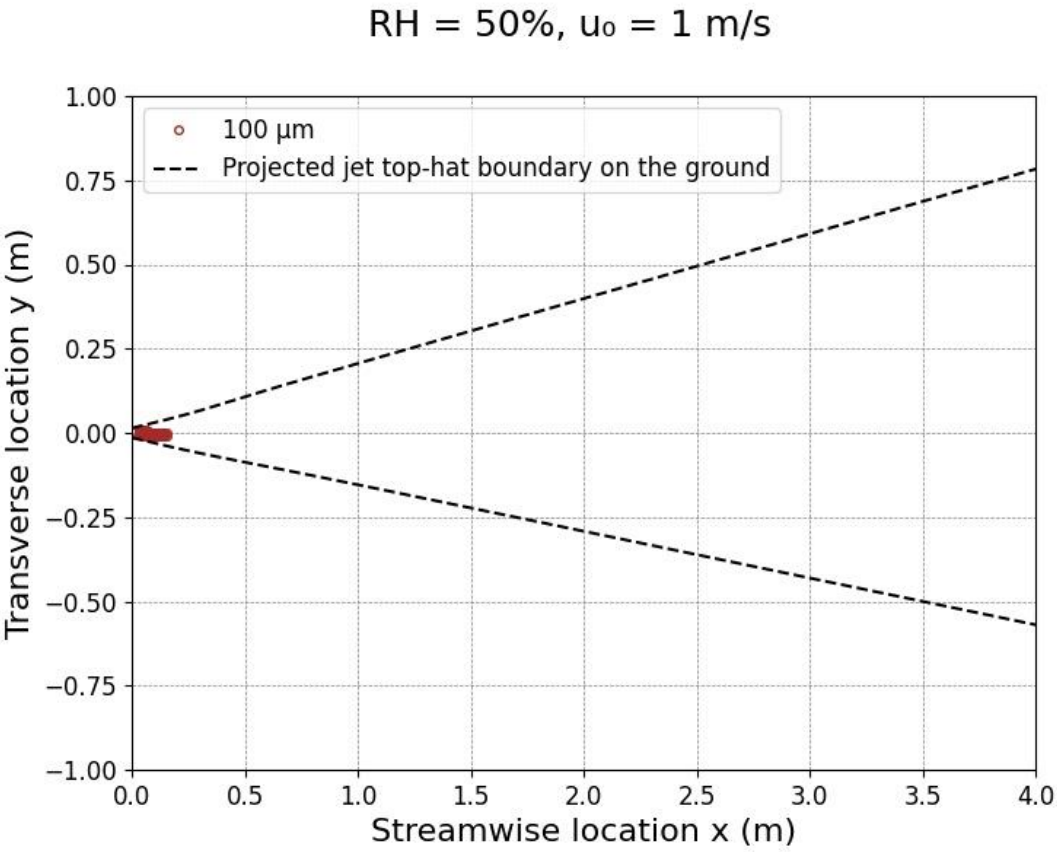
RH = 50%, u₀ = 1 m/s
100 µm
Projected jet top-hat boundary on the ground
Transverse location y (m)
Streamwise location x (m)
1.00
0.75
0.50
0.25
0.00
−0.25
−0.50
−0.75
−1.00
0.0
0.5
1.0
1.5
2.0
2.5
3.0
3.5
4.0

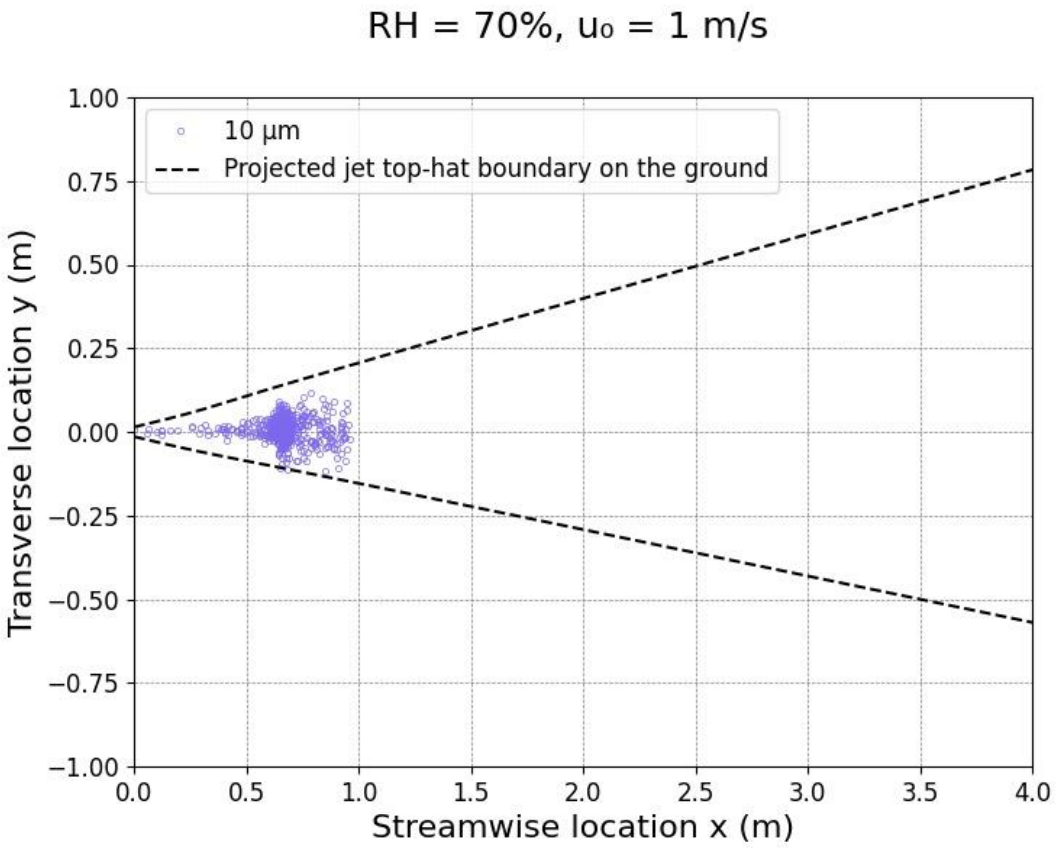
RH = 70%, u₀ = 1 m/s
10 µm
Projected jet top-hat boundary on the ground
Transverse location y (m)
Streamwise location x (m)
1.00
0.75
0.50
0.25
0.00
−0.25
−0.50
−0.75
−1.00
0.0
0.5
1.0
1.5
2.0
2.5
3.0
3.5
4.0

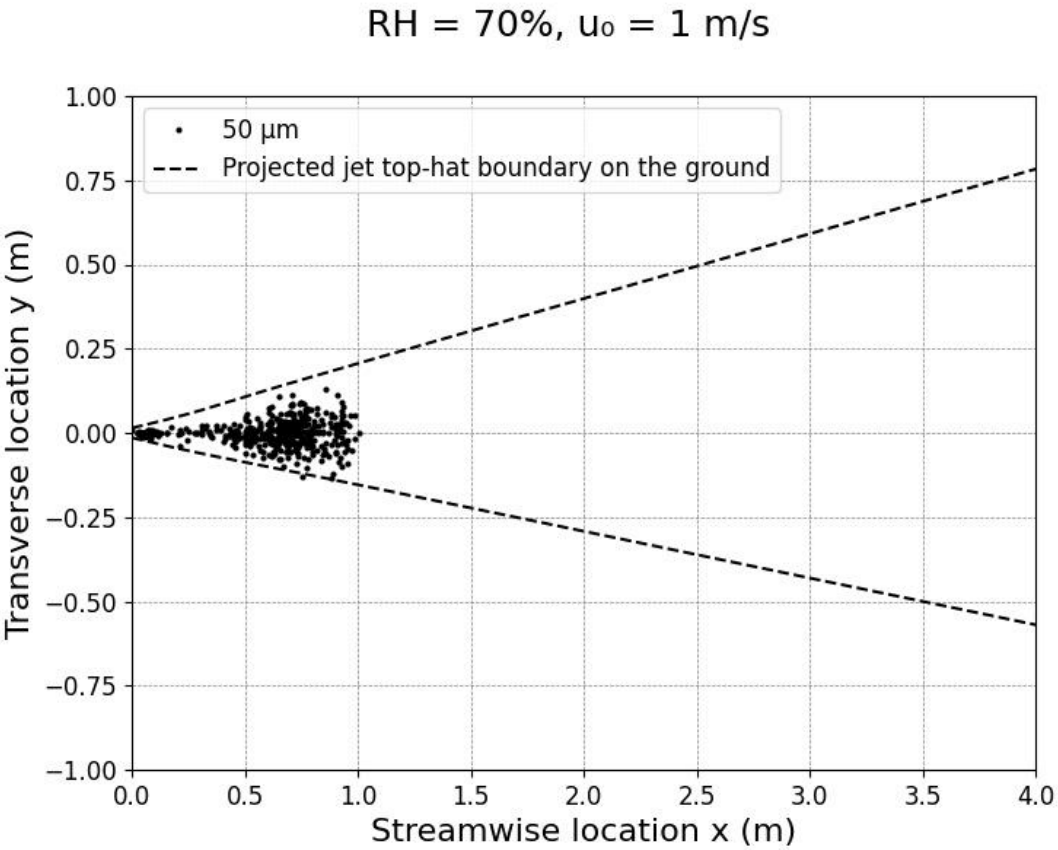
RH = 70%, u₀ = 1 m/s
50 µm
Projected jet top-hat boundary on the ground
Transverse location y (m)
Streamwise location x (m)
1.00
0.75
0.50
0.25
0.00
−0.25
−0.50
−0.75
−1.00
0.0
0.5
1.0
1.5
2.0
2.5
3.0
3.5
4.0

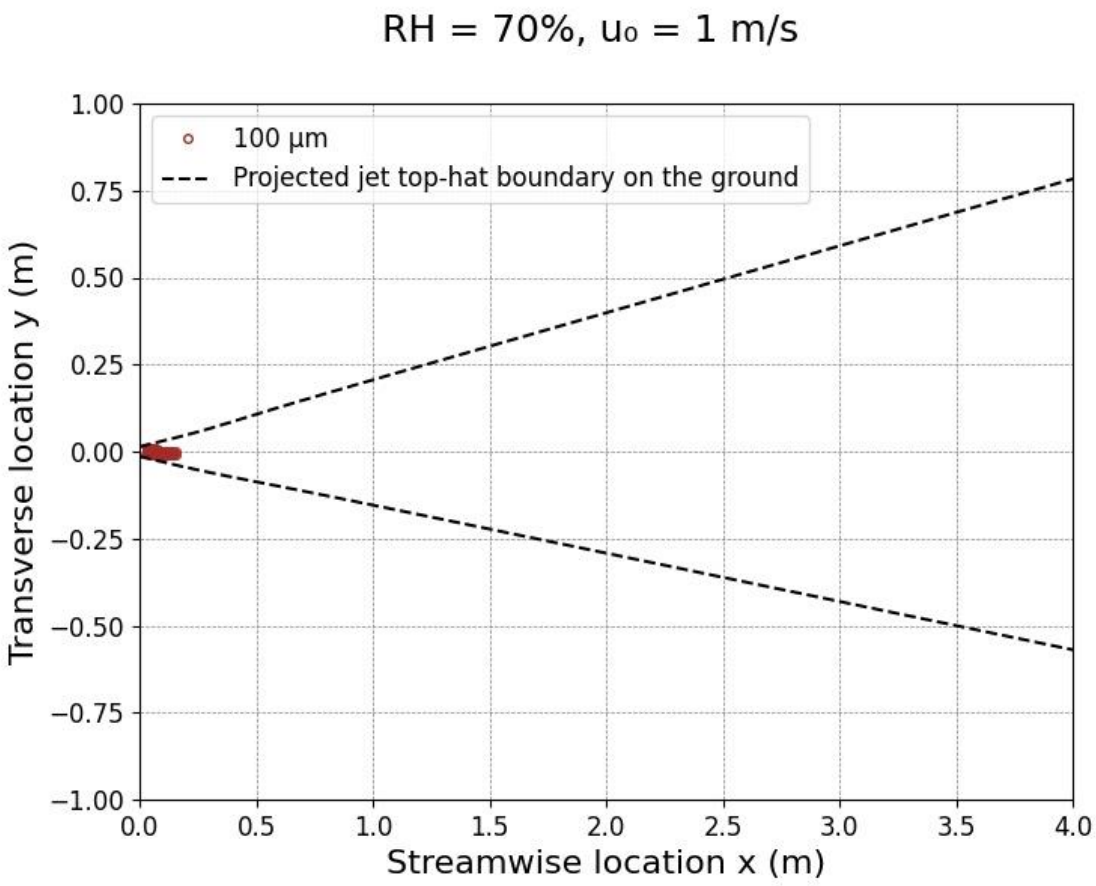
RH = 70%, u₀ = 1 m/s
100 µm
Projected jet top-hat boundary on the ground
Transverse location y (m)
Streamwise location x (m)
1.00
0.75
0.50
0.25
0.00
−0.25
−0.50
−0.75
−1.00
0.0
0.5
1.0
1.5
2.0
2.5
3.0
3.5
4.0

B.2.2 Initial velocity u_0 4 m/s

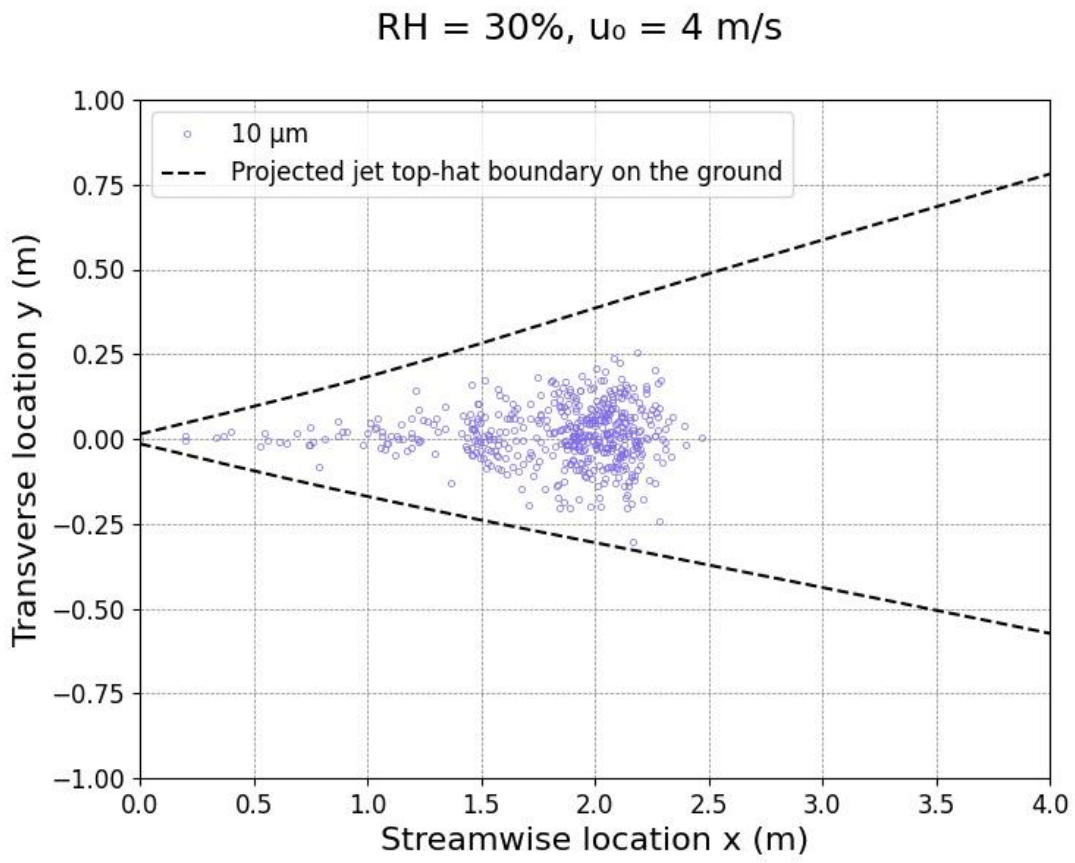

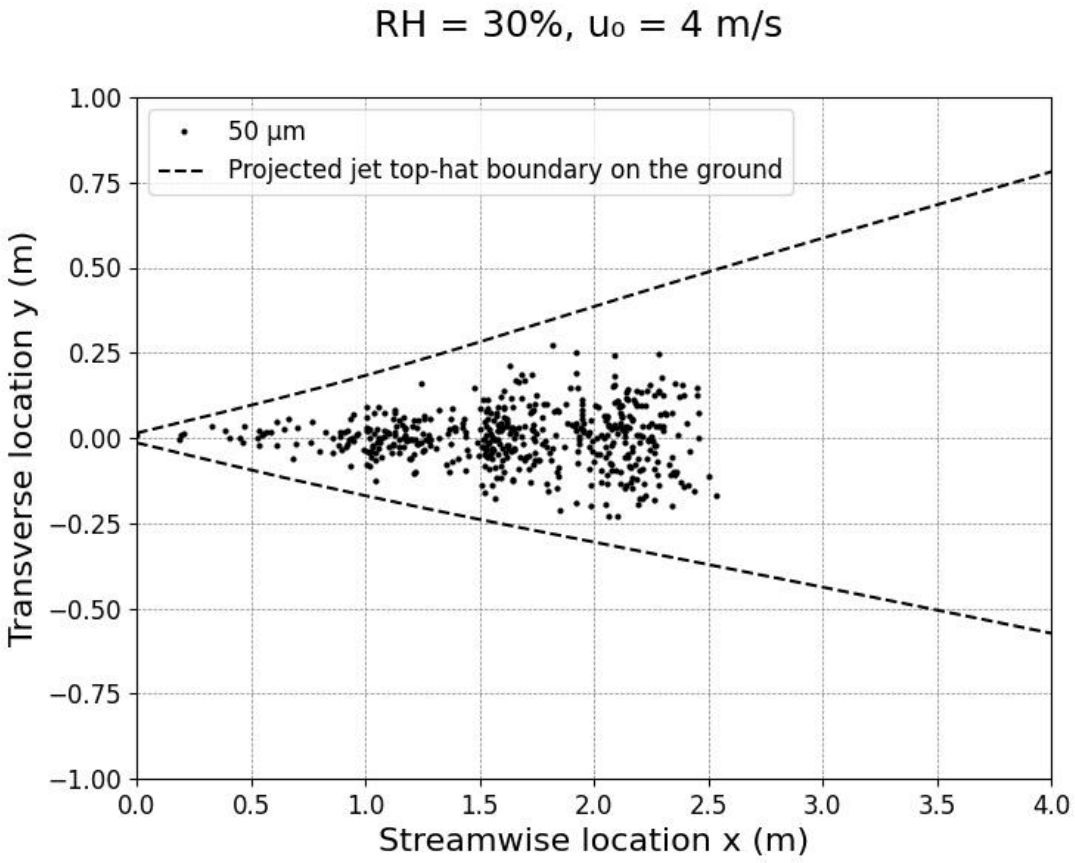

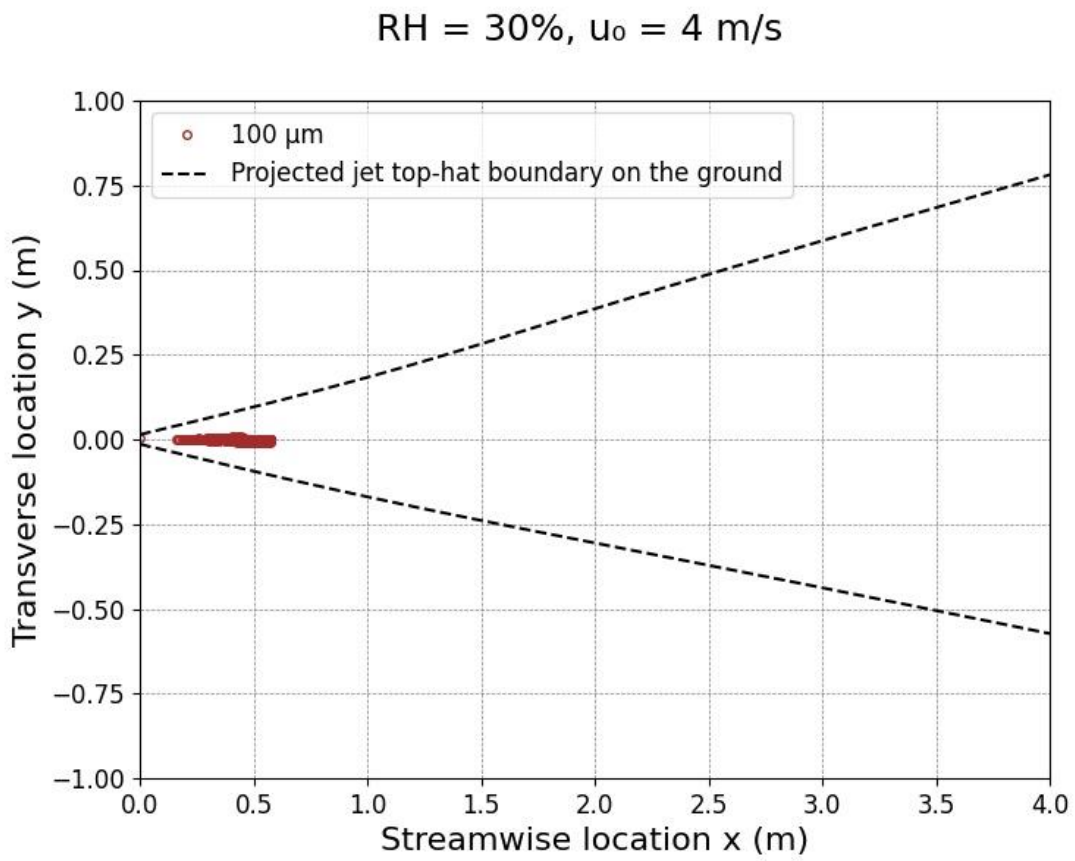
RH = 30%, u₀ = 4 m/s
100 µm
Projected jet top-hat boundary on the ground
Transverse location y (m)
Streamwise location x (m)
1.00
0.75
0.50
0.25
0.00
−0.25
−0.50
−0.75
−1.00
0.0
0.5
1.0
1.5
2.0
2.5
3.0
3.5
4.0

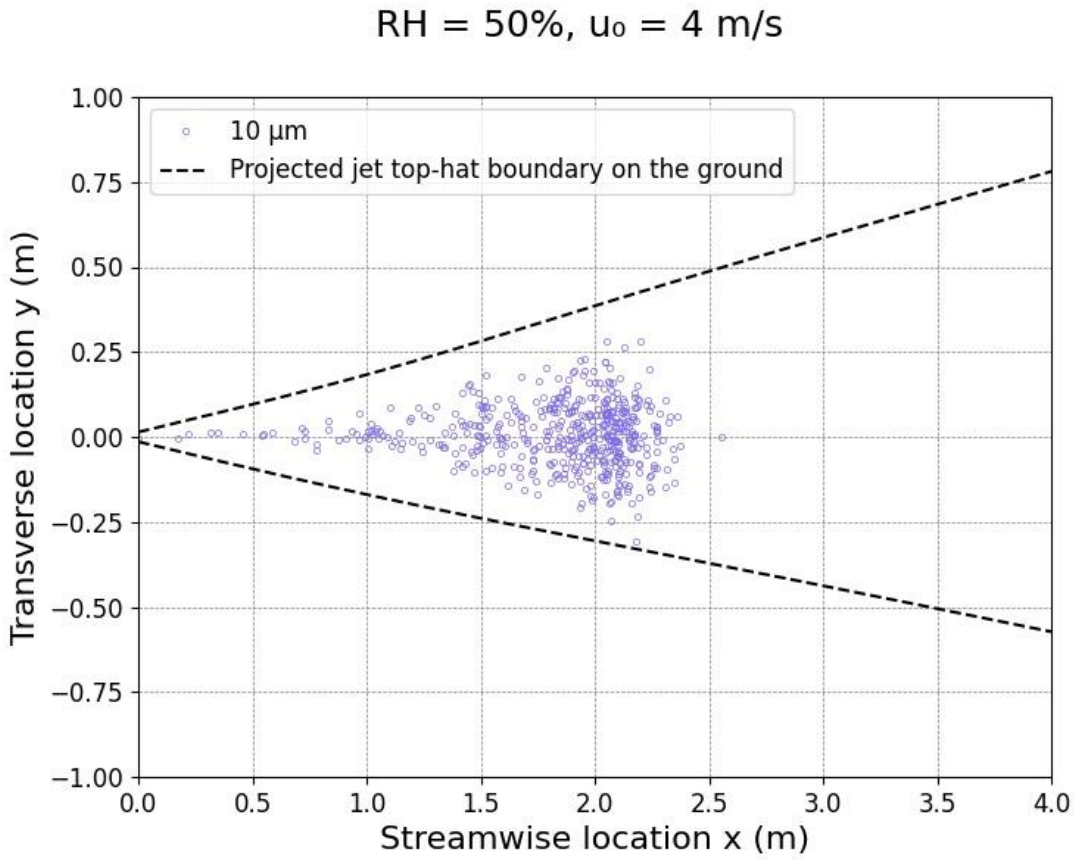
RH = 50%, u₀ = 4 m/s
10 µm
Projected jet top-hat boundary on the ground
Transverse location y (m)
Streamwise location x (m)
1.00
0.75
0.50
0.25
0.00
−0.25
−0.50
−0.75
−1.00
0.0
0.5
1.0
1.5
2.0
2.5
3.0
3.5
4.0

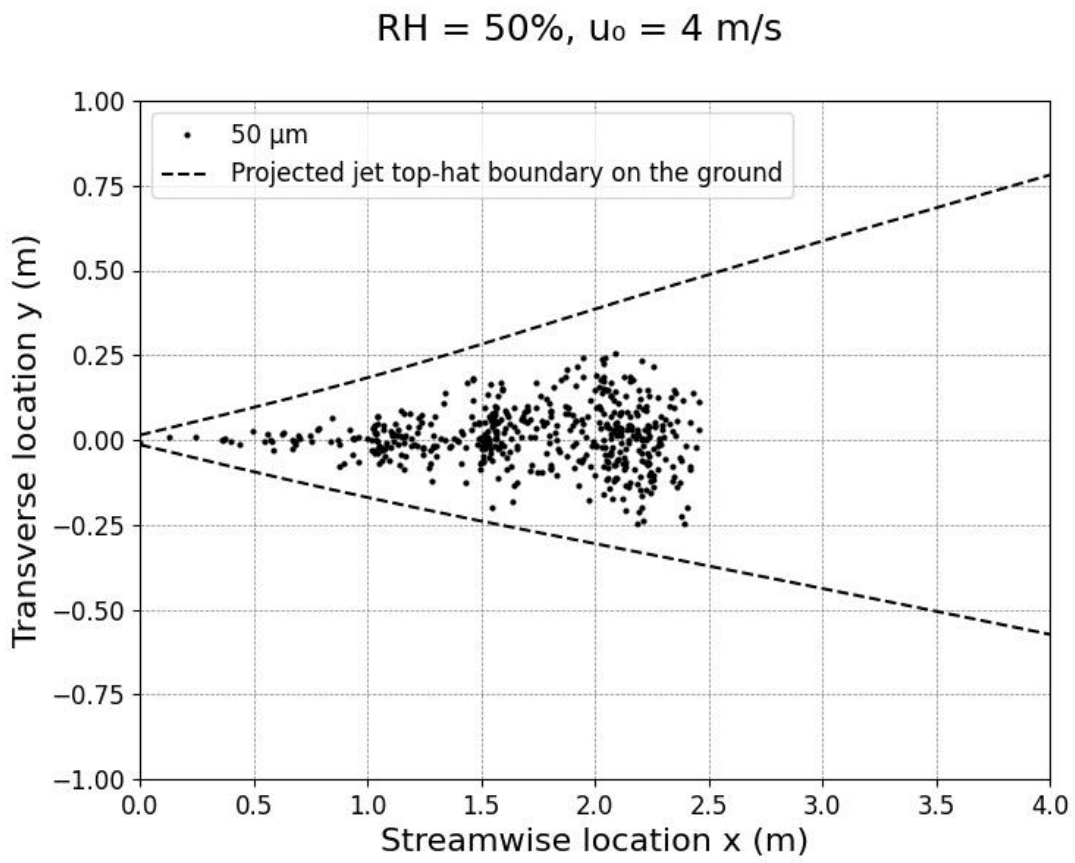
RH = 50%, u₀ = 4 m/s
50 µm
Projected jet top-hat boundary on the ground
Transverse location y (m)
Streamwise location x (m)
1.00
0.75
0.50
0.25
0.00
−0.25
−0.50
−0.75
−1.00
0.0
0.5
1.0
1.5
2.0
2.5
3.0
3.5
4.0

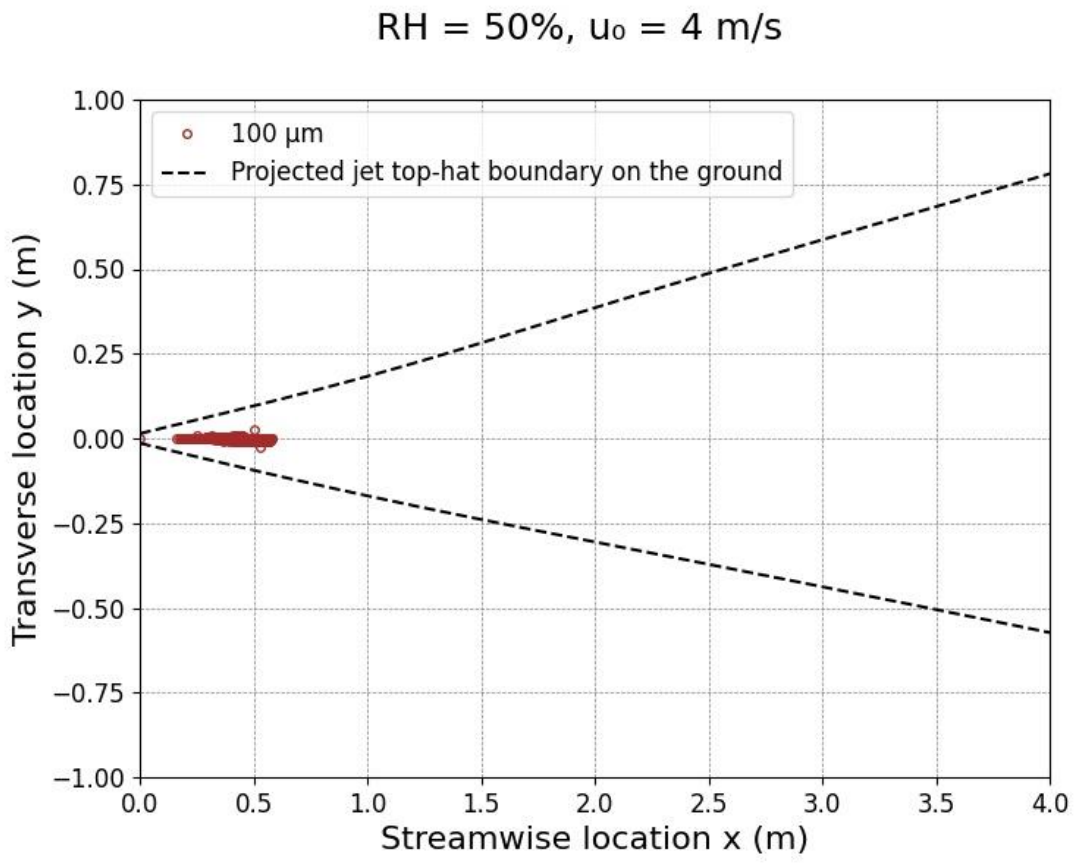
RH = 50%, u₀ = 4 m/s
100 µm
Projected jet top-hat boundary on the ground
Transverse location y (m)
Streamwise location x (m)
1.00
0.75
0.50
0.25
0.00
−0.25
−0.50
−0.75
−1.00
0.0
0.5
1.0
1.5
2.0
2.5
3.0
3.5
4.0

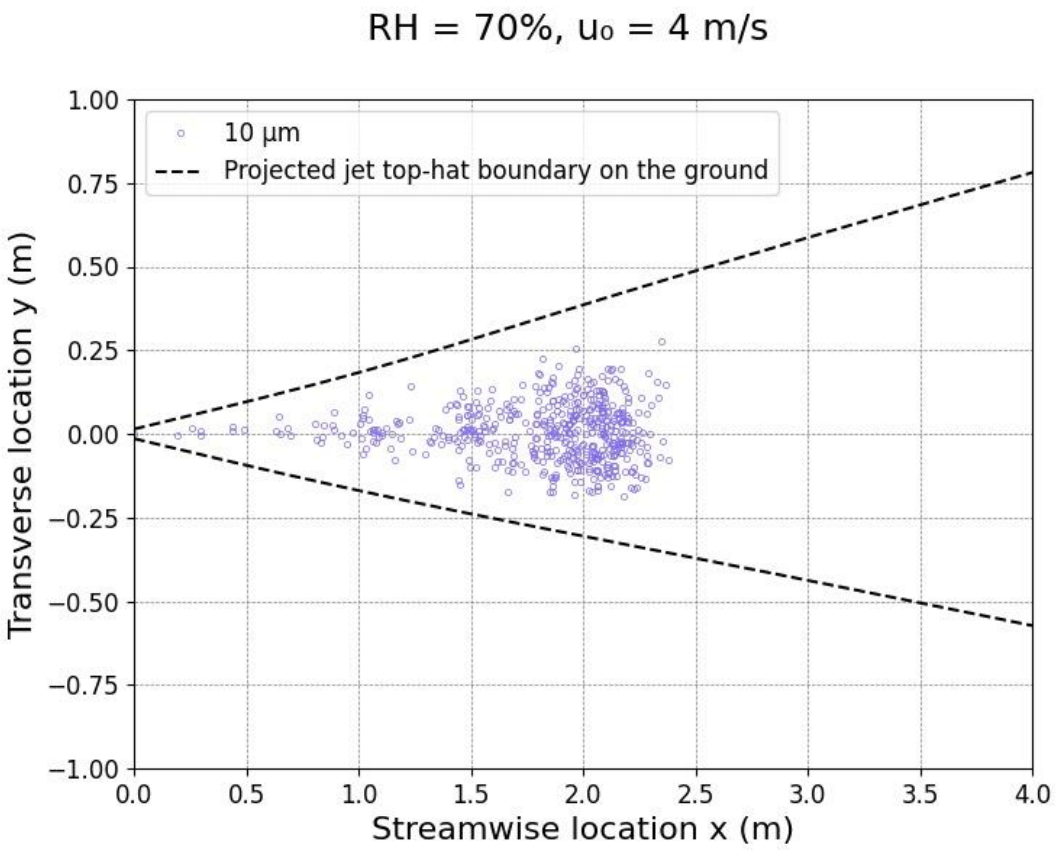
RH = 70%, u₀ = 4 m/s
10 µm
Projected jet top-hat boundary on the ground
Transverse location y (m)
Streamwise location x (m)
1.00
0.75
0.50
0.25
0.00
−0.25
−0.50
−0.75
−1.00
0.0
0.5
1.0
1.5
2.0
2.5
3.0
3.5
4.0

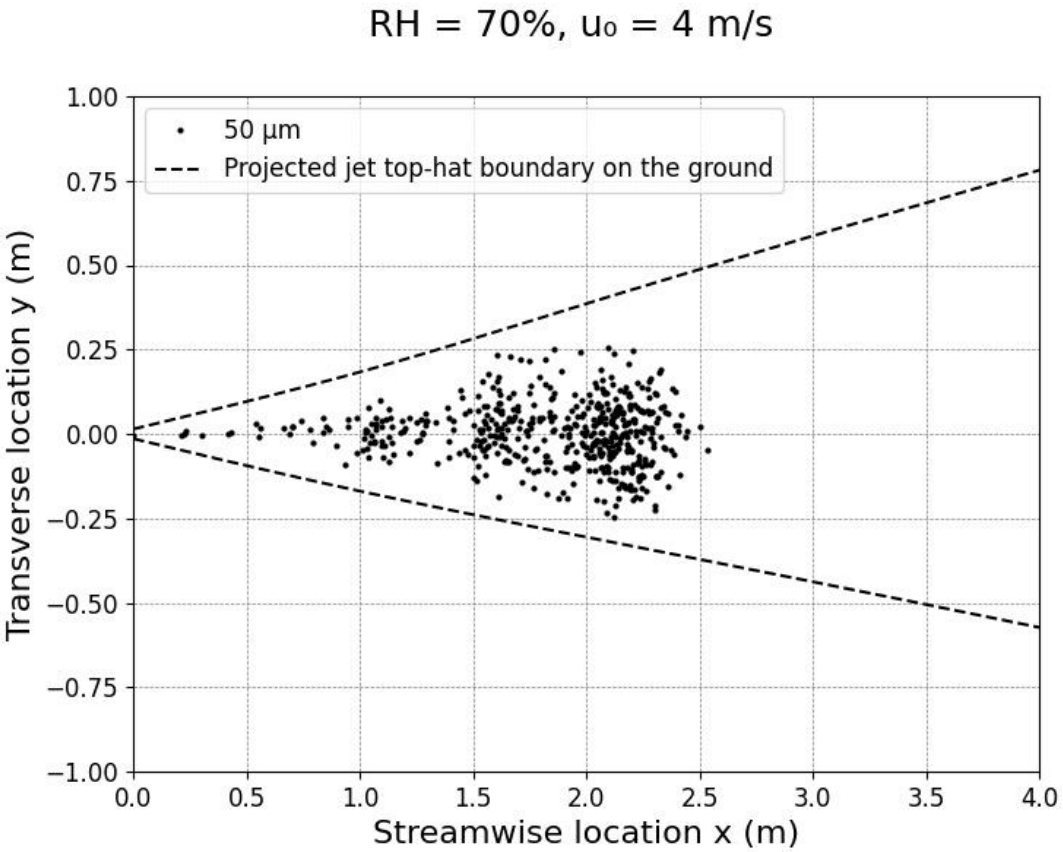
RH = 70%, u₀ = 4 m/s
50 µm
Projected jet top-hat boundary on the ground
Transverse location y (m)
Streamwise location x (m)
1.00
0.75
0.50
0.25
0.00
−0.25
−0.50
−0.75
−1.00
0.0
0.5
1.0
1.5
2.0
2.5
3.0
3.5
4.0

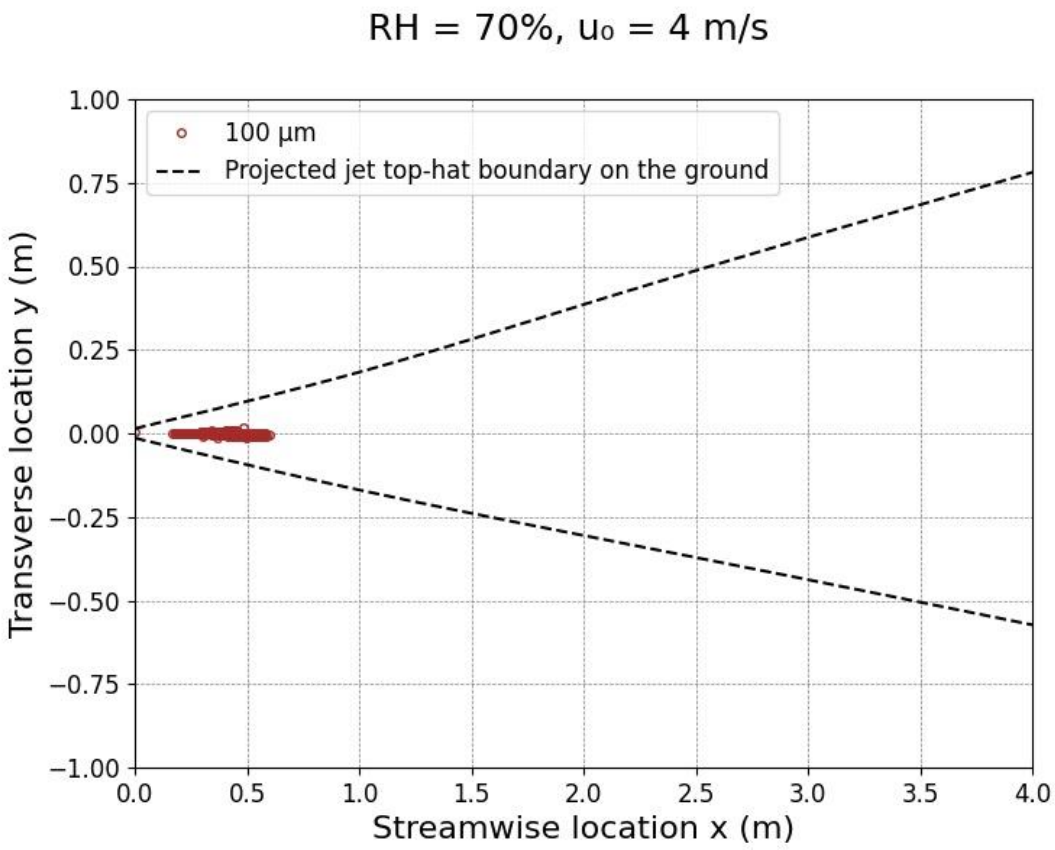
RH = 70%, u₀ = 4 m/s
100 µm
Projected jet top-hat boundary on the ground
Transverse location y (m)
Streamwise location x (m)
1.00
0.75
0.50
0.25
0.00
−0.25
−0.50
−0.75
−1.00
0.0
0.5
1.0
1.5
2.0
2.5
3.0
3.5
4.0

B.2.3 Initial velocity u_0 10 m/s

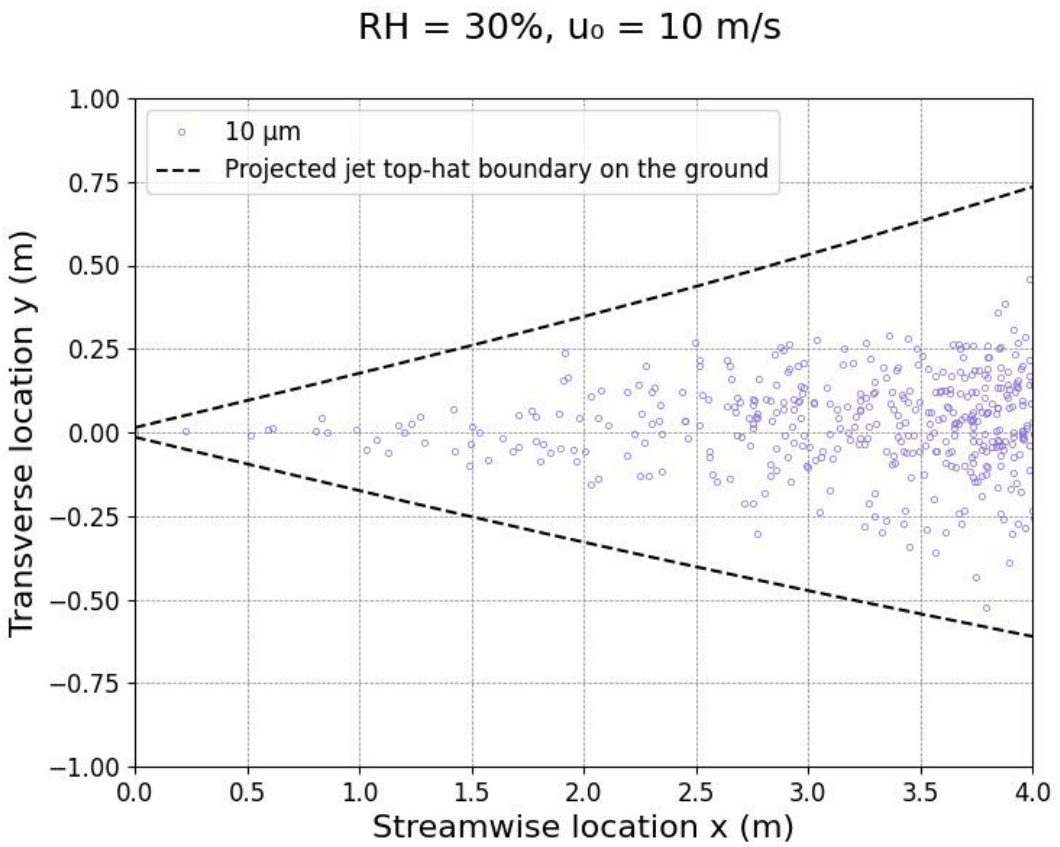

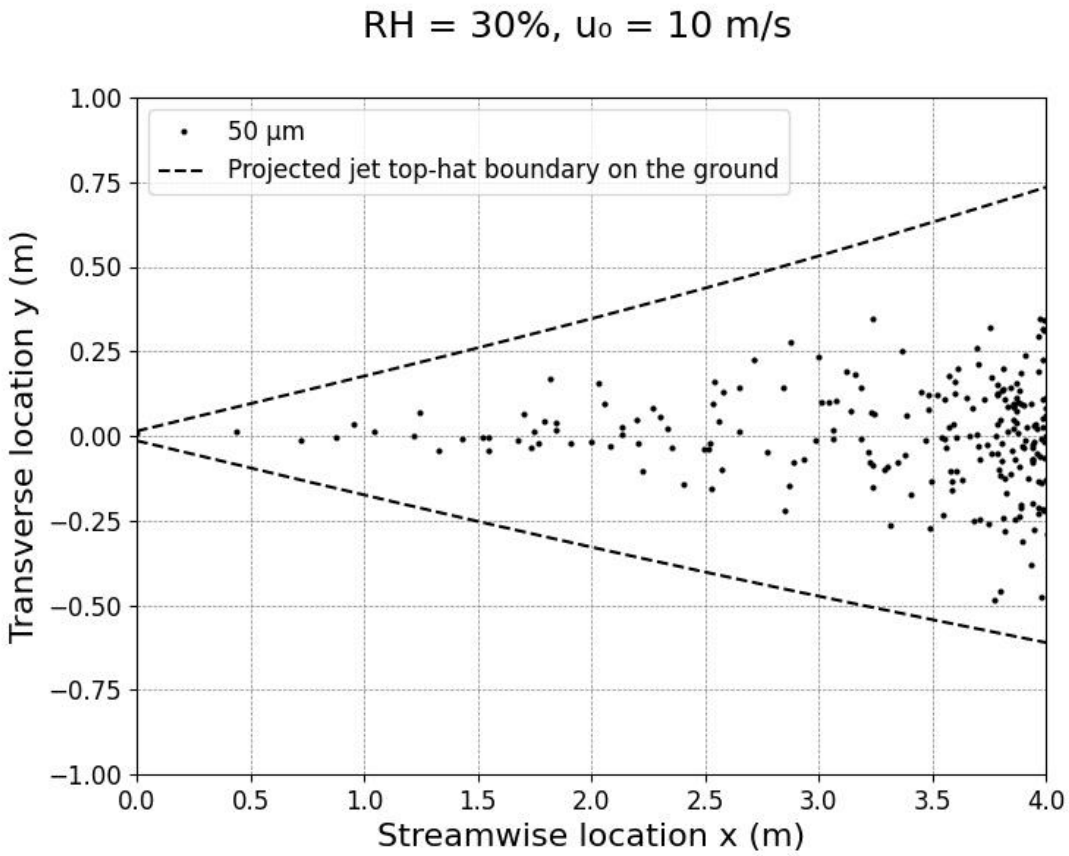

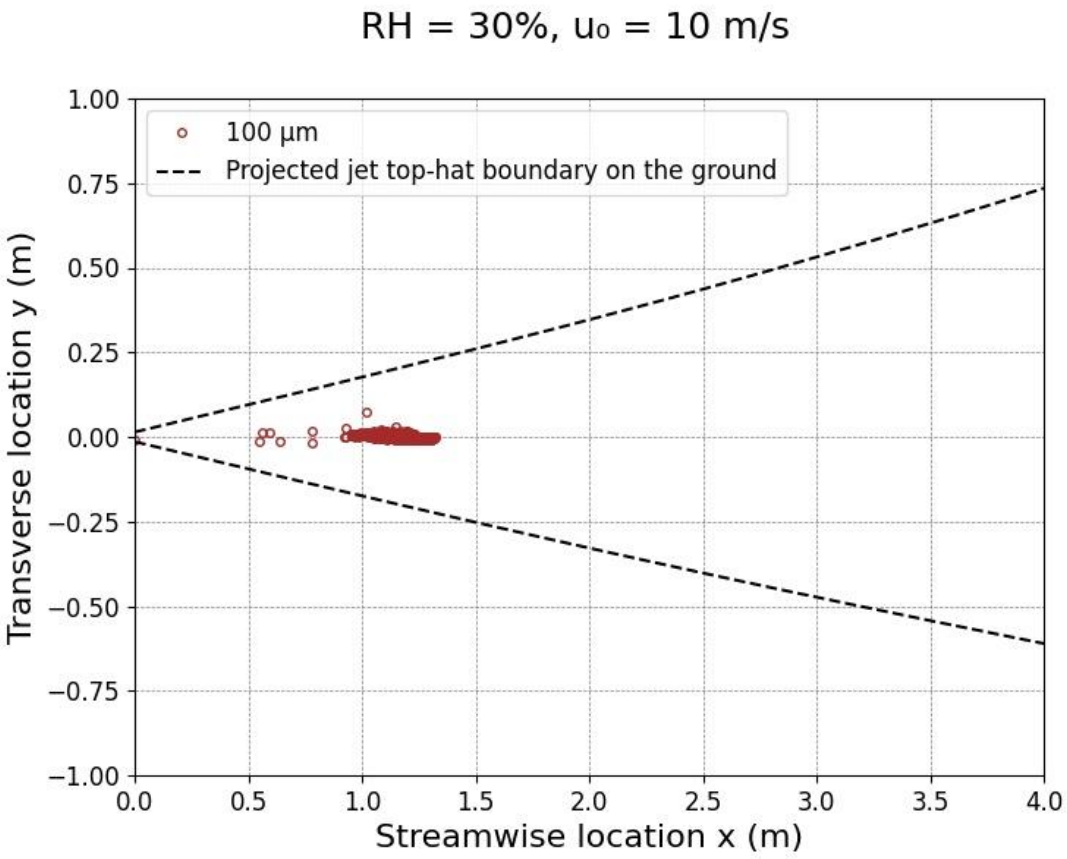
RH = 30%, u₀ = 10 m/s
100 µm
Projected jet top-hat boundary on the ground
Transverse location y (m)
Streamwise location x (m)
1.00
0.75
0.50
0.25
0.00
−0.25
−0.50
−0.75
−1.00
0.0
0.5
1.0
1.5
2.0
2.5
3.0
3.5
4.0

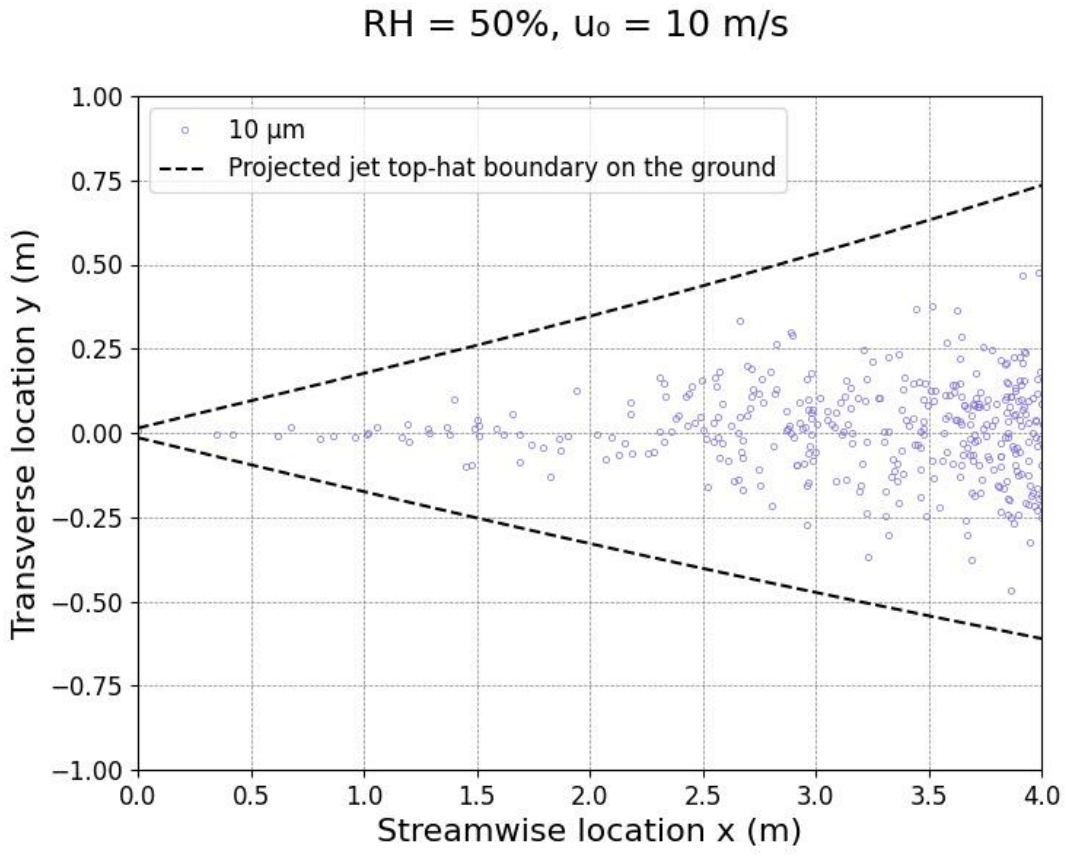
RH = 50%, u₀ = 10 m/s
10 µm
Projected jet top-hat boundary on the ground
Transverse location y (m)
Streamwise location x (m)
1.00
0.75
0.50
0.25
0.00
−0.25
−0.50
−0.75
−1.00
0.0
0.5
1.0
1.5
2.0
2.5
3.0
3.5
4.0

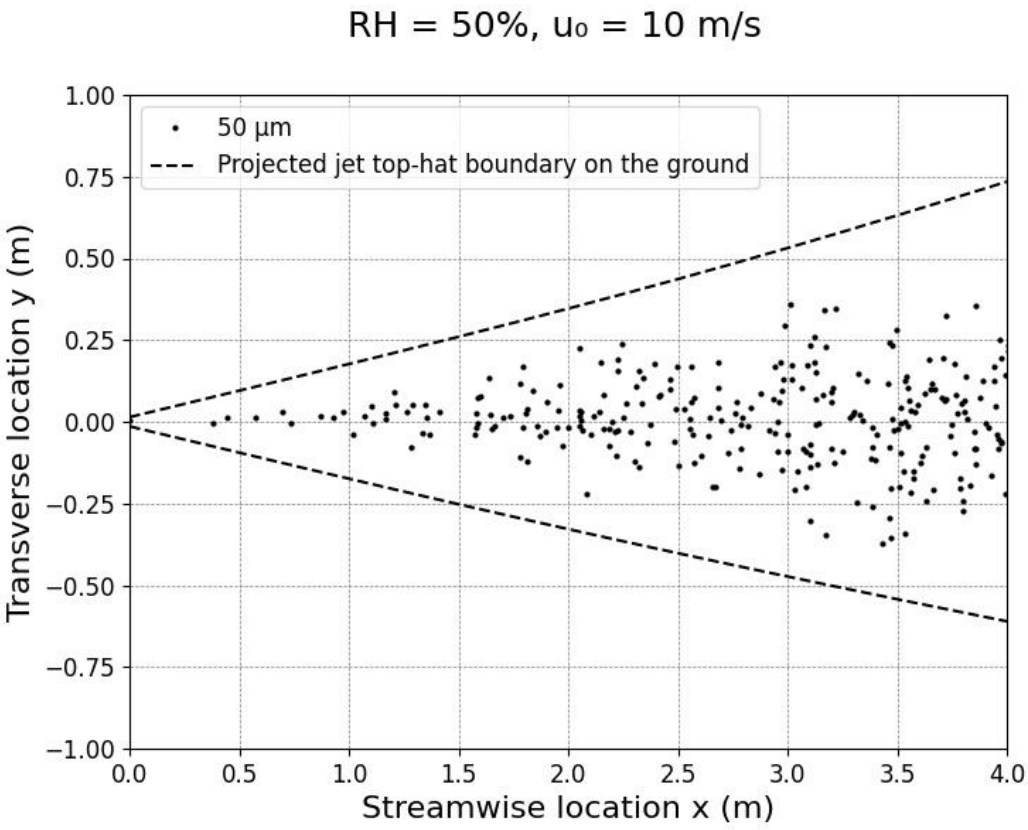
RH = 50%, u₀ = 10 m/s
50 µm
Projected jet top-hat boundary on the ground
Transverse location y (m)
Streamwise location x (m)
1.00
0.75
0.50
0.25
0.00
−0.25
−0.50
−0.75
−1.00
0.0
0.5
1.0
1.5
2.0
2.5
3.0
3.5
4.0

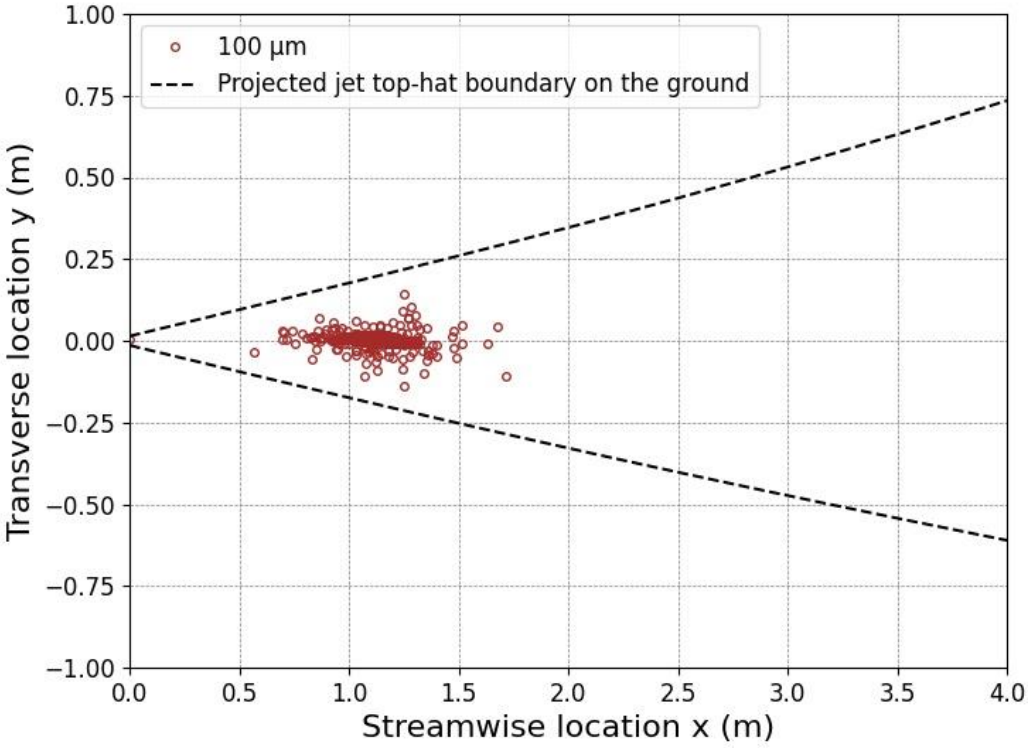
RH = 50%, u₀ = 10 m/s
100 µm
Projected jet top-hat boundary on the ground
Transverse location y (m)
Streamwise location x (m)
1.00
0.75
0.50
0.25
0.00
−0.25
−0.50
−0.75
−1.00
0.0
0.5
1.0
1.5
2.0
2.5
3.0
3.5
4.0

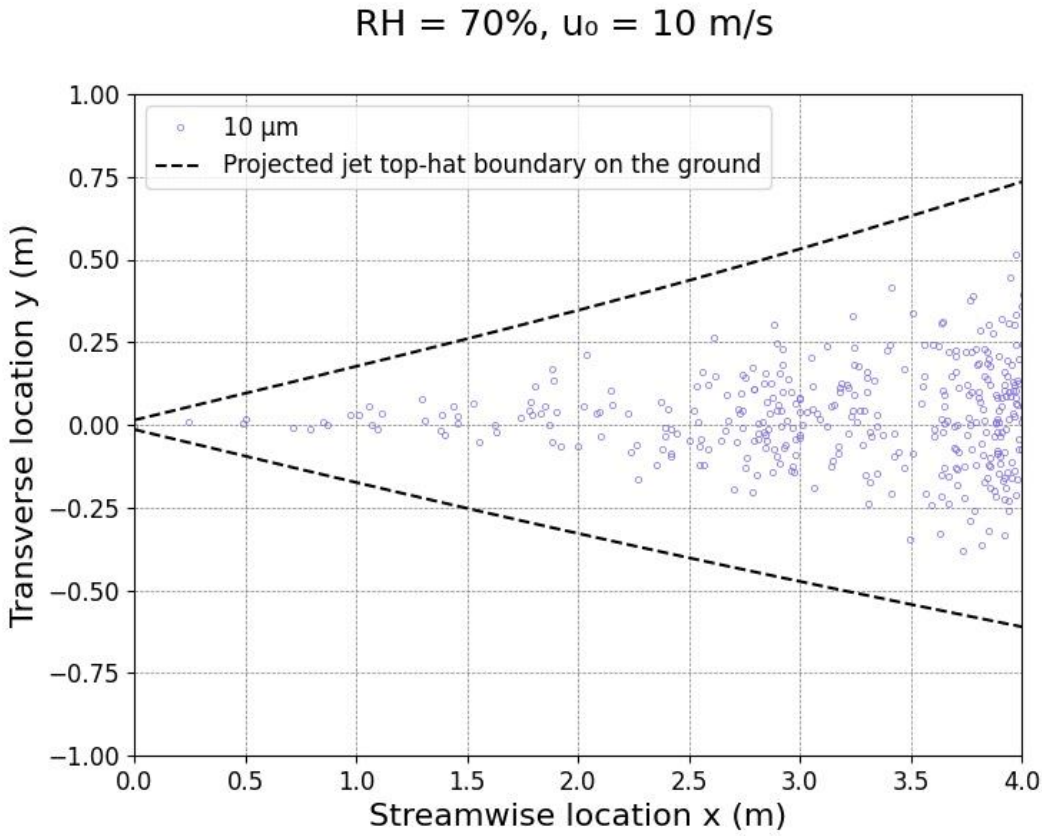
RH = 70%, u₀ = 10 m/s
10 µm
Projected jet top-hat boundary on the ground
Transverse location y (m)
Streamwise location x (m)
1.00
0.75
0.50
0.25
0.00
−0.25
−0.50
−0.75
−1.00
0.0
0.5
1.0
1.5
2.0
2.5
3.0
3.5
4.0

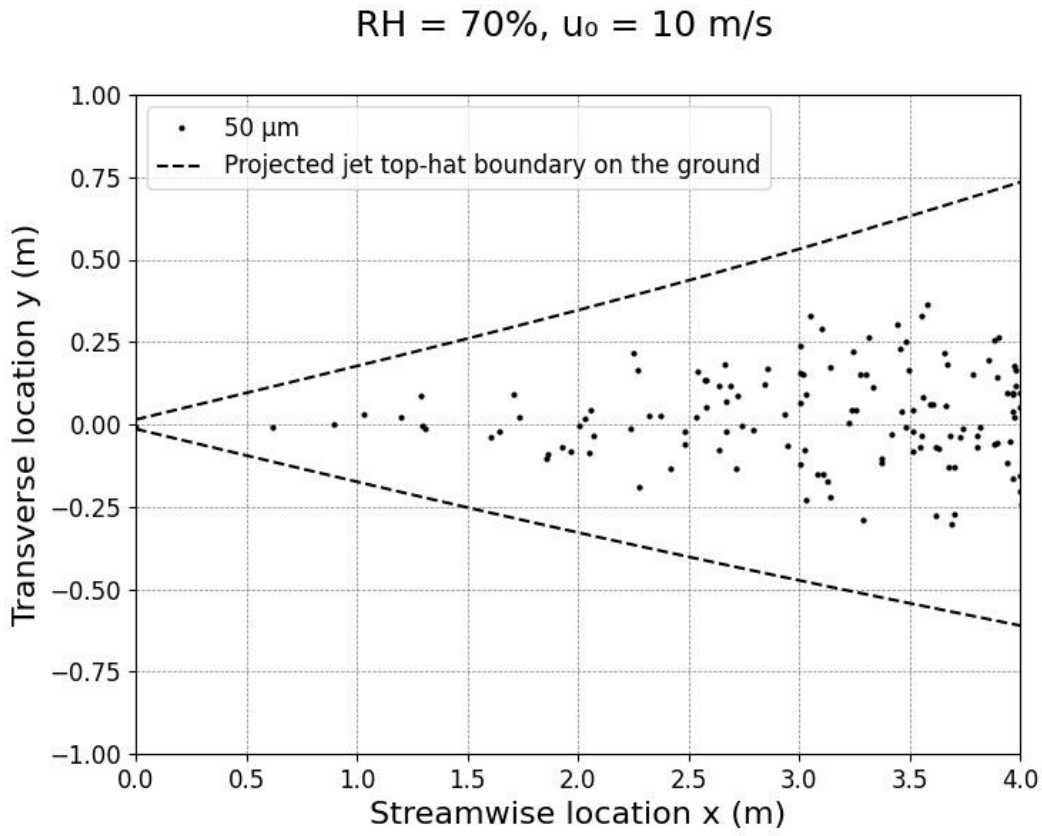
RH = 70%, u₀ = 10 m/s
50 µm
Projected jet top-hat boundary on the ground
Transverse location y (m)
Streamwise location x (m)
1.00
0.75
0.50
0.25
0.00
−0.25
−0.50
−0.75
−1.00
0.0
0.5
1.0
1.5
2.0
2.5
3.0
3.5
4.0

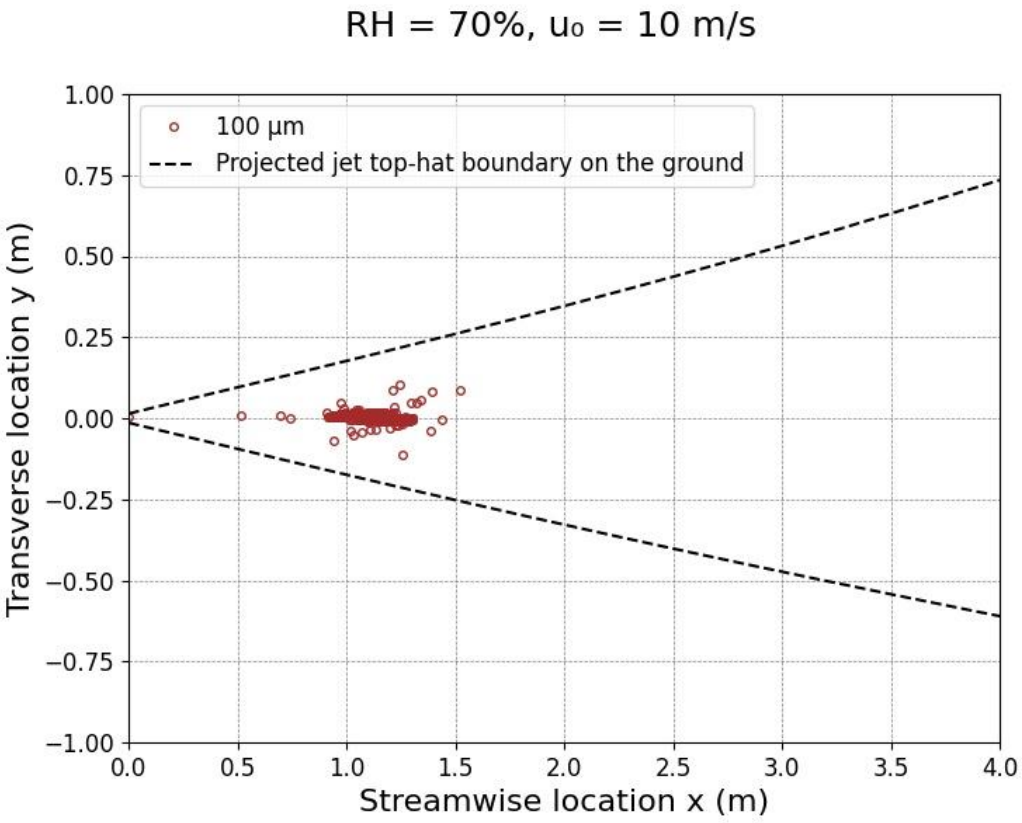
RH = 70%, u₀ = 10 m/s
100 µm
Projected jet top-hat boundary on the ground
Transverse location y (m)
Streamwise location x (m)
1.00
0.75
0.50
0.25
0.00
−0.25
−0.50
−0.75
−1.00
0.0
0.5
1.0
1.5
2.0
2.5
3.0
3.5
4.0